Design, Fabrication and Characterization of a Thermo-Mechanical Infrared Detector Array with Integrated Optical Readout

by

Refik Burak Erarslan

**A Thesis Submitted to the
Graduate School of Sciences and Engineering
in Partial Fulfillment of the Requirements for
the Degree of**

Master of Science

in

Electrical and Electronics Engineering

Koç University

July 2012

Koç University
Graduate School of Sciences and Engineering

This is to certify that I have examined this copy of a master's thesis by

Refik Burak Erarslan

and have found that it is complete and satisfactory in all respects,
and that any and all revisions required by the final
examining committee have been made.

Committee Members:

____
Hakan Urey, Ph. D. (Advisor)

____
Erdem Alaca, Ph. D.

____
Hamdi Torun, Ph. D.

Date: 20.07.2012

ABSTRACT

Thermal imaging has been a useful tool in many thermal mapping applications such as medical imaging, target detection, surveillance, monitoring circuits and rescue. This thesis reports the design, fabrication and characterization of micro electro-mechanical system (MEMS) based uncooled thermo-mechanical infrared (IR) sensor arrays integrated with CMOS based optical readout.

Pixelated sensor array operation is based on the conversion of incident IR radiation to mechanical displacement. The pixels are suspended membranes connected to a transparent substrate via bimaterial legs. Absorbed IR radiation modulates the temperature of the structure and this modulation causes the deflection of bimaterial legs that have a mismatch of coefficient of thermal expansion. This mechanical deflection is detected optically with sub-nm precision by monitoring the first diffracted order of the readout beam returning from the diffraction gratings that are embedded underneath each pixel. The main advantage of the designed sensors is that the MEMS die is passive, thus pixels are electrically and thermally isolated from the optical readout. Two options are exploited for the optical readout: (i) reimaging of diffracted light onto a CCD camera using Fourier filtering, (ii) integration of MEMS sensor array chip on a CMOS readout chip that contains a photodetector array and a through wafer via hole for each pixel for the illumination beam. This is a novel approach for optical readout and tried for the first time.

Sensor arrays are designed and microfabricated in 640x480, 320x240 and 64x64 pixel formats with 35 µm sensor pitch using standard MEMS processes with Si_xN_y/Al and Parylene/Al material combinations. Optical readout IC is fabricated using standard 0.18 µm CMOS process. As a post-process, the CMOS chips are thinned and through wafer holes are etched, which allow the readout laser beam to pass through. After the CMOS post-process steps, MEMS and CMOS dies are aligned and integrated, which enabled a novel integrated optical readout.

ÖZET

Termal görüntüleme; tıbbi görüntüleme, hedef tespiti, gözetleme, izleme devreleri ve kurtarma gibi birçok termal haritalama uygulamaları için yararlı bir araç olmuştur. Bu tezde, mikro elektro-mekanik sistem (MEMS) tabanlı, CMOS tabanlı optik okuma ile tümleştirilmiş soğutmasız termo-mekanik kızılötesi (IR) algılayıcı dizinlerinin tasarım, üretim ve karakterizasyonu sunulmaktadır.

Algılayıcının çalışma prensibi, gelen kızılötesi ışınımın mekanik bükülmeye dönüştürülmesine dayanmaktadır. Pikseller, transparan bir alttaşa çiftmaddeli bacaklar aracılığıyla bağlanan asılı zarlardan oluşmaktadır. Emilen kızılötesi ışınım, yapının sıcaklığını değiştirir ve bu değişim, uzama katsayıları farklı olan çiftmadde bacakların bükülmesine neden olur. Bu mekanik bükülme, her pikselin altına gömülmüş kırınım ızgaralarından yansıyan okuma ışınının birinci kırınım mertebesi algılanarak nanometre altı hassasiyet ile optik olarak ölçülür. Tasarlanan algılayıcının en önemli özelliği pasif olmalarıdır, böylelikle okuma kısmından elektriksel ve termal olarak yalıtılmış durumdadırlar. Optik okuma için iki yöntemden yararlanılmıştır: (i) yansıyan ışının kırınım birinci mertebesinin Fourier filtrelemesi kullanılarak tekrar görüntülenmesi, (ii) MEMS algılayıcı dizini ile fotodetektör dizini ve dizindeki her piksel için optik okuma ışığını geçirmeyi sağlayan delikler barındıran CMOS çipinin tümleştirilmesi. Bu yöntem, optik okuma için yeni geliştirilen ve ilk defa denenen bir yöntemdir.

Algılayıcı dizinleri 640x480, 320x240, 64x64 formatlı ve 35 µm piksel boyutlu olarak tasarlanmış, Si_xN_y/Al ve parylene/Ti malzeme çiftleri kullanılarak, standart MEMS süreçleri ile üretilmiştir. Optik okuma devresi ise standart CMOS 0.18 µm üretim teknolojisi kullanılarak üretilmiştir. Üretim sonrası işlemler olarak çipler inceltilmiş ve çiplere okuma ışınının geçmesine izin verecek delikler açılmıştır. Elektronik çiplerin üretim sonrası işlemlerinden sonra bu çipler MEMS çiplerle hizalanmış ve bütünleştirilmiş, bu bütünleştirme yeni bir tümleşik optik okuma yöntemini mümkün kılmıştır.

ACKNOWLEDGEMENTS

I would like to thank my thesis advisor Hakan Ürey for his support and guidance throughout this work. It was a privilege to be a part of the Optical Microsystems Laboratory (OML). I will always remember OML with its joyful research environment and physical activity based social events. I would also like to thank Prof. Erdem Alaca and Prof. Hamdi Torun for taking part in my thesis jury.

I would like to express my gratitude to Aselsan microelectronics, guidance and electro-optics group headed by Hacer Selamoğlu for their support and funding. I would like to thank Oray Orkun Cellek and Engin Ufuk Temoçin for their support and valuable feedback. I would also acknowledge Prof. Yusuf Leblebici for his kind invitation to his group at Ecole Polytechnique Fédérale de Lausanne (EPFL) as a visiting researcher to use cleanroom facilities. I am thankful to Yüksel Temiz from EPFL for helping me during the fabrication process. I want to thank Center of MicroNano Technology (CMi) staff, especially Jean Baptise Bureau for their support inside and outside the cleanroom. I am also grateful to Orhan Akar from METU MET and the staff who assisted fabrication runs related to this work. I would also acknowledge TÜBİTAK scholarship for my MSc studies and Koç University for the funding that I received.

It would have been impossible to complete my studies without the help of my colleagues at OML, especially Dr. Onur Ferhanoğlu for building a very solid background and for his fabrication effort during his PhD years on the same research. He always encouraged me, replied all my silly questions and accompanied me in cleanroom with his unique songs and poems. I also want to thank Selim Abi for helping me in any subject related to my research or not. I want to thank Dr. Hamdi Torun again for his support and valuable help throughout this work. I am grateful to Fatih Toy for answering all my questions and his friendship in the beautiful (boring!) city Lausanne. I am also thankful to

my lab partners S. Zeynep Lüleç and Ulaş Adiyan for all the help and joy they provided regarding different aspects of this project.

It was a privilege to work with the present and previous members of OML, especially Sven, Kutal and Erdem. I also want to thank Aslıhan, Duygu, Pelin, Cem, Erhan, Onur, Kaan, Aref, Utku, Kıvanç and Başar.

Finally, I want to thank my family and Tuğçe for their emotional support and understanding during my graduate studies. It is certain that this thesis would be impossible without them.

Table of Contents

ACKNOWLEDGEMENTS....................v

LIST OF FIGURES....................x

LIST OF TABLES....................xv

NOMENCLATURE....................xvi

1 INTRODUCTION....................18

1.1 Infrared Radiation....................18

1.2 Infrared Detector Types and Applications....................20

1.3 MEMS-based Thermal Detectors....................22

1.3.1 Bolometers....................23

1.3.2 Thermo-Mechanical Detectors....................24

1.4 MOEMS Thermal Imaging System Developed at Koç University....................26

1.5 Contributions of the Thesis....................29

2 THERMO-MECHANICAL IR SENSOR DESIGN....................31

2.1 Design Parameters....................31

2.2 Material Selection....................35

2.3 Mechanical and Thermal Design....................36

2.3.1 Si_xN_y/Al Sensor Design....................37

2.3.2 Parylene/Ti Sensor Design....................38

2.3.3 Finite Element Analysis....................39

2.4 Optical Readout....................42

2.4.1 Diffraction Grating Method....................43

2.4.2 Optical Lever Method....................45

2.5 System Theoretical Performance....................46

3 FABRICATION OF IR SENSOR ARRAY 48
3.1 Si_xN_y/Al sensor array fabrication 48
3.2 Parylene/Ti Sensor Array Fabrication 55
3.2.1 Process Flow 56
3.2.1.1 Wafer Preparation 57
3.2.1.2 Lift-off 57
3.2.1.2.1 Photoresist Spinning 57
3.2.1.2.2 Exposure and Develop 57
3.2.1.2.3 Metal Deposition and Patterning 58
3.2.1.3 Deposition and Patterning of Sacrificial Layer 59
3.2.1.4 Parylene deposition 60
3.2.1.5 Ti Layer Deposition and Patterning 60
3.2.1.6 Patterning of Structural Layer 62
3.2.1.7 Dicing 63
3.2.1.8 Releasing 63
3.2.1.9 Thin Film Absorber Deposition 65
3.3 Process Optimizations 67
3.4 CMOS ROIC Post-Processing 71
3.4.1 Grinding 71
3.4.2 Chip Handling 72
3.4.3 Etching Holes 73
3.4.4 Releasing 76
4 TEST AND CHARACTERIZATION RESULTS 78
4.1 Thermal and Mechanical Tests 78
4.1.1 Direct Heating Experiments 79
4.1.2 IR Imaging Experiments 82
4.2 CMOS ROIC Characterization 85
4.3 MEMS & CMOS ROIC Integration 94

4.3.1 Design and Layout 94
4.3.2 Alignment and Integration 97
4.4 Packaging 102

5 CONCLUSION 104

BIBLIOGRAPHY 106

LIST OF FIGURES

Figure 1.1 Black body curves for various temperatures..19

Figure 1.2 IR detector technologies. Photon detectors and thermal detectors are can also be classified as cooled and uncooled detectors. Boxes with blue background illustrate technologies exploited in this research. 21

Figure 1.3 Applications of IR imaging: (a) Surveillance (b) Security applications (c) Medical imaging (Infrared Cameras Inc.) (d) inspecting electronic circuits (e) military target detection (f) Veterinary applications..22

Figure 1.4 Schematic of IR imaging system developed at Koç University 27

Figure 1.5 (a) Si_xN_y/Al sensor designs. (b) Parylene/Ti sensor designs. (c) IR image of a human hand in front of IR heater. (d) IR image of a labeled plate in front of IR heater captured with Si_xN_y/Al array...28

Figure 2.1 Diffraction order intensity vs. displacement of the membrane....................33

Figure 2.2 Si_xN_y/Al IR sensor designs: (a) Two end fixed design. (b) One end fixed design. (c) Design not requiring TEC. 37

Figure 2.3 Parylene/Ti IR sensor designs: (a) Two end fixed design. (b) One end fixed design. (c) 4-leg design. 39

Figure 2.4 FEM simulation for deflection analysis of the design not requiring TEC....40

Figure 2.5 Thermo-mechanical simulation results for thermal cross-talk analysis........41

Figure 2.6 FEM simulation for the modal analysis of two end fixed design (first three modes)...42

Figure 2.7 Lever and grating based optical readout methods. 43

Figure 2.8 (a) Side-view of an IR pixel illustrating grating readout. (b) Grating readout schematic with photodetectors. 43

Figure 2.9 Intensity of light going to diffraction orders as a function of the distance from the membranes to the diffraction gratings. 45

Figure 2.10 Side-view of an IR pixel and top view of photodetectors illustrating optical lever readout. 46

Figure 3.1 Fabrication steps of Si_xN_y/Al sensor array: (1) Gold grating patterning (2) Sacrificial polyimide coating and patterning (3) Blanket deposition of Nitride and Aluminum layers (4) Al patterning with wet etch (5) Nitride patterning (6) Release with oxygen plasma (7) Absorber deposition. 49

Figure 3.2 (a) Drawn designs. (b) Numbered mask layout. (c) Diced wafer after fabrication 51

Figure 3.3 Fabricated Si_xN_y/Al sensor arrays: (a) microscope image of 6x5 array. (b,c) microscope images of 3x2 array. Bending of legs is shown. (d) SEM image of successfully fabricated sensor array. (e) SEM image of two pixels with bended legs. 52

Figure 3.4 Fabricated Si_xN_y/Al sensor arrays: (a) Microscope image of a fabricated array showing non-released pixels. (b) Optical profiler image of the same array. (c) Optical profiler image of 2-sided design. 53

Figure 3.5 Detailed profile measurement taken with white light interferometer. 54

Figure 3.6 Mask layout of parylene/Ti sensor arrays. 55

Figure 3.7 Fabrication steps of Parylene/Ti sensor array: (1) Titanium grating patterning (2) Sacrificial photoresist coating and anchor patterning (3) Blanket deposition of parylene (4) Ti deposition and patterning (5) Parylene dry etching (6) Release with resist remover and critical point dryer (7) deposition of absorber layer. 56

Figure 3.8 Defined gratings with lift-off process. 59

Figure 3.9 Anchor definition on photoresist sacrificial layer......................................60

Figure 3.10 Titanium layer patterned for bimaterial legs and reflectors of (a) one-sided design. (b) two-sided design. (c) 4-leg design. 61

Figure 3.11 (a,b,c,d) The devices on top of sacrificial layer after RIE step. (e,f) optical profiler images of the devices. 62

Figure 3.12 Successfully released devices. 64

Figure 3.13 Sheet resistance of Ti for different thicknesses for 2 different deposition equipment. 66

Figure 3.14 Sheet resistance change of 10 nm Ti after 4 days. 66

Figure 3.15 Previous process flow. 67

Figure 3.16 Grating definition on top of Pyrex wafer by wet etching techniques. 68

Figure 3.17 cracking and buckling after deposition of blanket titanium on parylene....69

Figure 3.18 (a) Photolithography errors in the edges of bimaterial legs. (b) Not well-defined legs connected to adjacent pixel's anchor. 70

Figure 3.19 (a) Unremoved photoresist on bimaterial legs and the reflector. (b) buckling of sensor membranes after photoresist removal at 80 °C....................................71

Figure 3.20 (a,b) Thinned CMOS chips placed on the holder wafer with dry film and capton tape. (c,d) SEM images of patterned dry film. 73

Figure 3.21 (a) Top metal mask layout for hole etching. (b) SEM images of etched holes. 74

Figure 3.22 (a) SEM images of CMOS chip from backside. (b) SEM image of a hole.75

Figure 3.23 Microscope images of CMOS chip after Al removal. 76

Figure 3.24 Microscope images with backside illumination using (a) 10x objective. (b) 20x objective. 77

Figure 4.1 Direct heating in SEM chamber. (a) Image at 25 ºC. (b) Image at 50 ºC. 79

Figure 4.2 Illustration of the experimental setup for direct heating. 80

Figure 4.3 Direct heating experiment of parylene/Ti array. (a) CCD image of 1st diffracted orders and randomly chosen pixel. (b) Intensity change of the heated pixel. 81

Figure 4.4 Direct heating experiment of Si_xN_y/Al array. (a) Intensity change of the self-levelling pixel. (b) Intensity change of lever design pixel. 82

Figure 4.5 (a) Illustration of the experimental setup for infrared imaging experiments. (b,c) Pictures of the setup. 83

Figure 4.6 2 frames of a captured IR video of a moving soldering iron. 84

Figure 4.7 (a) Designed PCB for wirebonding. (b) Image of wirebonded test chip. (c,d) Wirebonded post-processed chip to PCB with hole. 85

Figure 4.8 (a) Top view of the layout. (b) Bottom view of the layout. (c) Top view of the PCB. (d) Bottom view of the PCB. 86

Figure 4.9 Graphical user interface for testing 87

Figure 4.10 Preliminary results of ROIC chip. (a) Output voltage is stable for the chip that is covered with metal mask. (b) Output voltage swing is obtained for the chip with photodetectors not covered with metal mask. 88

Figure 4.11 Image of the laser spot and zoomed version of it using MATLAB............89

Figure 4.12 (a) Laser profile with highest intensity taken with MATLAB. (b) Laser spot imaged with GUI. 90

Figure 4.13 Experimental setup for CMOS ROIC characterization 91

Figure 4.14 The graph of incidence laser power on single PD vs. single PD current....92

Figure 4.15 Test results of CMOS ROIC for linearity and saturation 93

Figure 4.16 IC chip and MEMS integration for optical microphone [57]. 94

Figure 4.17 Top level structure block diagram. 96

Figure 4.18 MEMS-CMOS array configuration 97

Figure 4.19 First alignment setup..98

Figure 4.20 (a) MEMS chip with holder PCB. (b) Microscope image of MEMS array with epoxy. (c) Inspected alignment marks after UV cure of epoxy. (d) Alignment mark that is not inspected during alignment. (e) Google SketchUp model of the integration. (f) Image of MEMS chip integrated with CMOS chip. 99

Figure 4.21 (a) Second alignment setup. (b,c) Alignment marks before UV curing (d,e) Alignment marks after UV curing..101

Figure 4.22 (a) Conceptual drawing of the vacuum package. (b) Side view of the CMOS ROIC chip integrated with IR detector in vacuum package. 103

LIST OF TABLES

Table 1-1 Commercial and state-of-the-art R&D uncooled infrared bolometer arrays. 24

Table 1-2 Comparison of bolometers and thermo-mechanical IR detectors. 25

Table 2-1 Specifications of the thermo-mechanical IR sensor array 34

Table 2-2 Thermal and mechanical properties of selected MEMS materials. 35

Table 2-3 Fill factors, time constants and NETD values of both parylene/Ti and Si_xN_y/Al designs for 10 and 12 bit CCD cameras. 47

Table 4-1 Specifications of the CMOS ROIC 95

NOMENCLATURE

AFM	Atomic Force Microscope
CCD	Charge Coupled Device
CMOS	Complementary Metal-Oxide-Semiconductor
CVD	Chemical Vapor Deposition
CTE	Coefficient of Thermal Expansion
DRIE	Deep Reactive Ion Etching
FEA	Finite Element Analysis
FPA	Focal Plane Array
HF	Hydrofluoric Acid
IC	Integrated Circuit
IR	Infrared
LOR	Lift-off resist
LWIR	Long wave Infrared
MEMS	Micro-electro-mechanical Systems
MWIR	Mid wave Infrared
ND	Neutral Density
NETD	Noise Equivalent Temperature Difference
NIR	Near Infrared
PCB	Printed Circuit Board
PD	Photodetector
PWM	Pulse Width Modulation
QWIP	Quantum Well Infrared Photodetector
RIE	Reactive Ion Etching

ROIC	Readout Integrated Circuit
SEM	Scanning Electron Microscope
SWIR	Short wave Infrared
UV	Ultraviolet
TCR	Temperature Coefficient of Resistance
TEC	Thermo-Electric Cooler
TIA	Trans-Impedance Amplifier

1 INTRODUCTION

1.1 Infrared Radiation

The infrared (IR) detector devices are passive devices that collect the radiated energy from the targets according to Planck's radiation law assuming that all the objects behave as black bodies. A black body is an idealized physical body that absorbs all incident radiation, regardless of frequency. A black body in thermal equilibrium emits electromagnetic radiation according to Planck's radiation law that it has a spectrum that is determined by the temperature only. The expression of the energy emitted per unit volume per unit wavelength from a black body is given in equation 1-1.

$$E_\lambda = \frac{8\pi hc}{\lambda} \frac{1}{\exp(hc/\lambda kT) - 1} \tag{1-1}$$

where h is Planck's constant, c is speed of light, λ is wavelength of the radiation, k is the Boltzmann's constant and T is the temperature of the black body. The only parameters that determine the amount of radiated energy are wavelength and temperature; therefore one can create the thermal map of an object by detecting the radiated energy. Black body curves for various temperatures are given in Figure 1.1. As the temperature decreases, the peak of the black-body radiation curve moves to lower intensities and longer wavelengths. In other words, hot objects emit peak radiation at shorter wavelengths.

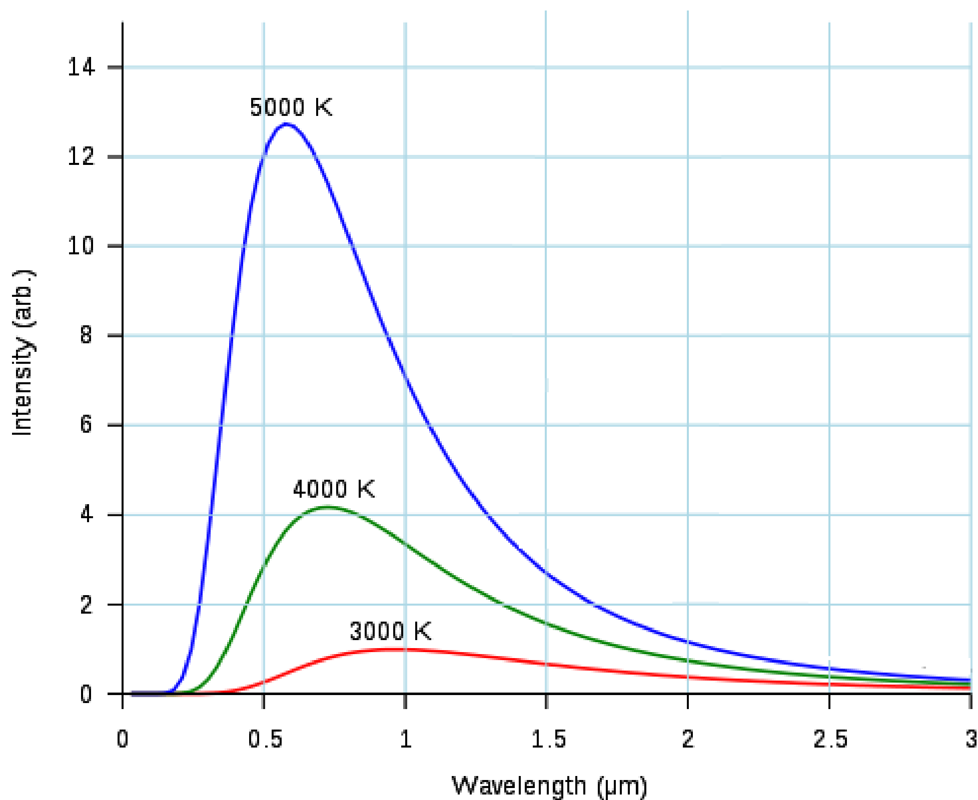

Figure 1.1 Black body curves for various temperatures

For instance, the sun's temperature is around 6000 K and its peak emission wavelength is around 500 nm. On the other hand, living creatures at 300 K emit radiation with a peak wavelength in the IR region of the spectrum which is nearly 10 µm. The interested band of the spectrum is classified as IR band and this band is also divided into sub-bands as a function of wavelength, which are near IR (NIR, 0.78-1 µm), short wavelength IR (SWIR, 1-3 µm), mid-wavelength IR (MWIR, 3-5 µm), long-wavelength IR (LWIR, 8-14 µm) and very long-wavelength IR (VLWIR, 14-100 µm).

Several detector technologies have been developed for these sub bands since each band has their own characteristics. Atmospheric gasses greatly affect the transmission of IR radiation and the transmittance of the atmosphere is high in MWIR and LWIR bands. This is the reason why infrared detectors are designed to operate in these wavelength ranges.

1.2 Infrared Detector Types and Applications

Detection of infrared radiation is performed by two different detection technologies as photon detection and thermal detection. In photon detectors, the detection mechanism is based on the excitation of electrons of a material from valance band to conduction band caused by incident photon. The absorbed photons generate electron-hole pairs. Thermally generated electron-hole pairs are larger than the IR induced pairs; therefore these detectors require cryogenic cooling. This cooling requirement makes the photon detectors bulky and expensive.

Whereas in thermal detection, temperature change by the absorbed IR radiation modulate a measurable property of the material. Thermal detectors are suspended on several legs which connect the device to substrate. Thermal detectors are relatively slow and have lower sensitivity comparing to photon detectors; however they do not require cooling which decrease the cost and complexity. Several sub-categories exist for both photon and thermal detectors and they are shown in Figure 1.2. Detailed analysis of IR detector types is not a concern of this thesis and it has been provided elsewhere [1], [2], [3].

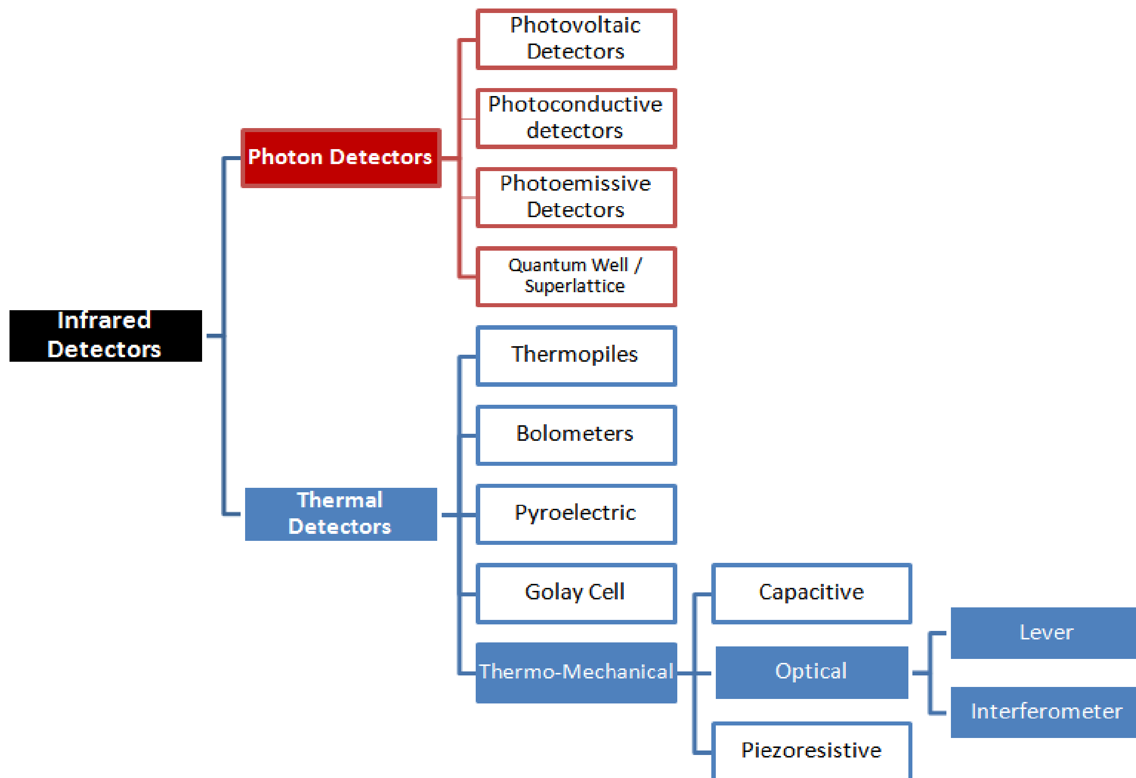

Figure 1.2 IR detector technologies. Photon detectors and thermal detectors are can also be classified as cooled and uncooled detectors. Boxes with blue background illustrate technologies exploited in this research.

Creating the thermal map of the environment finds itself a wide variety of applications in several areas such as medical imaging, military, industrial, surveillance, and rescue. Figure 1.3 shows thermal imaging applications with some example images.

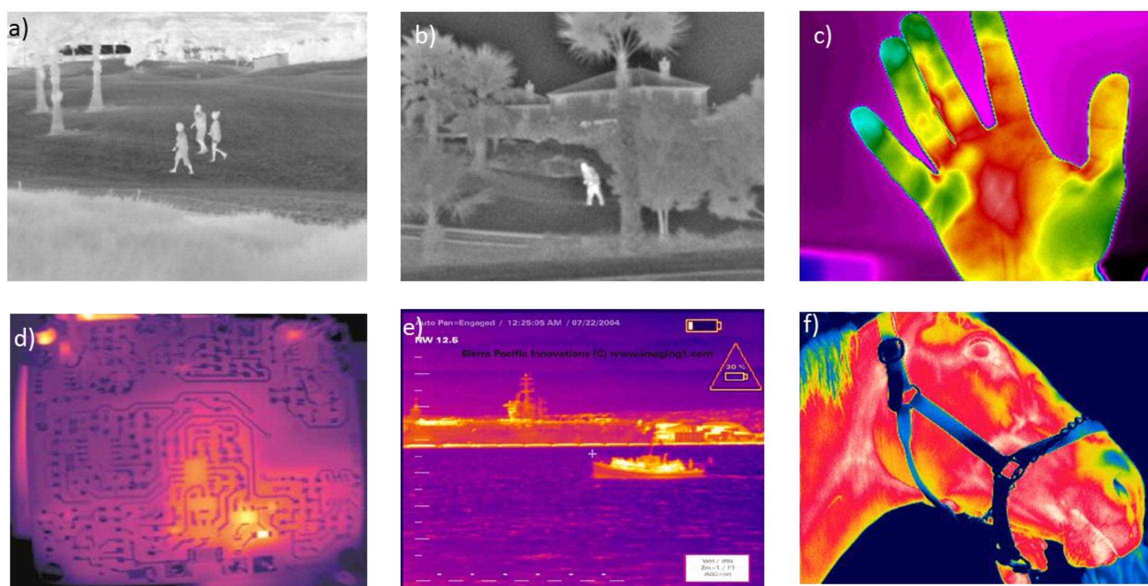

Figure 1.3 Applications of IR imaging: (a) Surveillance (b) Security applications (c) Medical imaging (Infrared Cameras Inc.) (d) inspecting electronic circuits (e) military target detection (f) Veterinary applications

1.3 MEMS-based Thermal Detectors

Incident IR radiation causes a temperature change of thermal detectors. This change in temperature is measured by a temperature-dependent parameter of the detector. Mechanical bending of thermo-mechanical detectors, resistance of bolometers, voltage of thermopiles, electrical polarization in pyroelectric detectors are examples of temperature-dependent parameters. Thermal detectors occupy a wider range in the wavelength spectrum compared to photon detectors. For this type of detectors, large response values require small thermal mass and well-isolated structure for optimum performance. But these parameters are related with time constant of the detector, therefore there must be a trade-off between response rime and responsivity for an optimal performance. Bolometers and

thermo-mechanical detectors are reviewed in the subsequent chapters since these types have similar structures and compete in performance.

1.3.1 Bolometers

Working principle of bolometers is based on the variation of electrical resistance of a material according to its temperature coefficient of resistance (TCR) caused by absorption of incident infrared radiation. A thin metal layer [4], [5] or a semiconductor material [6] can be used as the absorption layer. For metal layer case, the resistance of the bolometer is proportional to temperature, whereas for the semiconductor material case, the resistance is inversely proportional to temperature. For the majority of infrared imaging applications, the bolometers are optimized to detect radiation in the 8-14 μm wavelength regions. There are also bolometers that are optimized for broad-band detection in both the 3-5 μm and the 8-14 μm wavelength regions at the same [7].

The integration capability of bolometer structure with a CMOS readout circuit is an important advantage of the bolometers. Moreover, the current pitch size of 17 μm allows very large format focal plane arrays (FPA) such as 640x480 [8].

The selected bolometer temperature sensing material has a large influence on the sensitivity of the bolometer. A high TCR and a small 1/f noise constant are desirable material properties. At the same time, it must be possible to integrate the temperature sensing material together with signal read-out electronics (e.g. a CMOS wafer) in a cost efficient way. The most common bolometer temperature sensing materials are vanadium oxide (VO_x) and amorphous silicon (a-Si). VO_x is used in a variety of bolometer products but it is not CMOS compatible and requires a separate fabrication process due to contamination reasons. The amorphous silicon bolometer arrays that have been developed take advantage of the high TCR, relatively high optical absorption coefficient and the

advantage that they can be manufactured using silicon fabrication compatible processes. Table 1-1 shows an overview of the main suppliers, the bolometer technology and specifications for existing products and for bolometer arrays [9].

Company	**Bolometer type**	**Array format**	**Pixel pitch**	**NETD** (f=1, 20-60Hz)
FLIR, USA	VO_x bolometer	160x120-640x480	25	35 mK
L-3, USA	VO_x bolometer a-Si bolometer	320x240 160x120-320x240	37.5 30	50 mK 50 mK
BAE, USA	VO_x bolometer VO_x bolometer	320x240-640x480 160x120-640x480	28 R&D: 17	30-50 mK 50 mK
DRS, USA	VO_x bolometer VO_x bolometer	320x240 320x240	25 R&D: 17	35 mK 50 mK
Raytheon, USA	VO_x bolometer VO_x bolometer	320x240-640x480 640x512	25 R&D: 17	30-40 mK 50 mK
ULIS, France	a-Si bolometer	160x120-640x480	25-50	35-100 mK
Mitsubishi, Japan	Si diode bolometer	320x240	25	50 mK
NEC, Japan	VO_x bolometer	320x240	23.5	75 mK
SCD, Israel	VO_x bolometer	384x288	25	50 mK

Table 1-1 Commercial and state-of-the-art R&D uncooled infrared bolometer arrays.

1.3.2 Thermo-Mechanical Detectors

Recent advances in MEMS systems have led to the development of uncooled IR detectors operating as thermo-mechanical detectors Thermo-mechanical IR detectors detects mechanical bending or rotation of a sensor using optical [10] or capacitive [11]

methods. Main advantage of thermo-mechanical approach is the high sensitivity, simple fabrication and low cost. These sensing structures were originally invented at the Oak National Laboratory (ORNL) in the mid 1990's [10, 12-15], and subsequently developed by ONRL [16-20], the Sarnoff Corporation [11, 21], Sarcon Microsystems [22-24] and other for imaging [25, 26] and photo spectroscopic applications [27, 28].

In capacitive method, substrate and the moving membrane behave like a parallel plate capacitor. Incident IR radiation deflects the membrane, thus the capacitance is modulated. But this method requires electrical connections for the readout [21].

In optical readout, a diffraction grating interferometer or beam bouncing method is used. The first demonstration of the optical readout for thermo-mechanical detectors is performed by Manalis et al [29]. Performance comparison of bolometers and thermo-mechanical detectors is shown in Table 1-2 [30].

Features	**Bolometers**	**Microcantilevers**
Ultimate sensitivity (mK)	20	3
Response time (ms)	15-20	5-10
Dynamic range	10^4	$> 10^5$
Ease of fabrication	Requires special material that are protected	Standard MEMS fabrication
Operation principle	Detector saturation observed with hot objects	No detector saturation due to cyclic grating readout

Table 1-2 Comparison of bolometers and thermo-mechanical IR detectors.

1.4 MOEMS Thermal Imaging System Developed at Koç University

Uncooled infrared thermo-mechanical sensor array research was started at Koç University in 2004 [1]. This thesis mainly focuses on the development of new smaller pixel designs, new fabrication process for MEMS, CMOS post-processing, and integration of MEMS and CMOS readout IC.

Figure 1.4 illustrates the entire IR imaging system, wherein the incoming IR radiation is converted into heat and mechanical displacement at each pixel. The detector is a suspended structure fabricated on a transparent substrate. The membrane of the detector is connected to the substrate with bimaterial legs and isolation legs. Incident IR radiation is absorbed by the IR absorber layer of the detector. This absorbed energy modulates the temperature of the detector, and bimaterial legs deflect due to this modulation since two materials have different coefficient of thermal expansion. This bending effectively modulates the gap between the substrate and the membrane of the detector.

A diffraction grating interferometer is integrated underneath each pixel of the detector array in order to detect this gap modulation using optical readout with sub nm accuracy. Under each membrane of the pixels there are diffraction gratings, through which the membranes are illuminated. The reflected light from the gratings and the membranes create interference pattern. The displacement of the membranes modulates the output intensity of the diffracted orders. 1st diffraction order of each detector is imaged on to a CCD camera and computer post processing of resulting intensity map image yields to a thermal image of the scene.

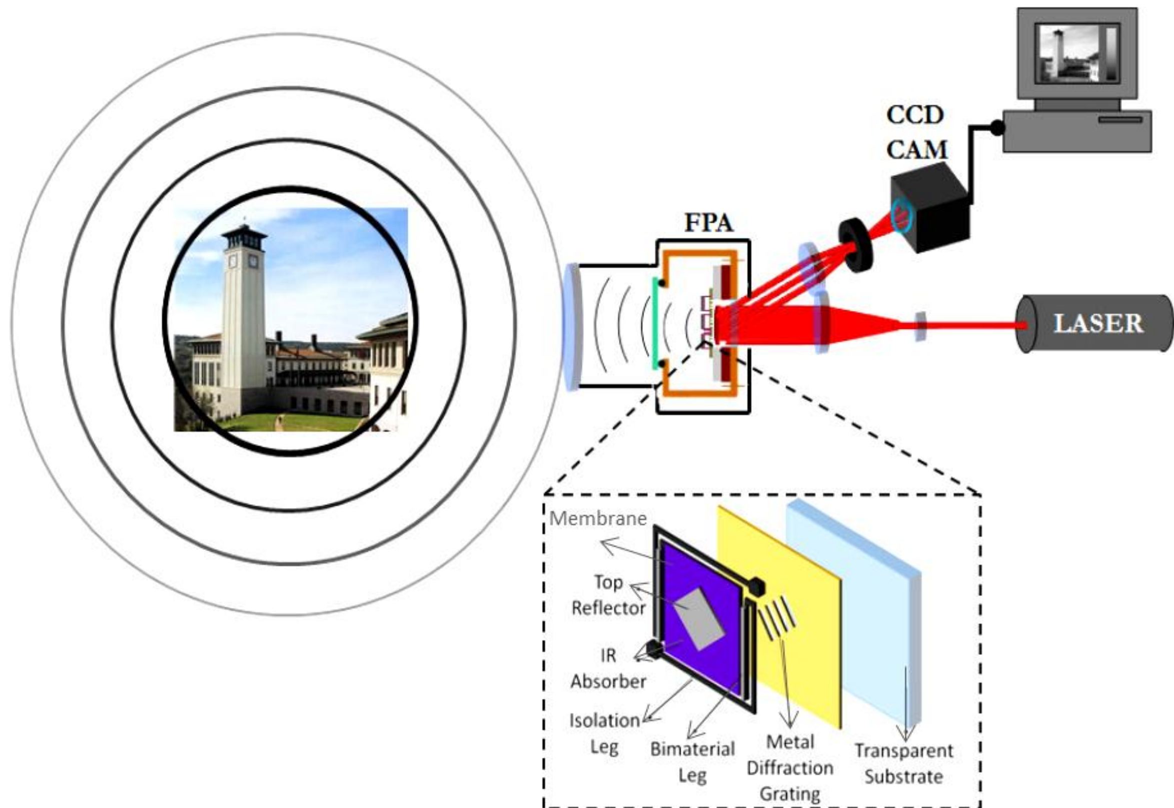

Figure 1.4 Schematic of IR imaging system developed at Koç University

Previous thermo-mechanical IR sensor designs developed at Koç University are given in Figure 1.5 (a,b). Experimental results of these designs are given in Figure 1.5 (c,d) and reported in [31-38].

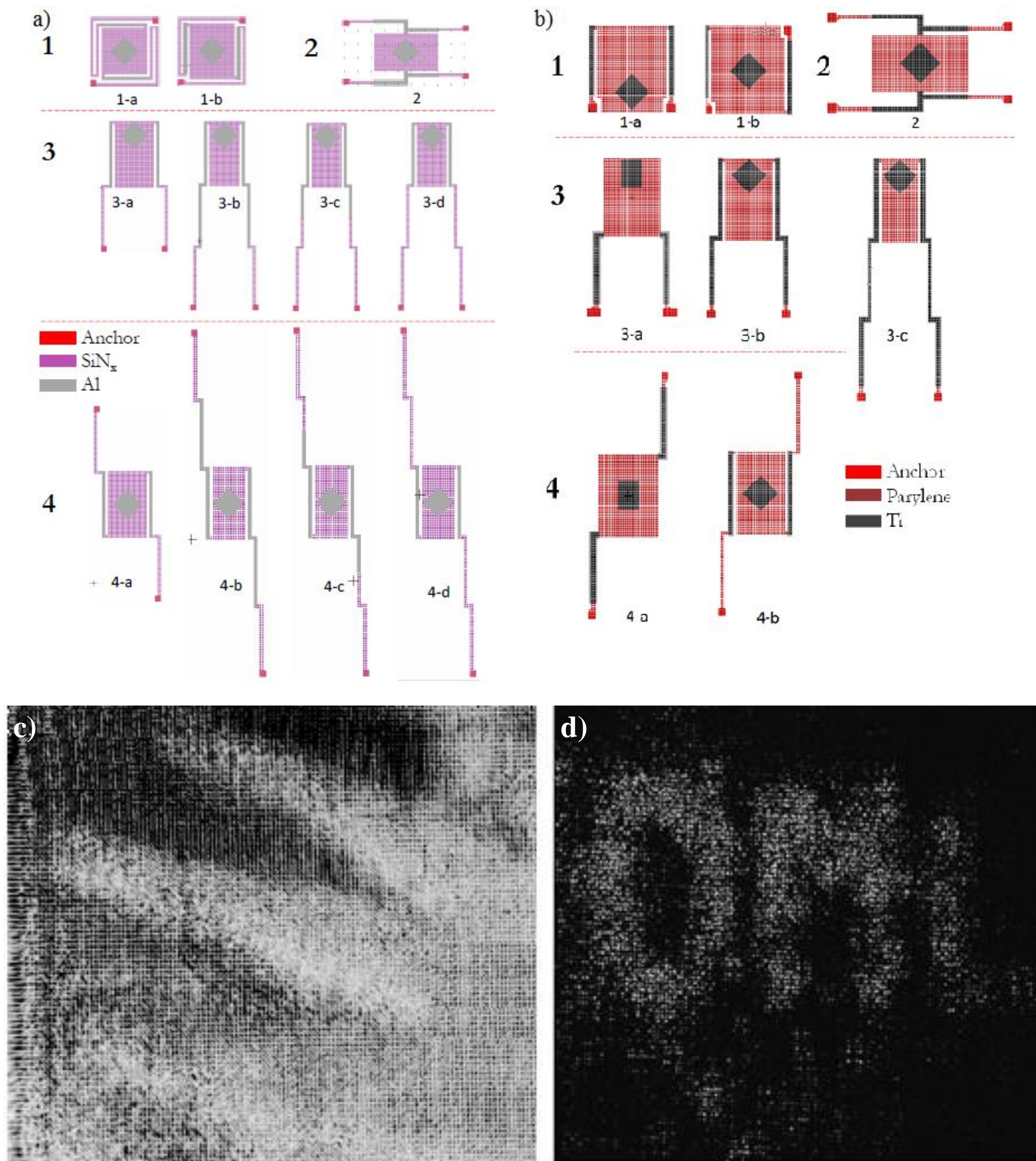

Figure 1.5 (a) Si_xN_y/Al sensor designs. (b) Parylene/Ti sensor designs. (c) IR image of a human hand in front of IR heater. (d) IR image of a labeled plate in front of IR heater captured with Si_xN_y/Al array.

There are several advantages of the thermo-mechanical IR detector approach integrated with an optical readout presented in this work:

- *No electrical connections*: Sensors are electrically isolated from the substrate and decoupled from the readout, thus self-heating due to readout is eliminated.
- *Simple fabrication*: The fabrication of the proposed thermo-mechanical detector requires 4-mask fabrication with standard materials and processes.
- *Sub-nm precision detection:* Diffraction grating based readout is proven to achieve very high precision for detecting small mechanical deflections.
- *Scalability*: The proposed design has the advantage of decoupling the thermo-mechanical sensor array from the readout, providing optimal design of each part to achieve high performance. Pixel size can be decrease and high array sizes can be achieved with this feature.
- *The detector array is immune to saturation* while observing high temperature target by incorporating readout algorithms to extend the range of optical interferometry.
- *The detector array is immune to environmental vibration* since vibration does not change the optical path difference of the readout beam because it affects both the sensor array and the gratings.

1.5 Contributions of the Thesis

Main contributions of this thesis are:

- *Design and fabrication of thermal imaging sensor array at 35um pixel size are completed and tests are continuing.* Array formats are 640x480, 320x240 and 64x64 thermo-mechanical imaging arrays with diffraction grating and lever based optical readout are designed. Silicon nitride based detector arrays are

fabricated at METU-MEMS center and parylene based detector arrays are fabricated at Center of MicroNano Technology (CMi) at Ecole Polytechnique Fédérale de Lausanne (EPFL). Characterizations of fabricated arrays such as minimum detectable temperature measurements, mechanical deflection measurement, time constant measurements, are performed.

- *Post-process on fabricated CMOS Readout Integrated Circuit (ROIC):* A compatible CMOS ROIC for readout of the thermo-mechanical IR detector array was designed and fabricated by Sevil Zeynep Lüleç, who was a MSc student at EPFL. A post-process is performed to etch holes on these chips in order to send a laser beam through these holes for the optical readout. Chips are also thinned down to 100µm thickness.
- *Integration of MEMS detector with CMOS ROIC:* A setup is realized to align 64x64 IR detector array with CMOS chip. Two chips are aligned with 1-2 µm accuracy and integrated.

2 THERMO-MECHANICAL IR SENSOR DESIGN

Thermo-mechanical IR sensor has seven operational structures: transparent substrate, metal diffraction gratings, membrane, IR absorber, bimaterial legs, isolation legs and top reflector as shown in Figure 1.4 inset. As a transparent substrate, pyrex wafers are used during fabrication process. Incident IR radiation is absorbed by a thin film metal lying on top of the membrane. Temperature change created by absorbed radiation bends the bimaterial legs, which are composed of two materials with different coefficients of thermal expansion. Isolation legs thermally isolate the detector from the substrate; moreover thermal response of the detector depends on them. Deflection of the detector changes the gap between the substrate and the detector membrane. This gap is detected using the diffraction gratings and the top reflector. These structures are illuminated with a laser beam through transparent substrate and the beam gets diffracted from the diffraction grating structure. The intensity of diffraction orders depends on the distance between the reflector and gratings. This intensity modulation is monitored with a detector positioned at 1st diffraction order. Thus, a thermal map of the target is generated.

2.1 Design Parameters

There are many design parameters that are to be optimized for high performance of the detectors. First parameter is IR absorption. Thin film metal absorbers give high absorption and low thermal mass, which are critical performance parameters for IR detectors. In order to obtain high performance, efficient absorption of IR radiation is critical. Moreover, low thermal mass is important to keep the thermal time constant low [39]. The required properties and optimization of the absorber layer will be covered in the next chapter.

The photodetector signal is the parameter that depends on the temperature of the sensor. Temperature change modulates the gap between reflector and gratings, and the detector signal depends on this displacement. The parameters that determine the sensitivity are deflection per temperature change of the detector and thermal conductivity G that can be expressed as:

$$G = \frac{kA}{L} \tag{2-1}$$

where k is thermal conductivity of the material, A is the cross sectional area of the isolation leg and L is the length of the isolation leg. Bimaterial portion of the leg has metal, which is a good thermal conductor; therefore G can be calculated considering only the isolation part of the leg without the metal. The thermal time constant τ of the system can be expressed as:

$$\tau = \frac{C}{G} = \frac{\rho c V}{kA/L} \tag{2-2}$$

where C is the heat capacity, ρ is the density, c is the heat capacitance, and V is the volume of the structural material (volume of the legs can be neglected due to its low volume compared to the structural material). Good thermal isolation results in high temperature increase at the membrane but on the other hand, it results also in a large thermal time constant. Adjusting the lengths of the bimaterial and isolation parts of the leg determines the trade-off between how fast the sensor is and how good the sensitivity is. This is the main design tradeoff in thermo-mechanical IR sensors.

The performance of a thermo-mechanical detector depends also on noise sources. Main noise sources for a thermo-mechanical IR sensor are background fluctuation noise, temperature fluctuation noise, thermo-mechanical noise, laser intensity noise and optical readout noise, which are discussed in detail elsewhere [1, 3].

The readout of the designed detector arrays is accomplished optically by using diffraction gratings, which brings a high temperature sensing capability. The intensity of the diffracted 1st order changes sinusoidal with respect to displacement of the membrane, and the expression of the intensity is given in Eq. 2-3 [3]:

$$I_n \propto sin^2(\frac{2\pi}{\lambda}g) \quad (2\text{-}3)$$

Where n is the nth diffracted order and g is the gap between the top reflector and the diffraction gratings. As shown in Figure 2.1, the period of I_n is λ/2 and if the membrane of the detector bends ± λ/8 from initial gap (g_{in}) to each side during heating and cooling, this displacement can be detected using the full range of the CCD camera.

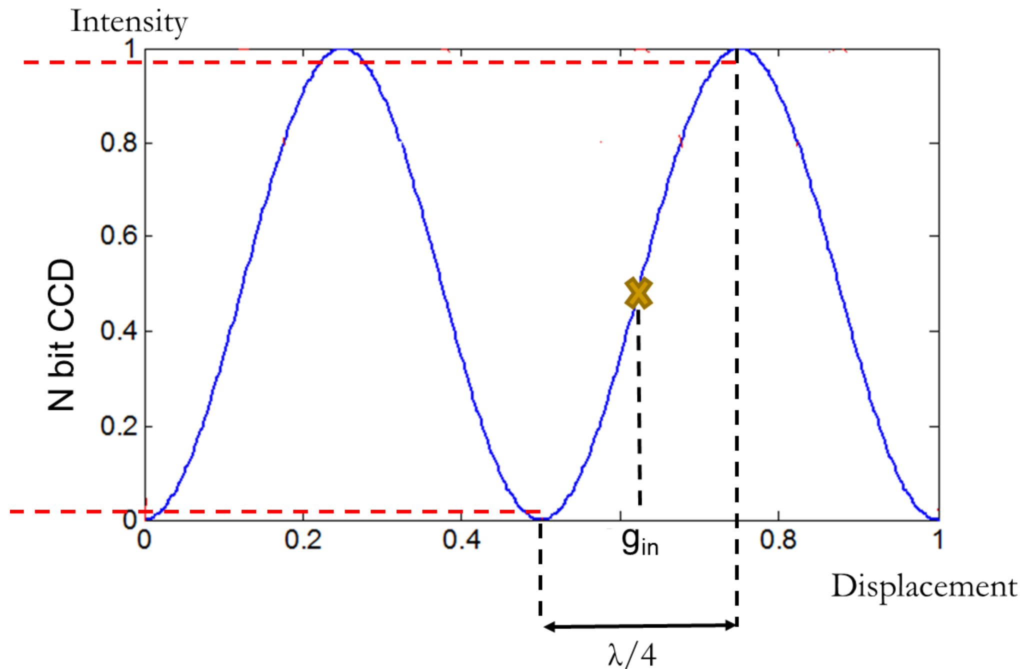

Figure 2.1 Diffraction order intensity vs. displacement of the membrane.

This condition can be expressed as:

$$\frac{dz}{dT_d}\frac{dT_d}{dT_t}(T_{max}-T_{min})=\frac{\lambda}{4} \tag{2-4}$$

where z is the displacement of the membrane, T_d is temperature of the detector, T_t is temperature of the target, T_{max} and T_{min} are the minimum and the maximum target temperatures. The conversion ratio between T_d and T_t can be expressed as:

$$\frac{dT_d}{dT_t}=\frac{\eta(\beta.A)(dP/dT)_{8-14\,\mu m}}{4(f\#)^2G} \tag{2-5}$$

where η is detector absorbance, β is the fill factor of the detector, A is detector area, $(dP/dT)_{8\text{-}14\mu m}$ is radiated power change per temperature for the wavelength between 8-14 µm of the spectrum and f# or the f-number is the focal length to diameter ratio of the imaging lens.

With all the parameters explained above, the targeted specifications of the thermal imager system are given in Table 2-1. Several detector designs will be explained below that can meet the Eq. 2-4 and all the criteria mentioned in Table 2-1.

Detection band	8-14 µm (LWIR)
Array format	640x480, 320x240, 64x64
Detector pitch size	35 µm
f#	1
Video frame rate	30 fps

Table 2-1 Specifications of the thermo-mechanical IR sensor array

2.2 Material Selection

Thermo-mechanical effect occurs when the materials composing the bimaterial legs have large coefficient of thermal expansion (CTE) mismatch. It is important to select the material combinations that will result in high displacement. The materials that are commonly used in MEMS and microelectronics are given at Table 2-2. Silicon nitride (Si_xN_y) & aluminum (Al) and parylene C & titanium (Ti) are selected for our designs. Parylene N seems to have a larger CTE mismatch but this material was not available in the cleanroom wherein the fabrication process was performed.

Material	CTE: α (10^{-6} K^{-1})	Young's modulus: E (GPa)	Thermal conductivity: k (W/K)	Heat capacity: c (J/kg.K)	density (kg/m^3)
Si_xN_y	**0.8**	180	**18.5**	690	2400
SiO_2	0.4	67	1.4	1000	2660
Al	**25**	69	**237**	908	2700
Au	14	80	318	130	19400
Ti	**8.6**	116	**22**	530	4500
Cr	5	279	94	450	7190
Parylene C	**35**	3.2	**0.082**	1000	1289
Parylene N	69	2.4	0.120	1300	1110
Polyimide	4	20	0.12	1090	1420

Table 2-2 Thermal and mechanical properties of selected MEMS materials.

Silicon nitride is a commonly used material in MEMS structures since it forms a high CTE mismatch with aluminum or gold (Au) that can be used as the structural material for thermo-mechanical IR sensors [37].

Another selected material for structural layer of our designs is parylene. Parylene is a polymer that is commonly used in many applications such as bimaterial actuators [40, 41], electrostatic actuators [42], biomolecular spectroscopy [43], pressure transducer [44] and bolometer [45]. It is also a suitable material for the structural layer of thermo-mechanical IR sensor with its high CTE and thermal isolation properties. Moreover, it forms a good match with titanium due to high mismatch of CTE and strong adhesion property of Ti.

The fabrication of the parylene based thermo-mechanical IR detectors is performed using photoresist as sacrificial material and there are many groups who used the same materials as structural and sacrificial layers. A group from Caltech fabricated actuator for micro adaptive flow control using photoresist as the sacrificial material and they released their devices with acetone [46, 47]. They also proposed a dry release process using BrF_3 for large freestanding parylene structures [48]. Another group from Caltech demonstrated parylene neuro-cages for live neural network study with 2µm hardbaked photoresist as a sacrificial layer [49]. Liu et al. fabricated suspended sensor structures with parylene and photoresist and they dried the structures with IR lamp after release with acetone in order to prevent stiction [50]. Using the same method, Guiterrez and Meng reported parylene based transducer in 2010 [51]. Majumdar et al. used critical point dryer to release their parylene based capacitive sensor to prevent stiction [52]. Torun et al. fabricated probes with parylene membranes for biomolecular force spectroscopy using photoresist as a sacrificial material and used acetone and supercritical dryer to release these structures [53].

2.3 Mechanical and Thermal Design

This section explains thermo-mechanical IR sensor designs of Si_xN_y/Al and parylene/Ti material combinations. Thickness optimization of the materials is performed with ANSYS finite element analysis software. Deflection per applied temperature and stiffness of the

devices are also calculated using ANSYS. Noise equivalent temperature differences (NETD) of the designs are calculated using the results of these simulations. For the minimum NETD values, the length of bimaterial part of the legs is investigated.

2.3.1 Si_xN_y/Al Sensor Design

Among the design parameters mentioned above, the most important one for the nitride-based designs is the conductivity value. The designs should have very long isolation legs for an optimum G value since the thermal conductivity of silicon nitride is relatively high. Thus, the fill factor of the Si_xN_y/Al designs is lower than parylene/Ti ones.

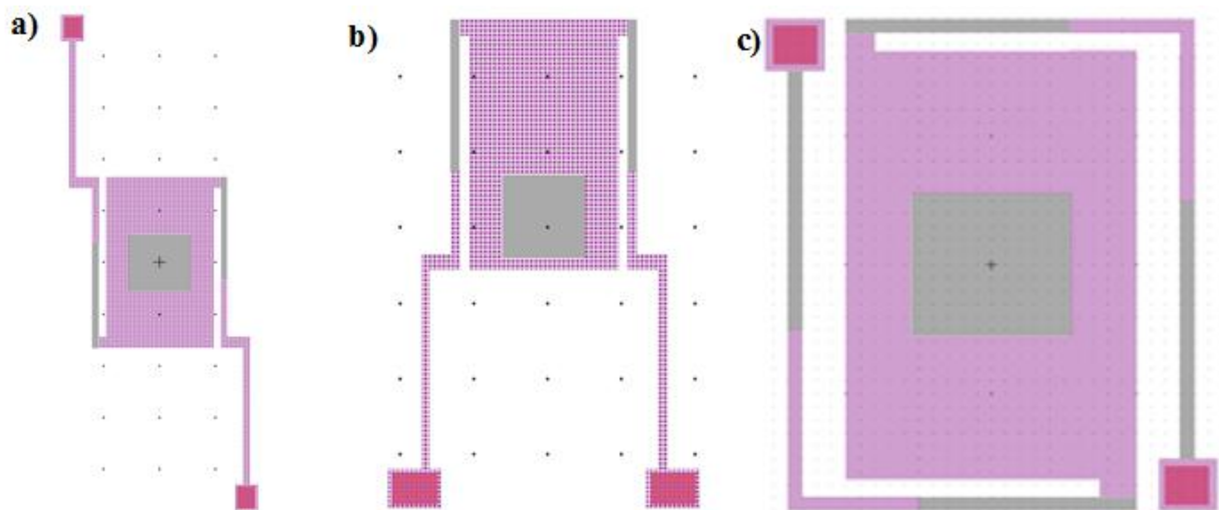

Figure 2.2 Si_xN_y/Al IR sensor designs: (a) Two end fixed design. (b) One end fixed design. (c) Design not requiring TEC.

Figure 2.2 illustrates three sets of Si_xN_y/Al designs. First two designs are one end fixed and two end fixed designs respectively that are composed of two legs with two joints. Two end fixed designs make a piston motion parallel to the substrate whereas the two end fixed designs make both piston motion and tilt motion. The third design is a crab leg design, where two legs with one joint surround the absorbing membrane. But this design is immune to ambient temperature changes and does not require thermo-electric cooling [54]. There are two bimaterial parts on a leg; heat due to incident IR radiation transfers to the one near the membrane and deflects the structure, but the isolation part of the leg prevents the heating of the other bimaterial part that is near the anchor. On the other hand, when the ambient temperature fluctuates, it heats up both bimaterial parts at steady state, but they deflect the structure in opposite directions, thus there is no effective deflection of the membrane.

2.3.2 Parylene/Ti Sensor Design

Parylene/Ti sensor designs that are shown in Figure 2.3 have very short isolation legs because parylene has a low thermal conductivity. Thus, the fill factor of the designs increases. Parylene/Ti sensors were designed by modifying the Si_xN_y/Al designs except the 4-leg design, but they have shorter isolation legs. Two end fixed design in Figure 2.3 (a) and 4-leg design in Figure 2.3 (c), which is borrowed from [1] make an out of plane motion, whereas one end fixed design in Figure 2.3 (c) makes both out of plane motion and tilt motion.

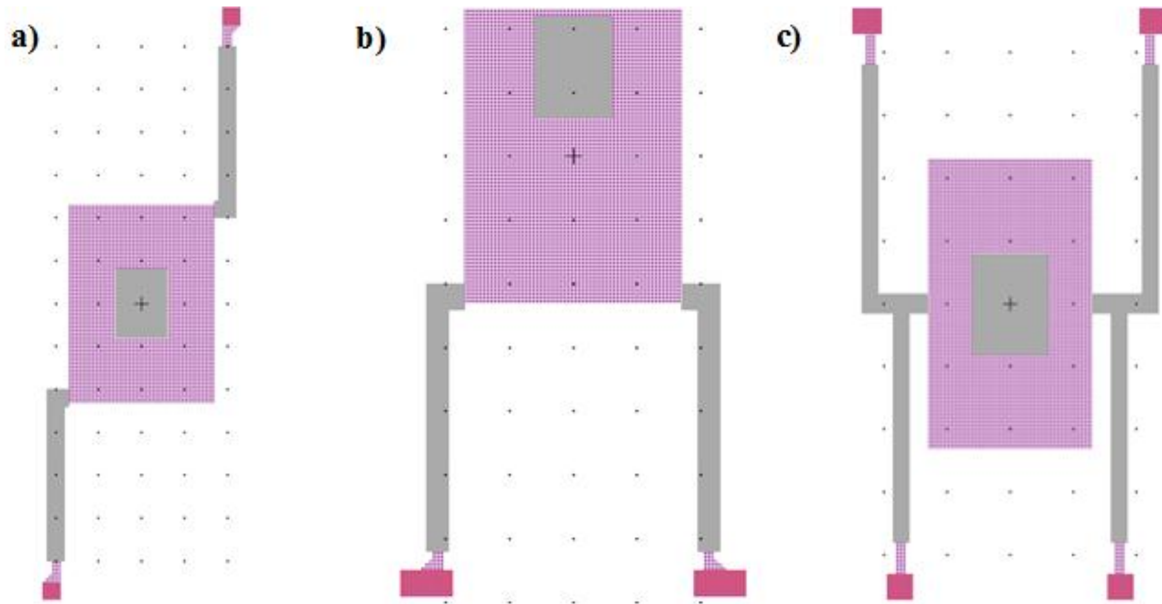

Figure 2.3 Parylene/Ti IR sensor designs: (a) Two end fixed design. (b) One end fixed design. (c) 4-leg design.

2.3.3 Finite Element Analysis

Natural frequency, stiffness and displacement per applied temperature values are extracted from the finite element simulation results in order to calculate the NETD values of the designs. Moreover, finite element analysis is also performed for the thickness optimization, length of bimaterial leg optimization and thermal cross-talk analysis. ANSYS finite element simulation software is used for these analyses. For all the analyses, the simulation routine starts with creating the physical model of the design and it continues with assigning the material properties to relevant parts of the structure. Then the device is meshed into discrete element using SOLID98 as the element type. SOLID98 is a coupled

field 10-node tetrahedral element that is used for thermo-mechanical analysis. Meshing size was selected such that further decrease in element size does not change the result.

As an example of thermo-mechanical coupled field analysis, simulation results of self-leveling design is given in Figure 2.4. In the first figure, deflection due to absorbed IR radiation is illustrated. For this case, maximum deflection at the membrane area is 38 nm/K whereas in (b), the deflection of the ambient temperature fluctuation case is given and the effective deflection of the membrane is zero. The most important parameters of these simulations are boundary conditions. For the ambient temperature fluctuation case, only the membrane is loaded with a 1 K temperature load and temperature of all parts of the structure increases by 1 K. On the other hand, for the IR heating case, membrane is loaded again with 1 K temperature load, but the temperature of the anchors is set to 0 K. With these boundary conditions, a temperature gradient is formed on the isolation leg and the bimaterial part near the anchor does not heat up. In the pictures given in Figure 2.4, red color represents the most deflected area whereas blue color shows the non-deflected area.

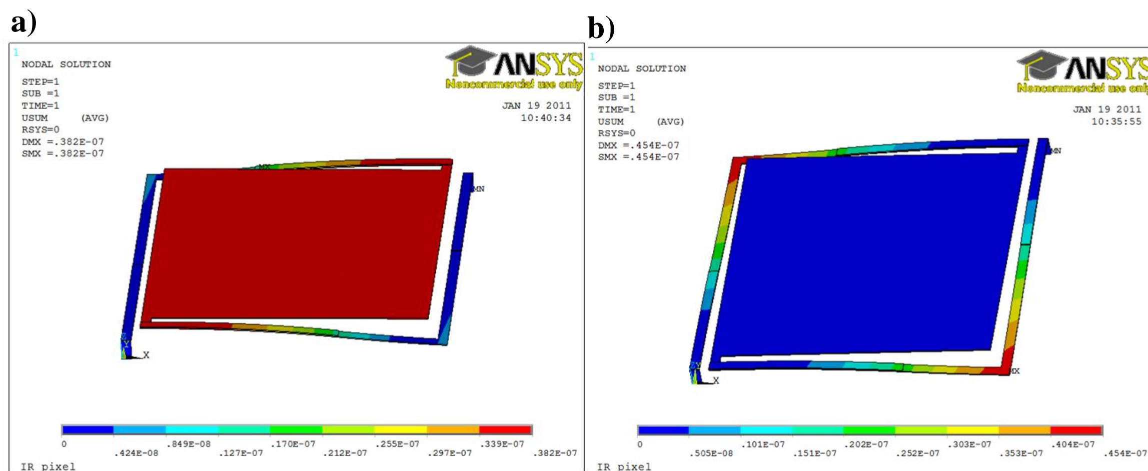

Figure 2.4 FEM simulation for deflection analysis of the design not requiring TEC.

In Figure 2.5, thermo-mechanical simulation result for thermal cross-talk analysis of an old design is given. In this analysis, two adjacent pixels on a metal covered substrate are simulated. The pixel at the right is loaded with 1 K temperature and the maximum deflection is around 16 nm/K. But the pixel at the left is not loaded and the maximum deflection of the membrane is 0.02 nm/K.

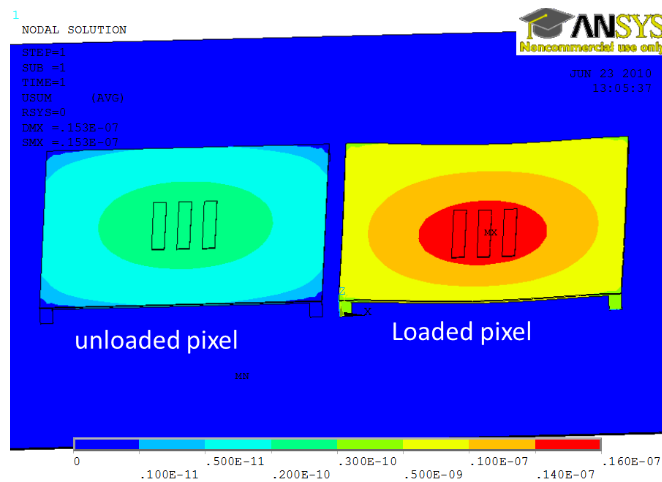

Figure 2.5 Thermo-mechanical simulation results for thermal cross-talk analysis.

As an example of modal analysis, simulation results of two end fixed design of parylene/Ti sensors is given in Figure 2.6. For an optimum performance, the detectors should be tolerant to environmental vibrations, in other words first modal frequency should be much higher than the frequency of operation and the environmental vibrations (at least up to 1 KHz). Simulation results show that the first mode frequency is around 16 kHz, which is much larger than the maximum operation frequency. First three modes of the given design are out of plane motion at 16 kHz, torsion at 34 kHz and rocking motion at 54 kHz. The design deflects at first mode under incident IR radiation because it is the closest mode to the operation frequency and there is a good separation between 1st and 2nd mode.

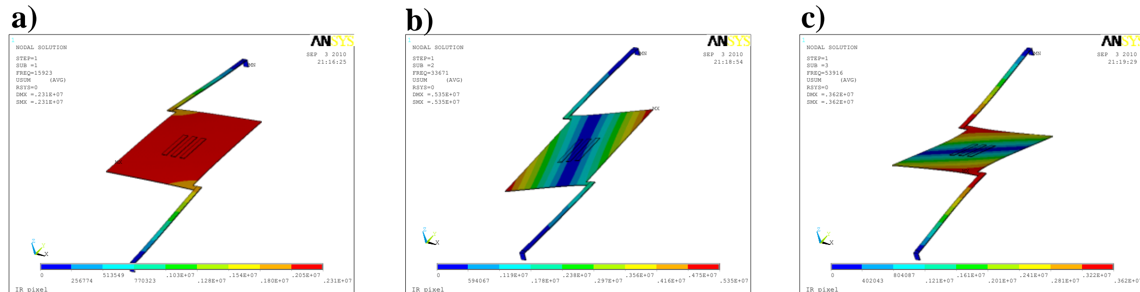

Figure 2.6 FEM simulation for the modal analysis of two end fixed design (first three modes).

2.4 Optical Readout

The deflection of the thermo-mechanical IR sensors is determined by optical methods. The reason behind the suggestion of an optical readout is to avoid the need of electrical interconnects on pixels. Fabrication of detectors should be performed on top of CMOS electronics without optical readout and this makes the fabrication process more complex. More importantly, yield is greatly affected. Joule heating due to electrical bias and thermal crosstalk of detectors via electrical interconnects decrease the performance of Focal Plane Array (FPA). A sub-nanometer resolution for the detection of the deflection of all pixels can be obtained with an optical readout.

Optical readout is basically performed by illuminating the back surface of the MEMS pixel and then checking the properties of the reflected beam using a detector array. Pixel deflections modulate the intensity of incident readout beam, and this modulation is imaged onto a 2D visible detector array. This intensity modulation is achieved either by beam steering (optical lever) or interference based methods (Figure 2.7)

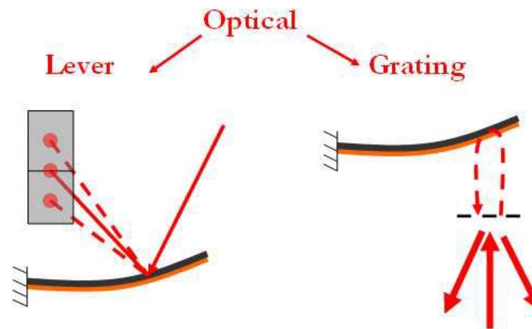

Figure 2.7 Lever and grating based optical readout methods.

2.4.1 Diffraction Grating Method

For this method, pixel level interferometers with diffraction gratings are designed. There are diffraction gratings under each reflector of the pixels, through which the membranes are illuminated by a laser beam. The reflected light both from the gratings and the reflectors create interference. The schematic of the structure is shown in Figure 2.8.

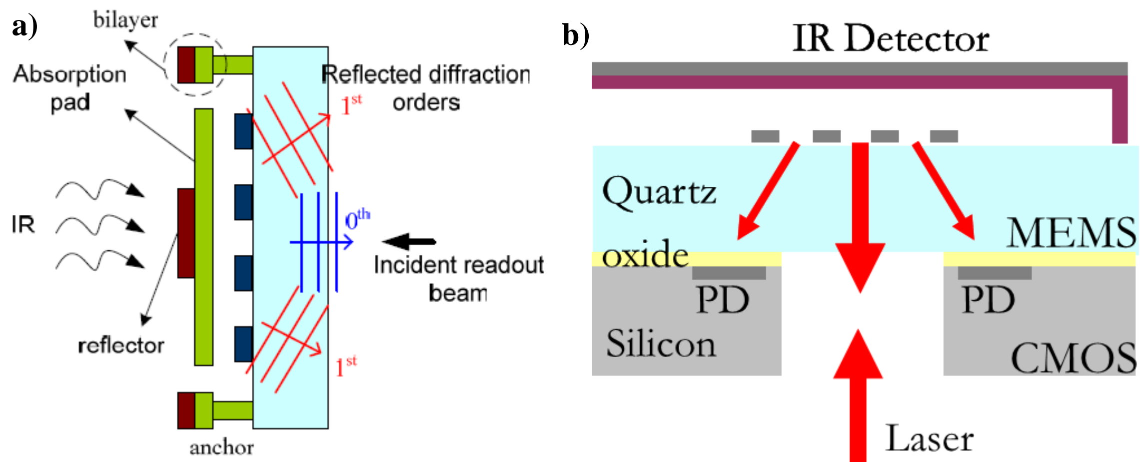

Figure 2.8 (a) Side-view of an IR pixel illustrating grating readout. (b) Grating readout schematic with photodetectors.

The gap between the membranes and the gratings is modulated by the absorbed IR radiation incident on the membranes due to the deflection on bimaterial legs which is caused by mismatch of coefficients of thermal expansion of two materials. This displacement of the membrane modulates the intensity of the reflected beam. Therefore the thermal distribution of the target can be mapped to the intensity of the readout light reflected from the pixels. One can specify how much the membrane displaces by measuring 0th, or $\pm 1^{st}$, or both orders of the reflected light. Therefore, the intensity fell on these orders are important and are given explicitly in Eq. 2-6 and 2-7 [1],

$$I^{0th}(d) = I_{in}\, cos^2(\frac{2\pi g}{\lambda}) \quad (2\text{-}6)$$

$$I^{1st}(d) = \frac{4}{\pi^2} I_{in}\, sin^2(\frac{2\pi g}{\lambda}) \quad (2\text{-}7)$$

where I^{0th} and I^{1st} are the intensities of light going to 0th and 1st diffraction orders, g is the gap between the membrane and the gratings, I_{in} is the intensity of incident beam, λ is the wavelength. Based on the expressions given above, the intensities of the light falling on 0th and 1st diffraction orders are plotted as a function of ration of the gap to the wavelength and illustrated in Figure 2.9.

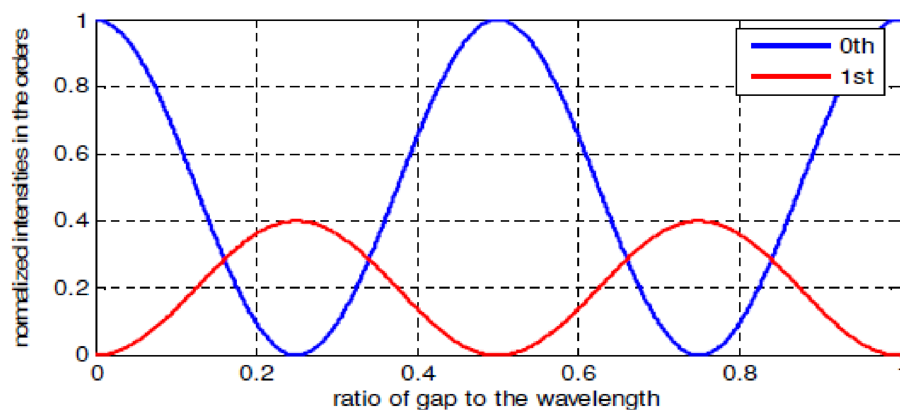

Figure 2.9 Intensity of light going to diffraction orders as a function of the distance from the membranes to the diffraction gratings.

2.4.2 Optical Lever Method

In this method, deflection of the one end fixed sensor changes the cantilever slope. This slope variation reflects the incident beam accordingly. This method is also used in atomic force microscopes (AFM). In this case, a position sensitive detector or a quadrant photodetector is positioned on the path of steered beam, and translation of beam is easily monitored. With this method, a resolution of sub angstrom is realizable. On the other hand, position detection of steered beam is difficult for an FPA that possibly will have overlapping regions of reflected beams from adjacent pixels, so beam translation is transformed into intensity modulation. For this purpose, the designed CMOS readout circuit has a differential readout feature. Two photodiodes are placed and when there is no bending, the light absorbed by each will be the same. When the detector bends up or down due to IR radiation, the light absorbed by one photodetector will increase whereas the other photodetector will start to absorb less light. Detailed analysis of this readout method is explained in [3] and [55]. The schematic of the structure is shown in Figure 2.10.

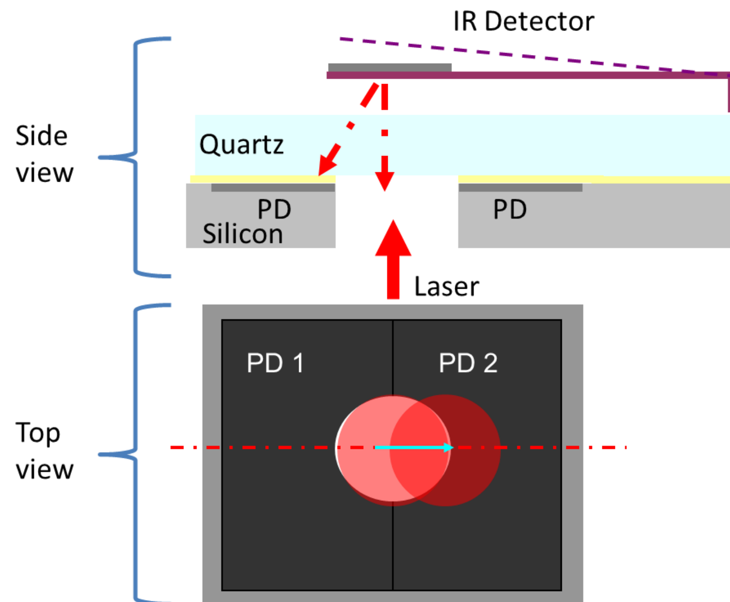

Figure 2.10 Side-view of an IR pixel and top view of photodetectors illustrating optical lever readout.

2.5 System Theoretical Performance

Time constant, fill factor and NETD values of the parylene/Ti and Si_xN_y/Al designs are given in Table 2-3. Calculations of NETD are performed assuming the readout is performed with 10 bit and 12 bit dynamic range CCD cameras and the noise level of the camera is about 1 bit. Si_xN_y/Al designs have very small time constants since thermal conductivity of silicon nitride is higher than parylene. Fill factor of Si_xN_y/Al designs is lower than parylene/Ti ones because they have longer legs, except the self-leveling design, which have 2 legs that surround the membrane. One end fixed parylene-based design performs better since longer legs enable higher thermal isolation and mechanical displacement.

	Design	Fill Factor (β)	NETD (10 bit) [mK]	NETD (12 bit) [mK]	NETD with noise-free readout (12 bit) [mK]	Time Constant (τ) [ms]
Parylene/Ti sensor designs	1-end fixed	60%	140	35	9	7.66
	2-end fixed	60%	809	202	51	11.92
	4-leg	46%	873	218	55	10.85
Si_xN_y/Al sensor designs	1-end fixed	46%	687	171	43	1.42
	2-end fixed	46%	587	146	37	1.39
	Self-leveling	80%	2410	602	150	0.97

Table 2-3 Fill factors, time constants and NETD values of both parylene/Ti and Si_xN_y/Al designs for 10 and 12 bit CCD cameras.

Although designs with long legs show higher theoretical performance, it is more difficult to deal with stress related fabrication issues for these designs. Therefore, it proved to be more difficult to realize the theoretically better performing designs.

In order to achieve better performance, it is possible to take advantage of the binning process in CCD camera based readout. The readout beam that is diffracted from each sensor is mapped to multiple CCD pixels. It is possible to sum all corresponding CCD pixels to achieve the total signal that diffracts from a pixel. Such an addition results in an increase in signal value more than the increase in the noise, which in turn results in an increased SNR that is proportional to the square root of the amount of binned CCD pixels. Binning can provide an extra 2-bit gain on top of the original A/D digitization of the CCD camera by binning 4x4 CCD pixels per thermo-mechanical IR sensor. In other words, NETD values given in Table 2-3 become 4-times better with binning process.

3 FABRICATION OF IR SENSOR ARRAY

In this chapter the fabrication of detector arrays and the vacuum packaging requirements are discussed. A 4-mask fabrication process was developed using standard materials of semiconductor industry. The mechanical design and mask layouts are performed by the author. The devices were fabricated on pyrex wafers to provide a transparent media for optical readout. For metal layers, titanium and aluminum were deposited using both sputtering and evaporating. Polyimide and photoresist are spin coated and cured as sacrificial layer. Silicon nitride and parylene were used as structural layers. In order to pattern the layers, both wet etching techniques and Reactive Ion Etching machines were used.

Fabrication of Si_xN_y/Al arrays was carried out at Middle East Technical University, Microelectronics Center (METU-MET), and the fabrication of parylene/Ti sensor arrays was carried out at Center of MicroNano Technology at Swiss Federal Institute of Technology (EPFL) by the author.

3.1 Si_xN_y/Al sensor array fabrication

Fabrication steps are illustrated in Figure 3.1. Firstly gold gratings are evaporated and patterned onto pyrex substrate. 2 μm of polyimide is deposited as sacrificial material. Thickness of this layer is chosen to be quarter of the IR wavelength, as a resonant gap for optimum absorption. Anchors are patterned on polyimide using O_2 plasma. 150 nm Si_xN_y and 150 nm aluminum are deposited using chemical vapor deposition (CVD) and sputtering. Silicon nitride layer is patterned with RIE as structural layer and aluminum is

patterned with wet etching as bimaterial legs with using one mask for each. The arrays are diced and released with oxygen plasma etch of polyimide. Finally, to increase the IR absorption, a thin layer of titanium nitride (TiN) is sputtered. Some arrays are fabricated without the absorber layer. A thin layer of gold is sputtered for absorption at Surface Science and Technology Center (KUYTAM) at Koç University.

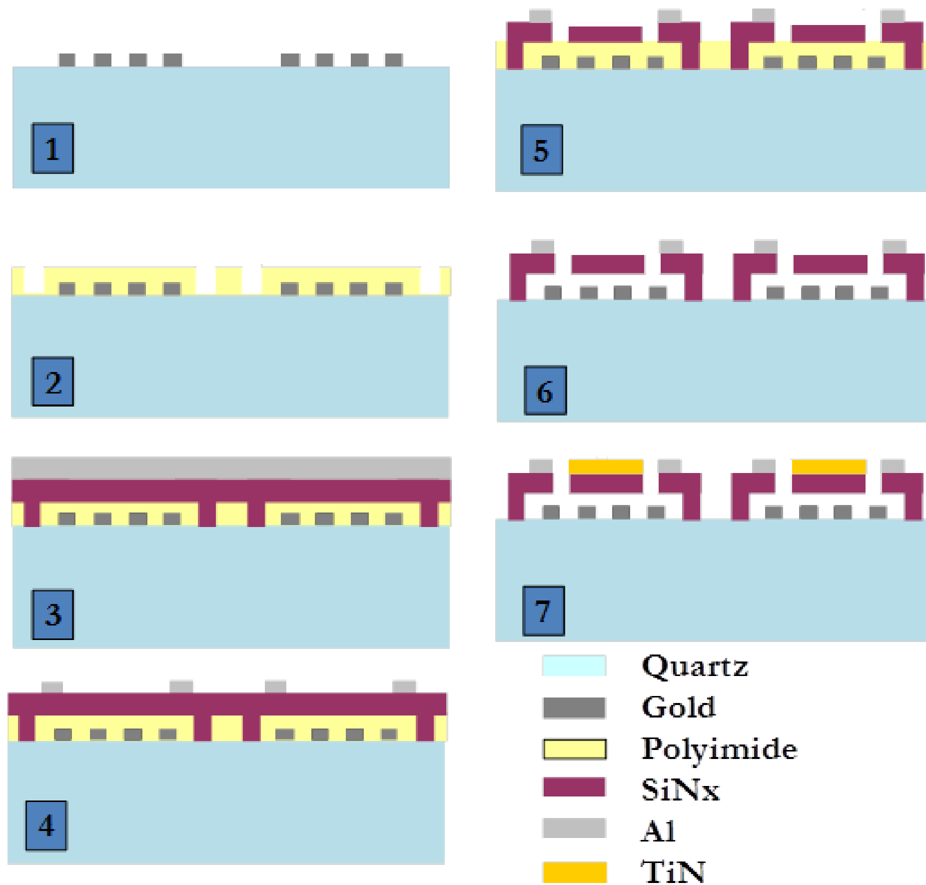

Figure 3.1 Fabrication steps of Si_xN_y/Al sensor array: (1) Gold grating patterning (2) Sacrificial polyimide coating and patterning (3) Blanket deposition of Nitride and Aluminum layers (4) Al patterning with wet etch (5) Nitride patterning (6) Release with oxygen plasma (7) Absorber deposition.

The mask layout was drawn according to the finite element analysis results and sent to METU-MEMS for the fabrication. Each array is placed 5 mm away from the other arrays for dicing purposes. Since a stepper is used during photolithography steps, layout was drawn with a 1 μm lithographic resolution and total area of drawn layout is 22mmx22mm for the compatibility of the stepper configuration. Then the designs were placed on the layout using step&repeat technique. The drawn designs, numbered mask layout and a picture of diced wafer are illustrated in Figure 3.2.

The sacrificial polyimide was removed with an oxygen plasma etcher. Since the plasma etch time is a function of membrane size, the different types of designs on the layout were drawn with the same membrane size. And the time of O_2 etch is optimized for this specific membrane size. But first release results had a bending problem and non-uniformity. Figure 3.3 (a) illustrates microscope images of released sensor arrays. It can be observed that the pixels that are out of focus have a bending problem. Moreover the damaged pixels have a black spot on the membrane area. The bending problem can only be seen in Figure 3.3 (b,c), which shows membrane area out of focus when anchors are focused and vice versa. For more detailed inspection, SEM images of fabricated arrays were taken at KUYTAM, at Koç University with Zeiss EVO LS15 Scanning Electron Microscope. The bending problem at bimaterial legs can only be seen in Figure 3.3 (d,e).

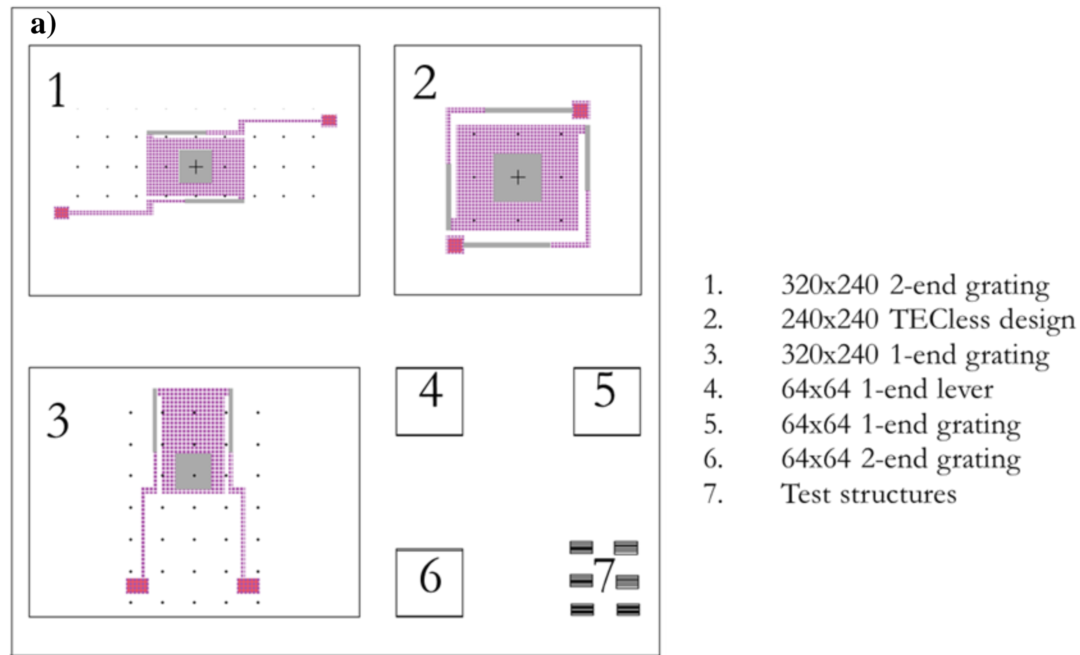

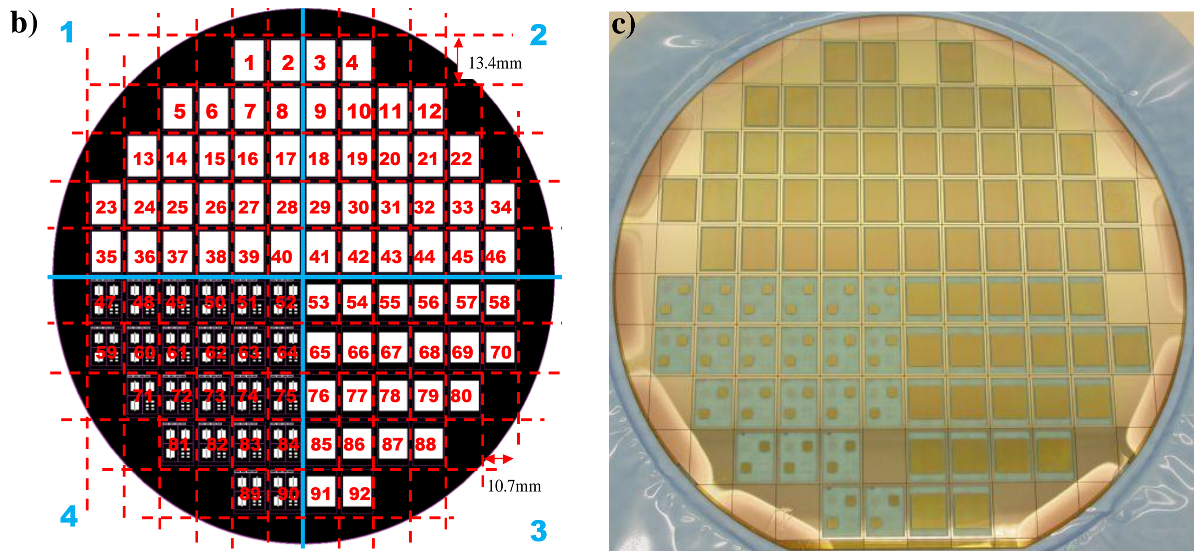

Figure 3.2 (a) Drawn designs. (b) Numbered mask layout. (c) Diced wafer after fabrication

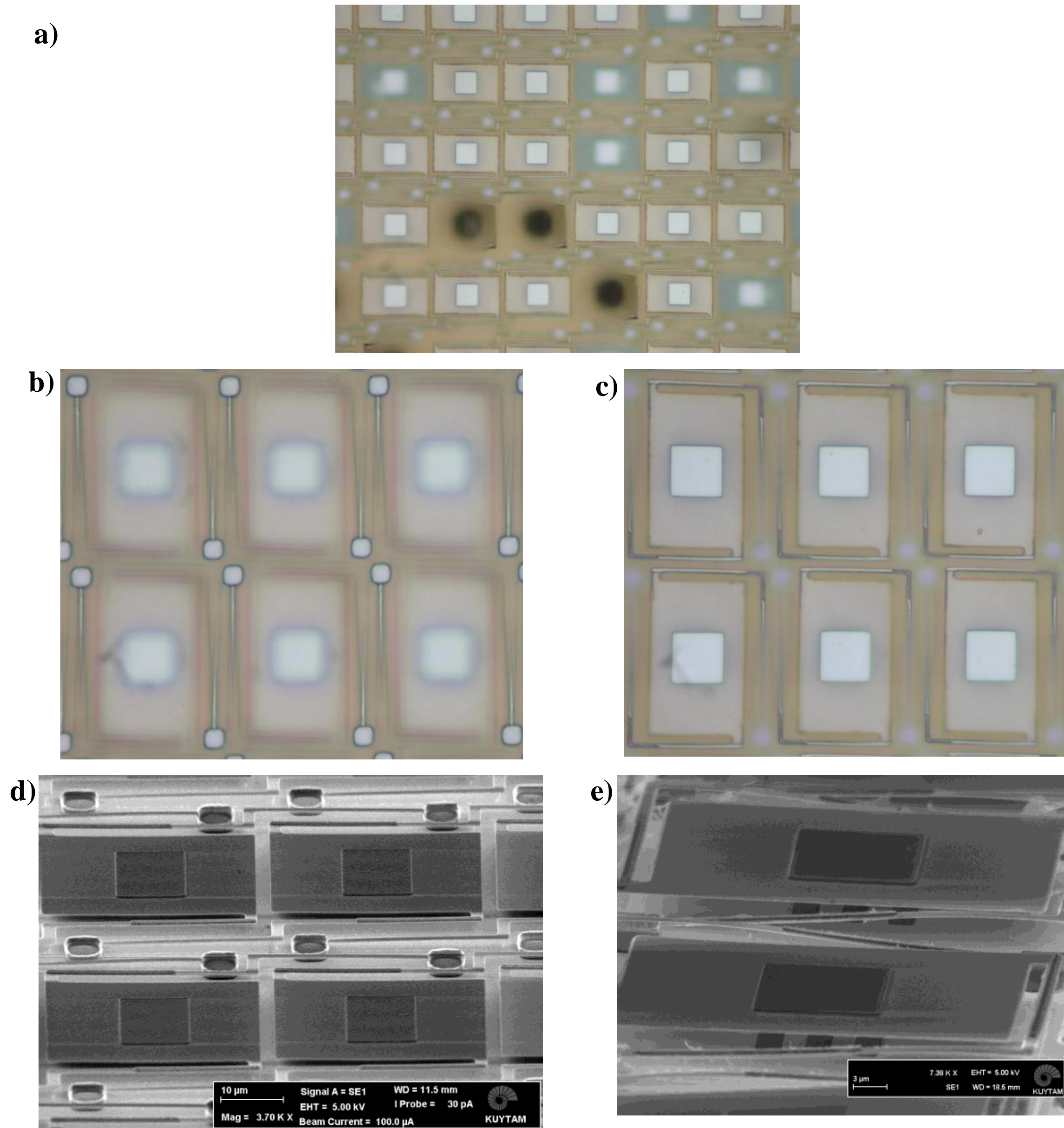

Figure 3.3 Fabricated Si_xN_y/Al sensor arrays: (a) microscope image of 6x5 array. (b,c) microscope images of 3x2 array. Bending of legs is shown. (d) SEM image of successfully fabricated sensor array. (e) SEM image of two pixels with bended legs.

For more inspection purposes, measurements with white light interferometer, ContourGT in Motion of Bruker were taken. The uniformity problem of fabricated arrays was verified after comparing these results with optical microscope images. Figure 3.4 (a,b) illustrates one microscope image and one optical profiler measurement of a large array, and non-released pixels can be both seen in these images.

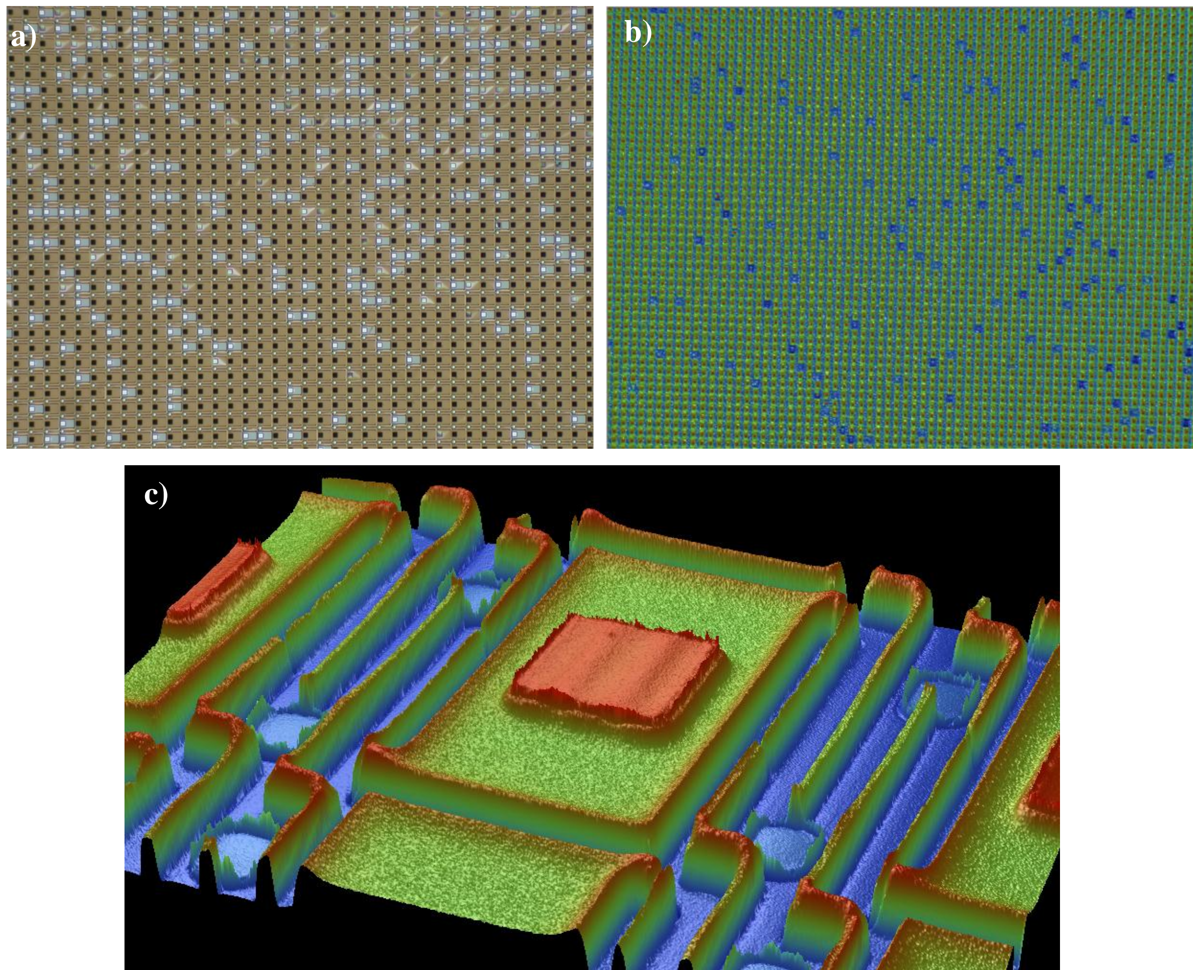

Figure 3.4 Fabricated Si_xN_y/Al sensor arrays: (a) Microscope image of a fabricated array showing non-released pixels. (b) Optical profiler image of the same array. (c) Optical profiler image of 2-sided design.

The measurements taken with white light interferometer are used also to confirm the fabrication results. Figure 3.5 illustrates profile measurements of one released pixel. X profile shows the profile on the horizontal red line, and it can be observed that top of the reflector is 2.3 µm above from the substrate which is expected because the gap between the membrane and substrate is 2 µm and the thicknesses of silicon nitride and aluminum are 150 nm each. The bending problem of the process can also be seen in this image. It can be observed that the bimaterial legs and membrane part of the pixel are not in the same height level.

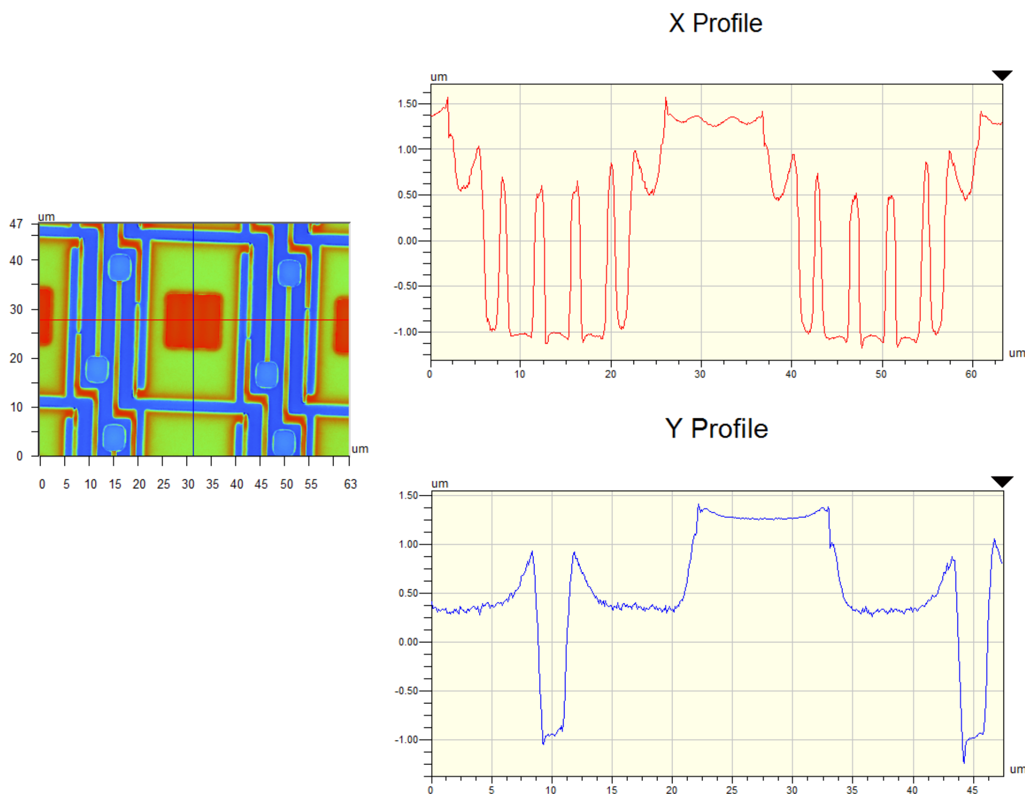

Figure 3.5 Detailed profile measurement taken with white light interferometer.

3.2 Parylene/Ti Sensor Array Fabrication

The fabrication process of parylene/titanium sensor arrays is similar to the fabrication of nitride-based sensors however the fabrication steps of parylene-based sensors will be explained more detailed since the process was performed by the author. Fabrication of parylene/Ti arrays was carried out at Center of MicroNano Technology (CMi) at Ecole Polytechnique Fédérale de Lausanne (EPFL) in 2010 and 2011.

The photolithography masks were designed according to finite element analysis results but due to process limitations, they were designed such that the minimum line width is 1.5 μm. The layout has also some variations in pitch size and array size. Layout and design variations are illustrated in Figure 3.6.

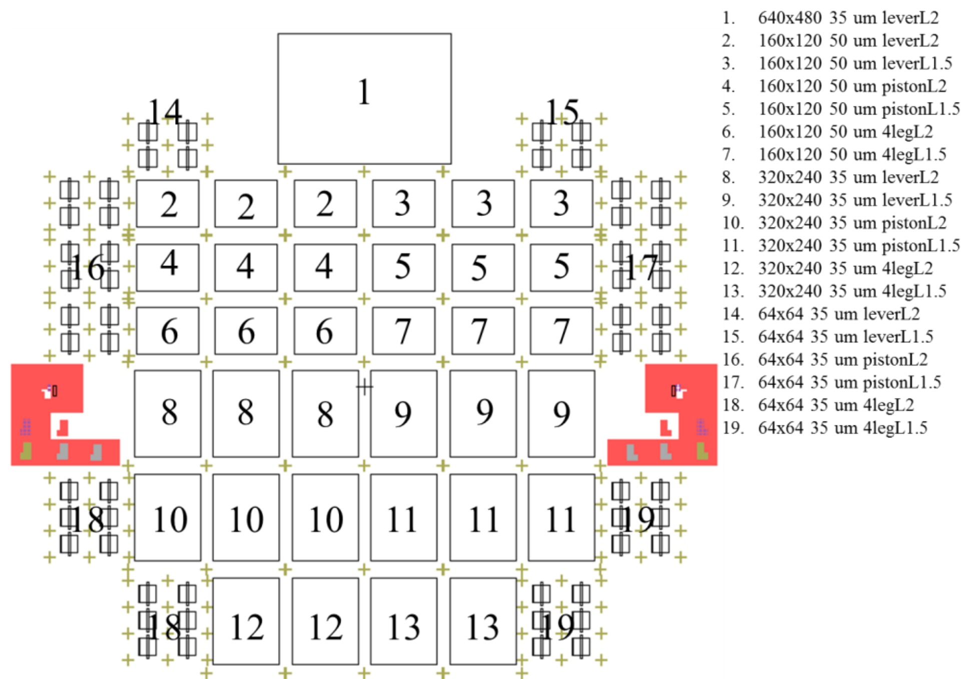

Figure 3.6 Mask layout of parylene/Ti sensor arrays.

3.2.1 Process Flow

A 4-mask process was developed and optimized with standard materials that are commonly used in MEMS area. A schematic of the final process flow is given in Figure 3.7. Each step of the process is explained below.

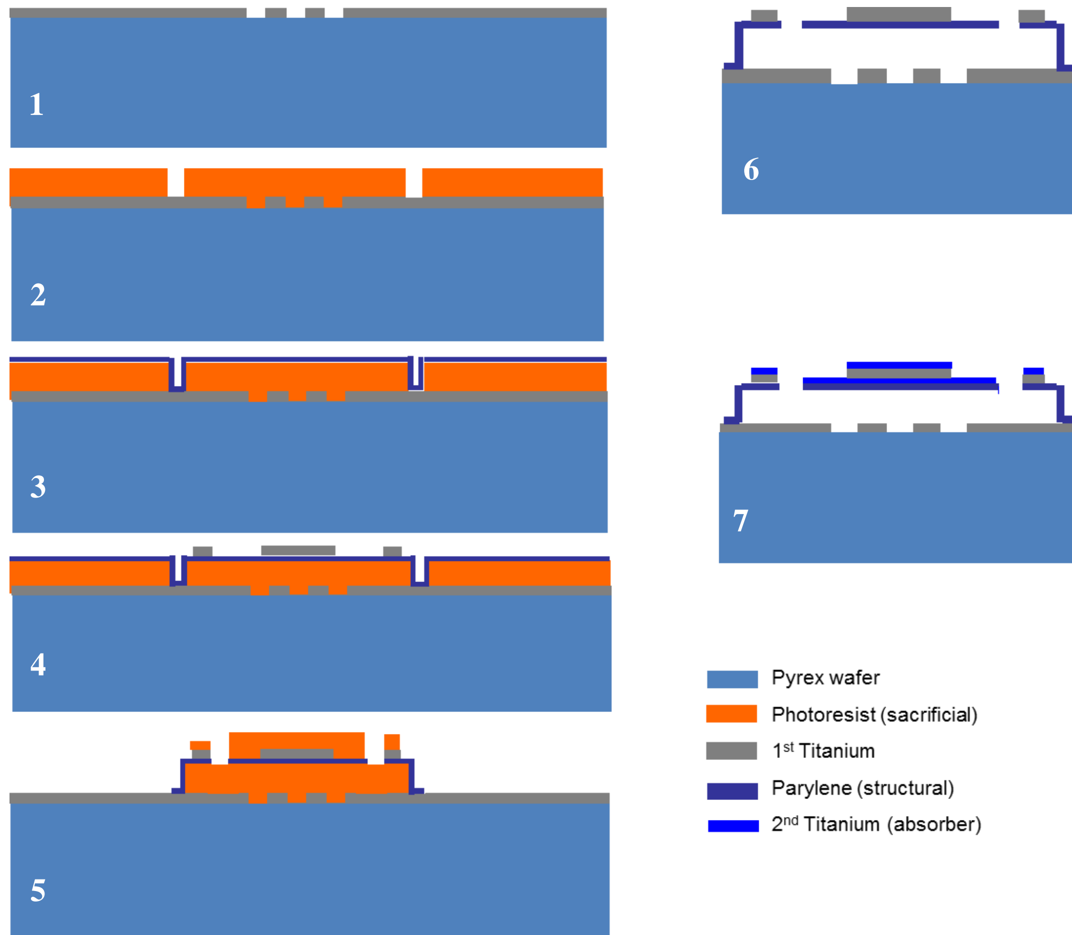

Figure 3.7 Fabrication steps of Parylene/Ti sensor array: (1) Titanium grating patterning (2) Sacrificial photoresist coating and anchor patterning (3) Blanket deposition of parylene (4) Ti deposition and patterning (5) Parylene dry etching (6) Release with resist remover and critical point dryer (7) deposition of absorber layer.

3.2.1.1 Wafer Preparation

Wafer surface cleaning before subsequent processes is performed for each run. For this purpose, 10 minutes of oxygen plasma with 500 W power was performed for every pyrex wafer of 525 μm thickness.

3.2.1.2 Lift-off

Lift-off process is a method of patterning a target material, mostly metal, on the surface of a substrate using photoresist. In this process, 100 nm of Titanium layer is patterned as diffraction gratings on a pyrex wafer. Lift-off step is divided into three sub-steps as follows: Photoresist spinning, photolithography, metal deposition and patterning.

3.2.1.2.1 Photoresist Spinning

Lift-off process is performed with lift-off resist (LOR). LOR is a polymer that dissolves in an alkaline solution. LOR is used as a sacrificial material and it can be under etched with standard developers of positive photoresist just by extending the development time of the imaging top resist. This method is known as the double layer lift-off or bi-layer lift-off. Photoresist AZ1512HS is selected as associate imaging resist. For the success of lift-off process, maximum layer thickness of deposited metal should not be larger than 70% of the photoresist thickness. Firstly 400 nm of LOR is spin coated with a spin speed of 6500 rpm and spin time of 30 seconds. Then 1.6 μm of AZ1512 photoresist is spin coated with a spin speed of 2800 rpm and spin time of 30 seconds using automatic resist processing cluster EVG150.

3.2.1.2.2 Exposure and Develop

Exposure in each photolithography step was performed using Suss Microtec MA6&BA6 and MJB4 mask aligner. The exposure time was first calculated theoretically

using the information on the clean room's web site, and then the correct exposure time was found experimentally by varying the exposure time. For this first mask, exposure time was 1.2 seconds, alignment gap was 40 μm, light intensity mode was Constant Power (CP), light power intensity was 10 mW/cm^2 and electrical power consumption was 275 W. Due to presence of the LOR layer, reflection of light is slightly reduced; therefore the corrected exposure time was less than the calculated one.

The exposed wafers were then developed by AZ 726MIF using EVG150. Spin-Rinse-Dryer step was performed after each develop step to avoid contamination on other equipments during further processing steps.

3.2.1.2.3 Metal Deposition and Patterning

The metal deposition for the lift-off process was performed with Leybold Optics LAB 600H evaporator. Sputtering covers the resist step and consequently an ultrasonic bath is needed for cutting the weakened metal link along the sidewalls and this action may damage the structures. Therefore evaporation is used for lift-off process.

Lift-off of the evaporated Titanium by dissolving the resist in the solvent Remover 1165 is the last step of the process. The success of this step is dependent on material properties such as stress and thickness, width of opening to be dissolved by the solvent and step coverage by metal deposition. For this last step of the lift-off, wafers were left in the solvent for one night at room temperature. To stop the process wafers were immersed into isopropanol tank, and then were rinsed with DI water. Successfully defined gratings on top of pyrex wafers can be seen in Figure 3.8.

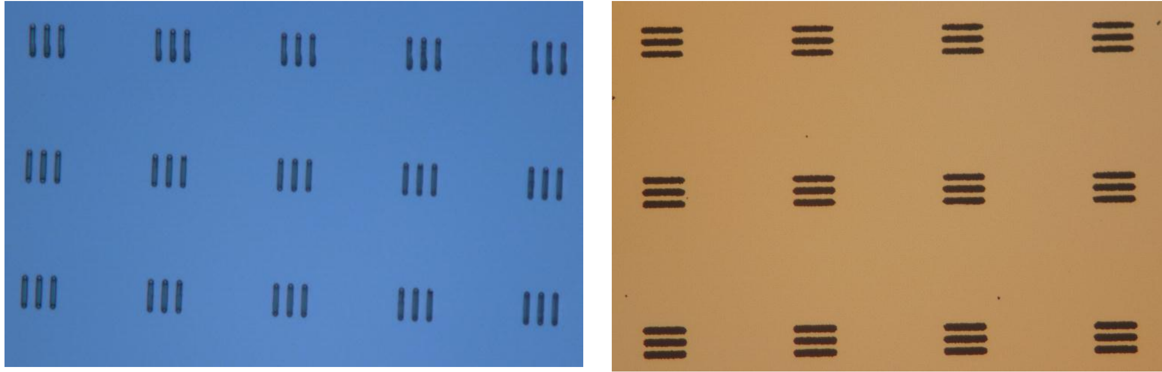

Figure 3.8 Defined gratings with lift-off process.

3.2.1.3 Deposition and Patterning of Sacrificial Layer

Hardbaked photoresist is used as the sacrificial material. That is due to easiness of removing photoresist by resist remover or acetone. 2 µm of the photoresist AZ1512 was spun coated and hardbaked at 100 °C for 5 hours. The purpose of the hardbake is to dissolve all the solvent remaining in the resist, because if not, this solvent causes outgassing during the post bake of the further photolithography step, therefore buckling of the titanium layer was observed.

After the coating of photoresist sacrificial layer, a photolithography step was performed to define the anchors. Resist coated wafers were exposed to UV and after the develop step, anchors were defined. The patterned anchors can be seen in Figure 3.9.

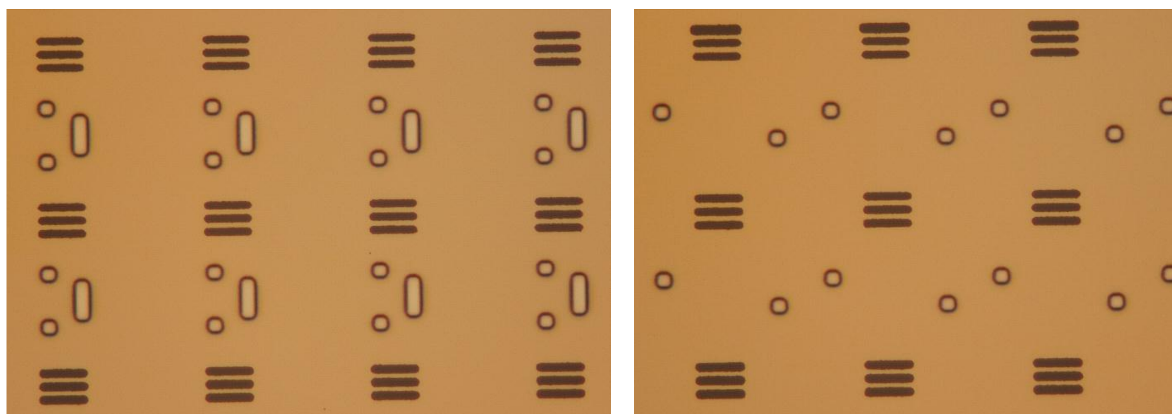

Figure 3.9 Anchor definition on photoresist sacrificial layer.

3.2.1.4 Parylene deposition

After defining the anchors, parylene C is deposited onto wafers as the structural material using Comelec C-30-S parylene deposition system. Before deposition, wafers' backside was protected with a tape layer since both sides of wafers are coated in this equipment. As explained in earlier chapters, at first 200 nm parylene was deposited but due to stress related problems, fabrication process was continued with 400 nm parylene.

3.2.1.5 Ti Layer Deposition and Patterning

Titanium layer thickness was predicted to be 100 nm but 200 nm titanium was deposited since parylene thickness was 400 nm instead of 200 nm. The blanket deposition of Ti was performed with Pfeiffer Spider 600 sputter system. To increase the adhesion with parylene layer, oxygen plasma was performed for 1 minute before the deposition.

After photolithography with 3rd mask, 100nm aluminum was deposited on backside of the wafers because the Reactive Ion Etching (RIE) equipment has an electrostatic clamping system. Backside of the pyrex wafers was needed to be deposited with a metal layer to be

safely clamped inside the chamber of the etcher. And the best candidate for this layer was aluminum due to easiness of removing Al layer without etching Ti layer. Patterning of Ti layer was performed with RIE using STS Multiplex ICP. The patterned metal layer can be seen in Figure 3.10.

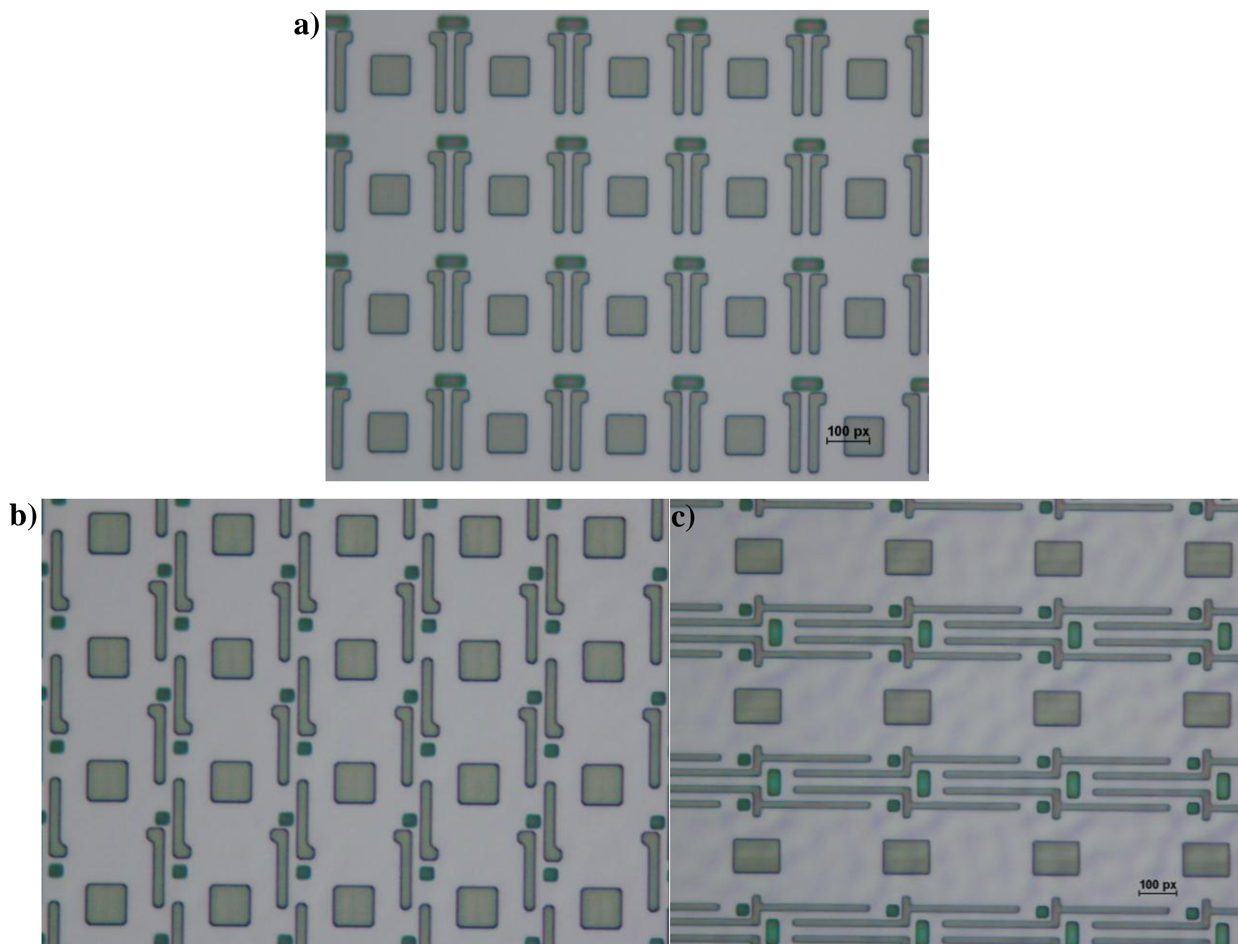

Figure 3.10 Titanium layer patterned for bimaterial legs and reflectors of (a) one-sided design. (b) two-sided design. (c) 4-leg design.

3.2.1.6 Patterning of Structural Layer

STS Multiplex ICP RIE machine was again used to etch the parylene layer to define the isolation legs and absorption pads. The recipe of RIE machine to etch parylene attacks also photoresist with a etch rate of 1:1, but since parylene thickness is 400 nm, 1.1 um of photoresist was sufficient to etch parylene. Different devices can be seen in Figure 3.11.

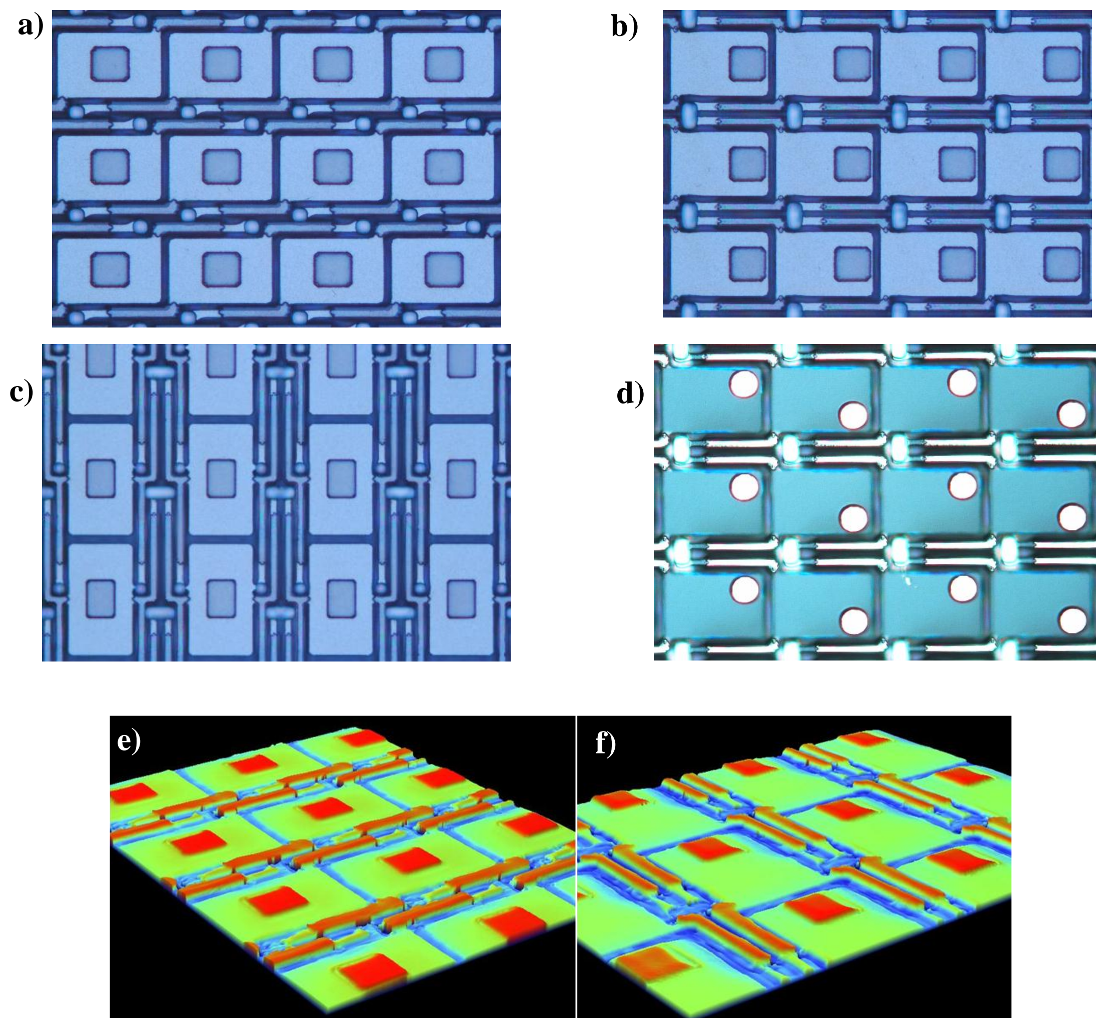

Figure 3.11 (a,b,c,d) The devices on top of sacrificial layer after RIE step. (e,f) optical profiler images of the devices.

3.2.1.7 Dicing

The wafers were taken outside the cleanroom for the dicing step. The wafers were coated with photoresist to protect the structural layer. The dies were designed such that each one is a 13.4 mm x 10.6 mm rectangle. The arrays with 64 x 64 formats were designed such that each one is 5.1 mm x 3.4 mm.

3.2.1.8 Releasing

Releasing of the dies were performed with positive photoresist stripper since all the photoresists used for the last lithography step, sacrificial layer and protecting the structural layer are the same photoresist, AZ1512. Releasing with oxygen plasma could not be performed because oxygen plasma attacks also parylene, which is the structural layer material. In order to release, the dies were left in a beaker full of photoresist stripper, Shipley SVC-14. After one night in beaker, the dies were dipped into distilled water then transferred quickly into ethanol for one hour because it was strictly forbidden to expose the chamber of the supercritical dryer to any acids or any other liquids. During these transfers of the dies, exposure time to air must be minimized for best results. The releasing step was ended with Tousimis Automegasamdri 915-B Critical Point Dryer to avoid stiction, sticking of the released membrane to the substrate, after wet etching of sacrificial photoresist. It is shown that supercritical carbon dioxide can be successfully used to alleviate the stiction problem. The absence of surface tension of in the supercritical phase of liquid CO_2 provides an excellent means to overcome stiction. The stiction problem reduces yield and hence reduces the efficiency of the process. Liquid CO_2 is selected for this process because of its relatively low critical temperature and pressure, high diffusivity and low surface tension. Successfully released devices are shown in Figure 3.12.

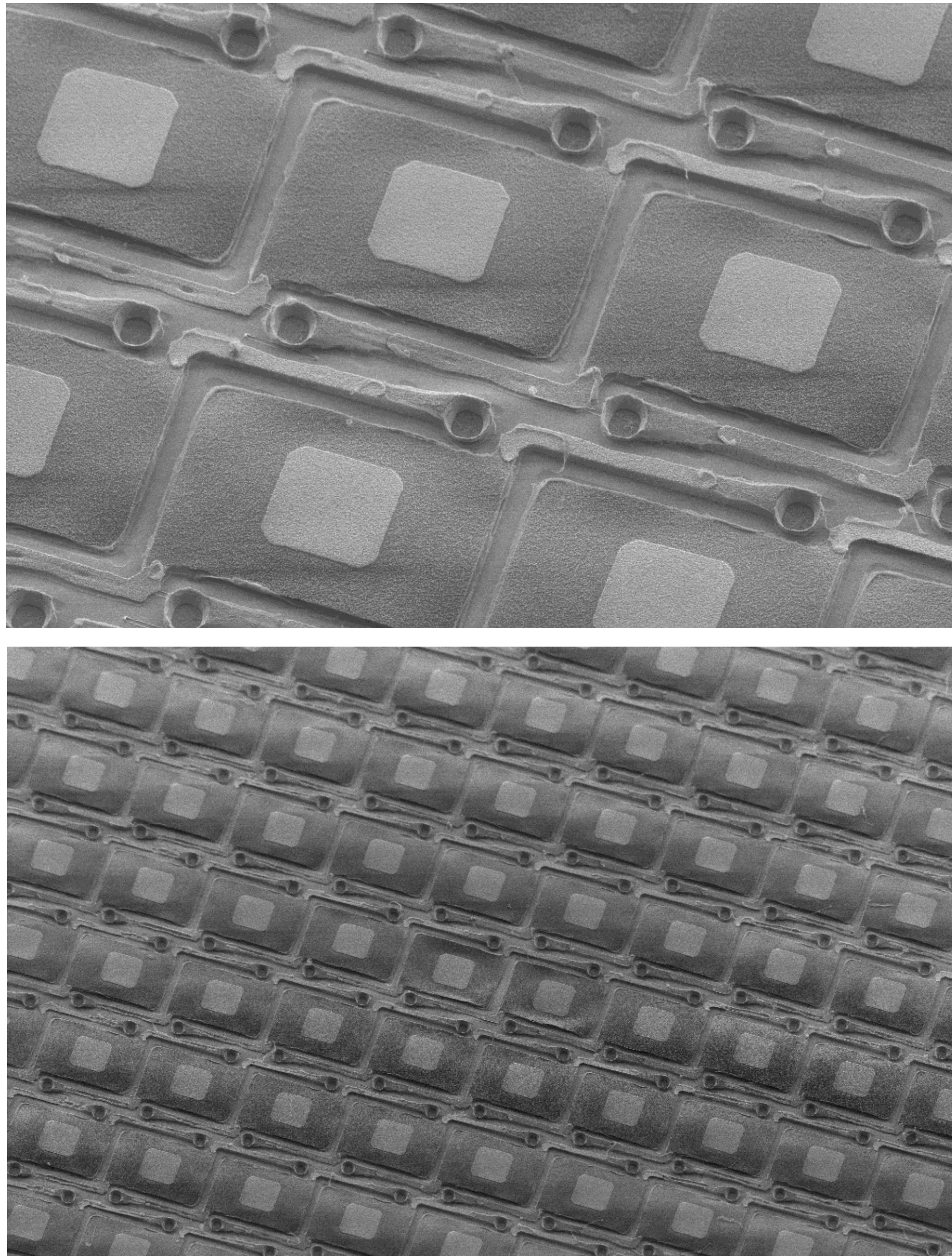

Figure 3.12 Successfully released devices.

3.2.1.9 Thin Film Absorber Deposition

IR radiation can be absorbed by thin or porous metal films. A metal layer starts to reflect when the thickness of the metal increases. But, a thin metal layer is transparent. There exists a critical thickness where high absorption occurs. In order to increase the absorption of the IR sensor, a thin film metal layer was deposited on the dies. To optimize the thickness of the absorption layer, different thickness of Ti was deposited on bare wafers using different sputter and evaporation equipment. Then their sheet resistance was measured with a four-point resistivity meter, KLA Tencor OmniMap RS75, in order to meet matching conditions. It has been shown that thin metal films having sheet resistance, $R_s = \eta_0/2$, where η_0 is the wave impedance of vacuum (377 Ω) where refractive index is 1, absorbs 50% of the incoming radiation. Furthermore, the absorption can be increased up to 100% for a specific wavelength by placing a thin metal with $R_s = \eta_0$ placed in front of a reflector, with λ/4 gap in between. In other words, by matching the absorber film to the wave impedance in vacuum, maximum power absorption is achieved, which is similar to matching load impedance to source impedance in electronic circuits. Resistance measurements of different Ti thicknesses taken with 4-point probe are shown in Figure 3.13. Same thicknesses were also measured after several days to see how the resistance changes (Figure 3.14). After these optimization steps, 10 nm Ti with LAB600 evaporation machine is selected as the absorber thickness since its resistance is the closest to wave impedance of vacuum which is 377 Ω.

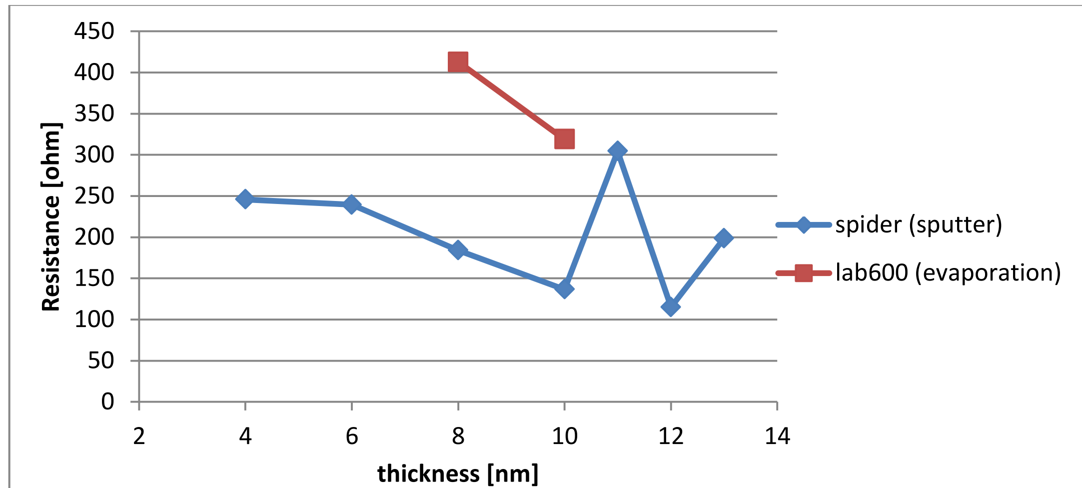

Figure 3.13 Sheet resistance of Ti for different thicknesses for 2 different deposition equipment.

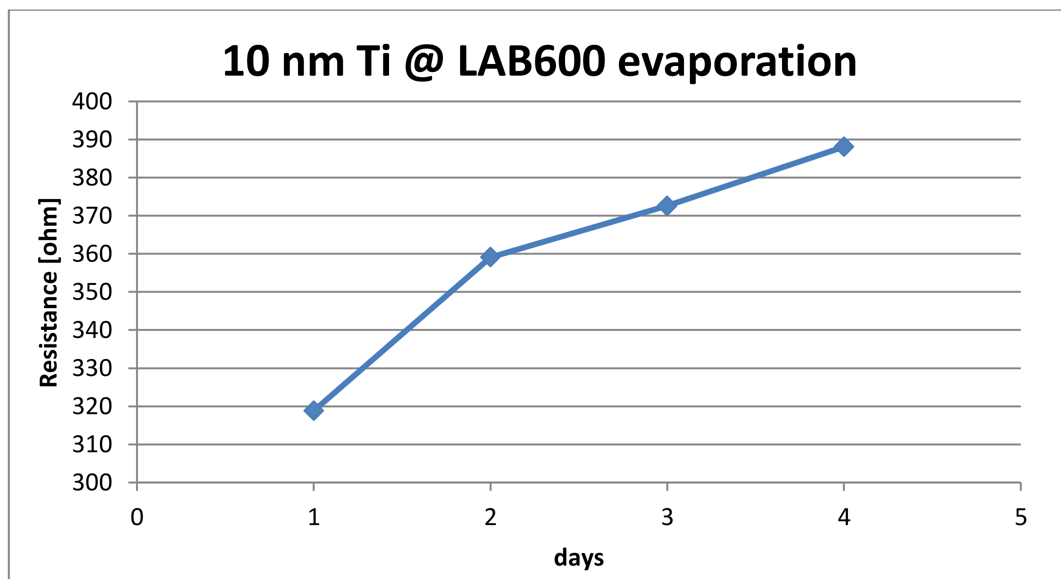

Figure 3.14 Sheet resistance change of 10 nm Ti after 4 days.

3.3 Process Optimizations

- *Organization of process steps:* In the first fabrication run at CMi, the process flow was different than the one in Figure 3.7. In the previous process flow shown in Figure 3.15, titanium layer was deposited after the deposition of parylene as a hard mask for dry etching of the structural layer. This metal layer was patterned with parylene mask and after defining parylene, titanium was patterned with combined reflector and bimaterial mask. In the next process flow, bimaterial legs and reflectors were defined after the parylene deposition. Structural layer of parylene was patterned afterwards. Thus, number of process steps decreased by two.

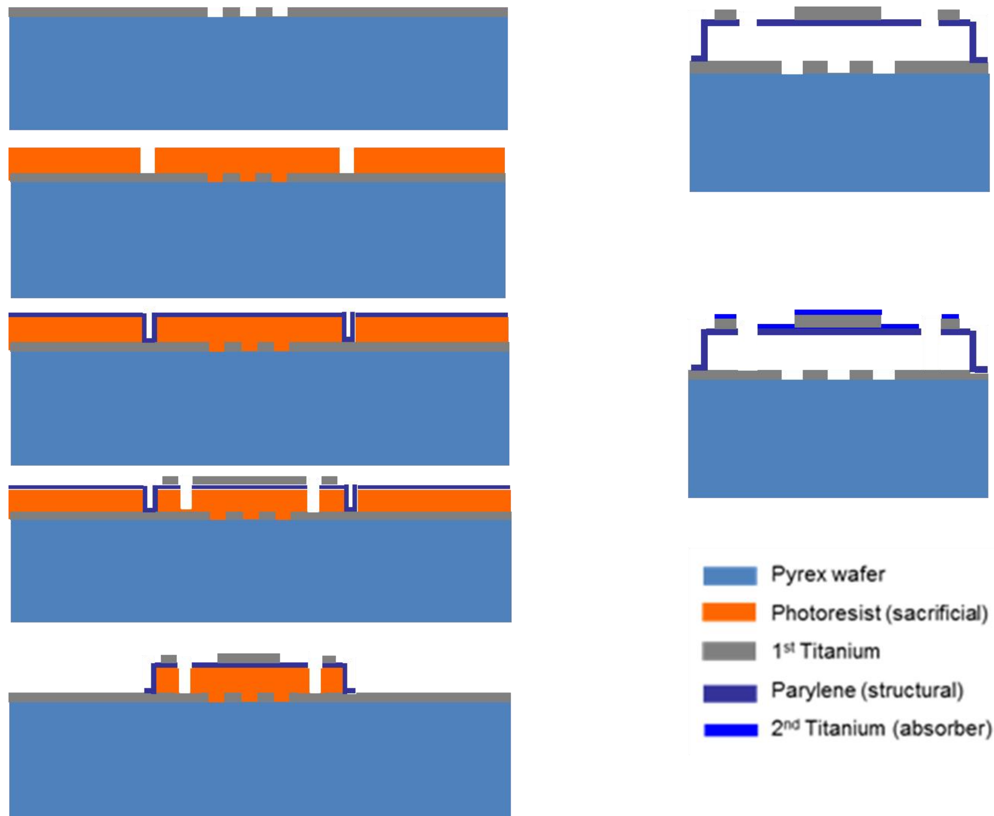

Figure 3.15 Previous process flow.

- *Defining gratings using lift-off instead of wet etch with HF:* Process flow starts with defining of diffraction gratings and this step was performed with wet etching with Hydrofluoric Acid (HF) solution HF(49%):H_2O 1:4 which was present in metal etching wet bench. Moreover, more diluted HF solutions were prepared for controlled wet etch but since HF is a very strong acid, defining very small features like gratings with 2 μm width with HF is anuncontrolled process. This etching step was repeated with HF(49%): H_2O 1:300. Etching was happening in a very short time and as a result, the grating area was completely removed. The best results obtained with wet etch are shown in Figure 3.16 but it can be observed that the grating period is not 50%.

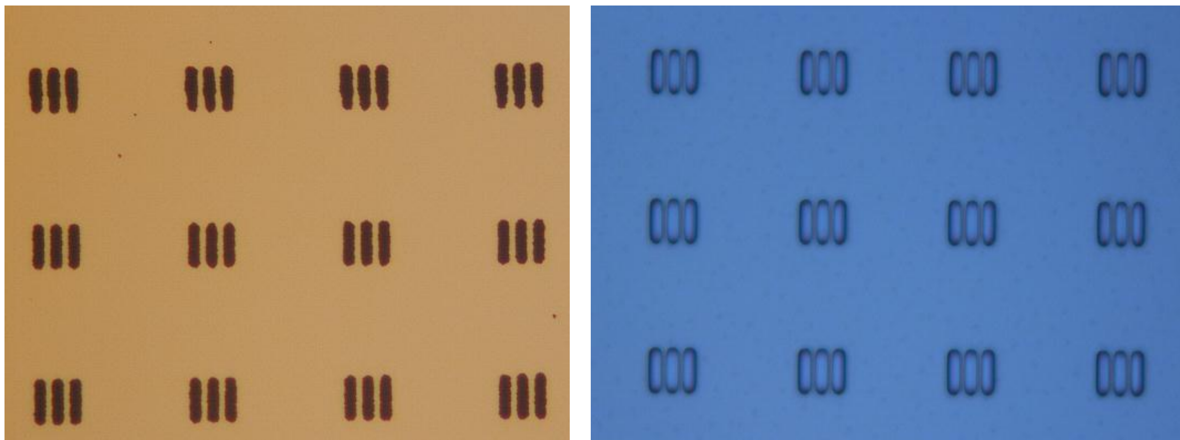

Figure 3.16 Grating definition on top of Pyrex wafer by wet etching techniques.

- *Titanium deposition on parylene in 2 steps:* After the deposition of 200 nm titanium on top of parylene, cracking and buckling of the both titanium and parylene layers were observed due to high mismatch (Figure 3.17). The problem was avoided by depositing titanium in two steps, 100 nm during each.

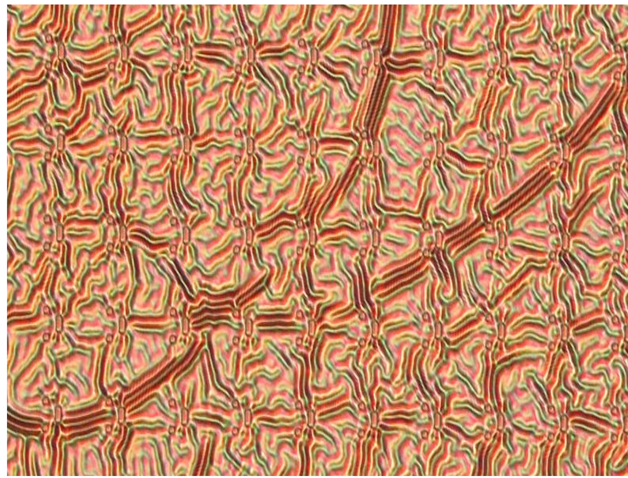

Figure 3.17 cracking and buckling after deposition of blanket titanium on parylene.

- *Photolithography parameters:* During the photolithography steps of the first fabrication run, thickness of the photoresist was 1.6 μm and hard contact mode of the mask aligner was being used. The photolithography quality was low with these parameters. The edges of the features were not sharp and the bimaterial legs were not perfectly defined, they were attached to the anchors of adjacent pixel, which prevents the movement of the device (Figure 3.18). Sharp edges and perfect patterning was obtained after changing these parameters as 1.1 μm photoresist thickness, less exposure time and vacuum contact mode of the mask aligner.

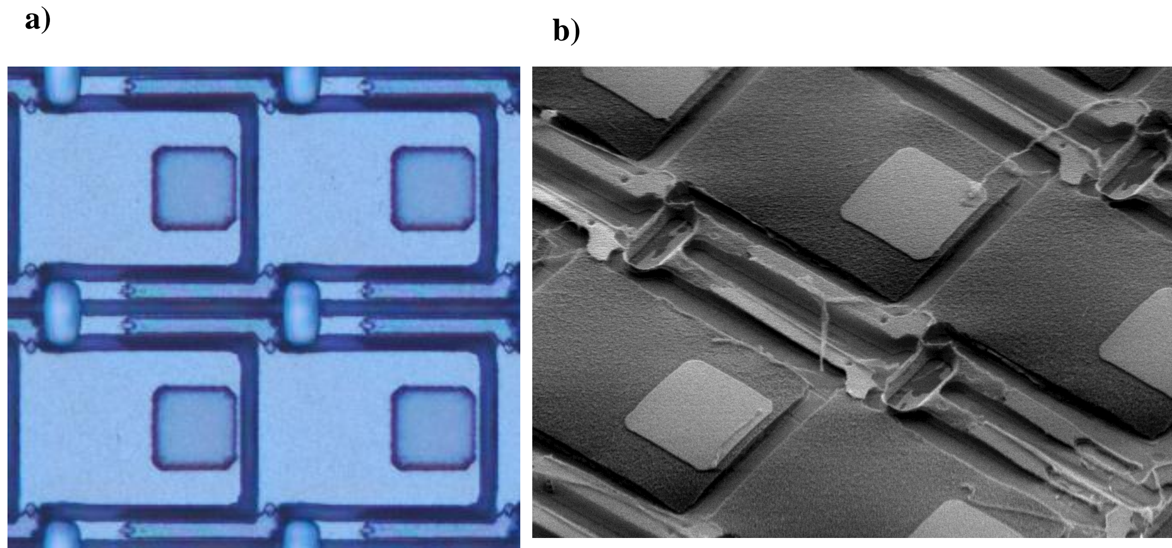

Figure 3.18 (a) Photolithography errors in the edges of bimaterial legs. (b) Not well-defined legs connected to adjacent pixel's anchor.

- *Absorber deposition after release:* In the first process flow, absorber deposition was before the releasing step. Although it was evaporated, thin metal layer covered the walls of the resist because of thermal softening. During evaporation or any other dry etching process, the photoresist film may be heated above its softening point. Therefore, the resist profile starts rounding allowing the coating material to cover also the resist profile sidewalls. As a consequence, the majority of the resist remained above the reflector and bimaterial legs, which drastically limits the movement of the device, after releasing with Shipley AZ100 remover at 40 °C. The resist was removed at higher remover temperatures (~80 °C); however, extensive buckling is observed on the membranes (Figure 3.19). The problem was avoided by deposition of absorber layer after the releasing step.

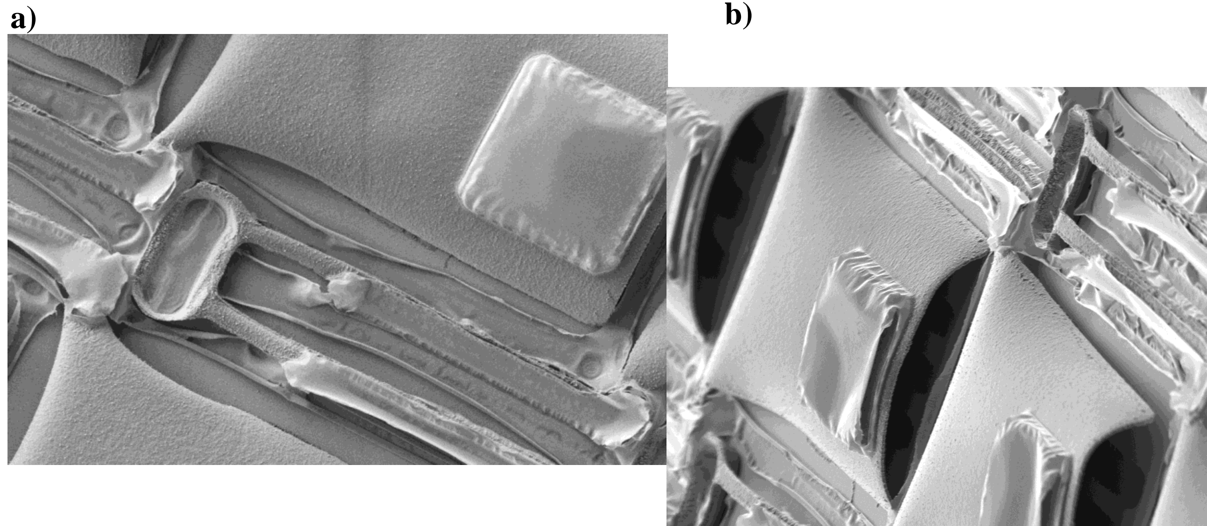

Figure 3.19 (a) Unremoved photoresist on bimaterial legs and the reflector. (b) buckling of sensor membranes after photoresist removal at 80 °C.

3.4 CMOS ROIC Post-Processing

A post-processing of fabricated CMOS chips was needed in order to integrate with IR sensors. Holes on CMOS chip were needed to be etched in order to let the readout laser beam passes through and reflects from the reflector of the IR sensor. First of all, the holes on the readout chip were ordered from the foundary with the readymade holes on it. The diameter of the holes was specified as 10 μm which is compatible with reflector and diffraction grating size of the IR sensor and the thickness of the IC chip is 280 μm. The process flow of the post-processing is explained below.

3.4.1 Grinding

First step of post-processing is grinding because thickness of the IC chip is 280 μm and an aspect ratio of 1:28 was needed to etch the holes but the safe aspect ratio of the Deep

Reactive Ion Etching (DRIE) equipment was 1:10 at CMi. Thus, firstly the chips were thinned down to 100 μm with automatic surface grinder DAG810. CMOS chips were firstly mounted to dedicated frames to ensure perfect handling using Powatec Wafer Mounter P-200. These frames are used in combination with a UV sensitive tape to handle chips. After grinding, the Automatic Cleaner DCS1440 gives clean and dry work pieces that are then safely released when exposing the tape to UV light (Powatec UV Curing U-200).

3.4.2 Chip Handling

The grinded chips were placed on a silicon test wafer for further process steps. Before that, 200 nm aluminum was deposited with Balzers BAS 450 sputter system as an etch stop for silicon etching step. Then chips were fixed onto wafer with PhotoPro33 Dry Film Laminator. Ordyl Alpha 940 dry film is a negative tone photoresist of 40 μm thickness. Chips are fixed onto wafer and also coated with photoresist with this technique. 40 μm of photoresist is thick enough for further etching steps. After the lamination, a photolithography step was performed for patterning the dry film to protect the circuit part of the chips and to remove the dry film on the holes. The aluminum pads for the electrical connections were also covered with capton tape to protect them from etching steps. Chips placed on the handling wafer are shown in Figure 3.20.

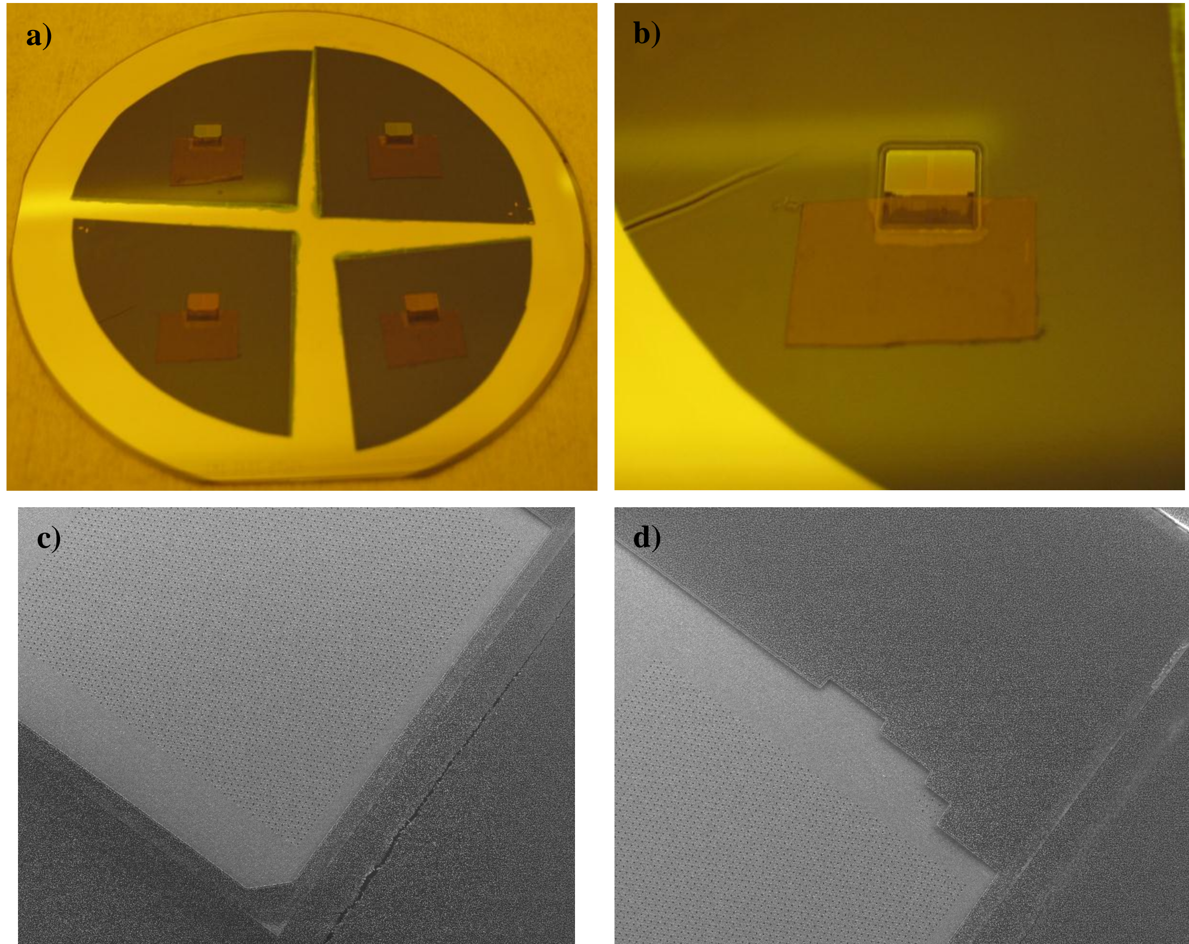

Figure 3.20 (a,b) Thinned CMOS chips placed on the holder wafer with dry film and capton tape. (c,d) SEM images of patterned dry film.

3.4.3 Etching Holes

Holes are implemented on the IC chip to allow the readout laser to reach the IR sensor array by passing through these holes. It is desired to implement the holes with accuracy higher than 1-2 µm. Thus, it is decided to use the top metal mask as a mask layer on top of

all the electronics and apply RIE to etch the oxide, nitride and silicon layers. One problem related with the top metal mask layer was, due to thermal expansion reasons it was not possible to manufacture a large metal block. Thus, design rules implied to put slots with 20 μm distance in between. Mask layout and corresponding SEM pictures of the metal mask are shown in Figure 3.21.

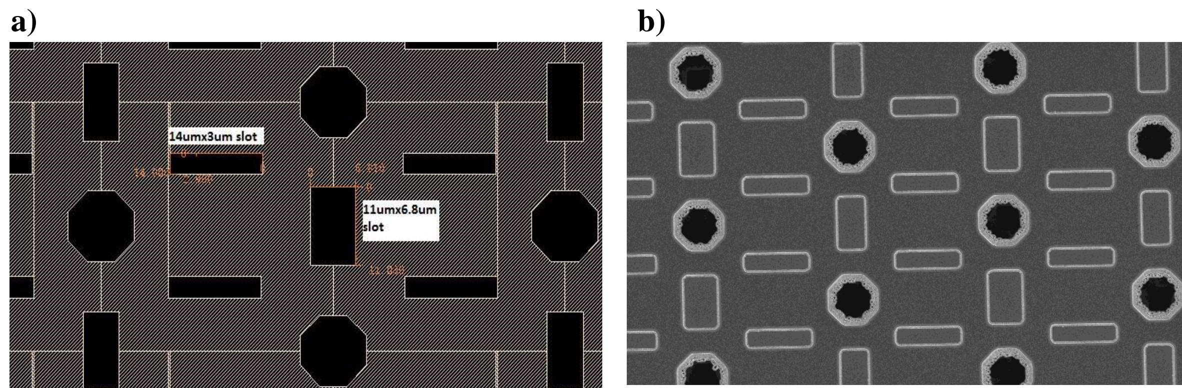

Figure 3.21 (a) Top metal mask layout for hole etching. (b) SEM images of etched holes.

Etching time of nitride, oxide and silicon were calculated according to the layer thicknesses. After 70 minutes of RIE in Alcatel 601E dry etcher, holes were perfectly etched. Figure 3.22 illustrates SEM pictures of the holes taken from both backside and topside.

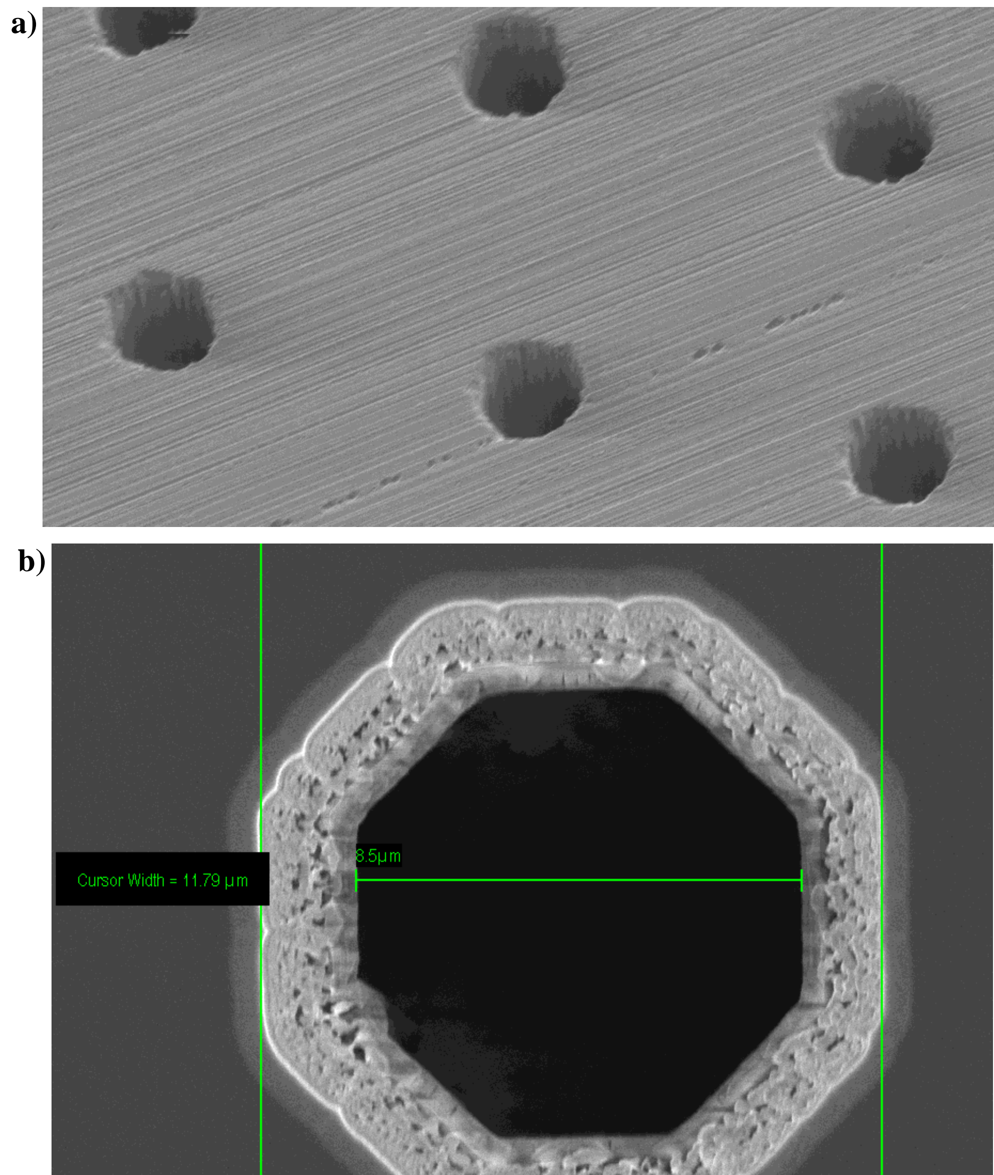

Figure 3.22 (a) SEM images of CMOS chip from backside. (b) SEM image of a hole.

3.4.4 Releasing

First step of the releasing is removal of the aluminum mask layer. Etching of the top metal mask was performed using STS Multiplex ICP RIE machine for 4 minutes. Figure 3.23 illustrates microscope images of the CMOS chips after Al removal.

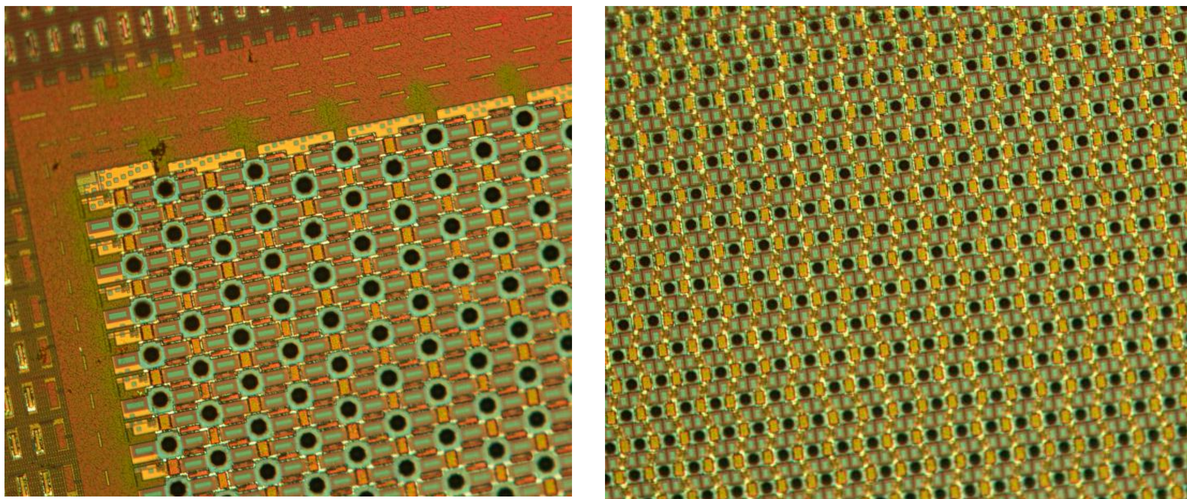

Figure 3.23 Microscope images of CMOS chip after Al removal.

The capton tape was removed and the dry film stripped using alkaline NaOH 2.5% solution in order to completely release the chips. Positive photoresist stripper and oxygen plasma were also applied to chips since dry film stripper attacks also aluminum pads. After full release, an optical microscope with back light illumination was used to inspect the etched holes from backside Figure 3.24.

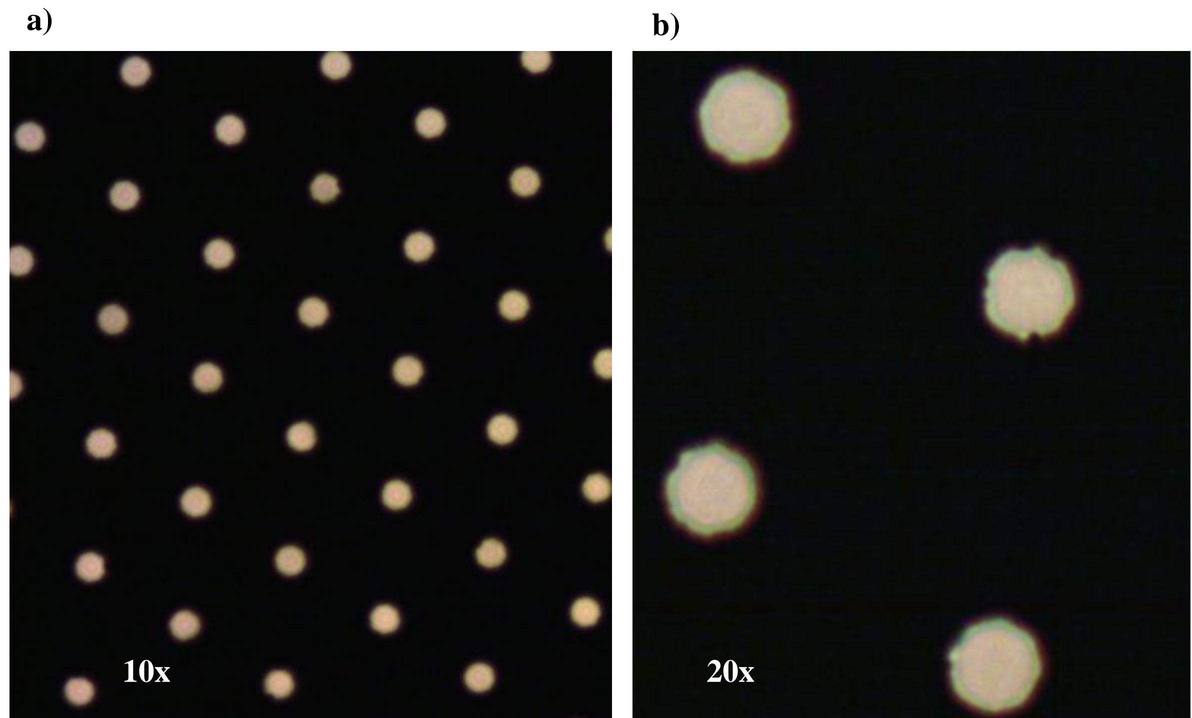

Figure 3.24 Microscope images with backside illumination using (a) 10x objective. (b) 20x objective.

4 TEST AND CHARACTERIZATION RESULTS

In this chapter, the experimental results for the thermo-mechanical detector arrays and CMOS readout integrated circuits (ROIC) are discussed. Then, integration of MEMS sensors with CMOS chips is explained. For the characterization of MEMS sensors, direct heating and IR imaging experiments are performed. Post-processed CMOS chips are tested with modulated laser and alignment of MEMS sensors with CMOS chips is discussed.

4.1 Thermal and Mechanical Tests

Even though, the author of this thesis was not involved in the characterization effort, the experimental setup and test results are briefly explained to maintain the unity. All the thermal and mechanical tests of the thermo-mechanical IR sensors are performed by Ulaş Adiyan, PhD student in our group. First experiments are performed in SEM with direct heating to prove that devices are released and respond to temperature differences. For that purpose, detectors that are fabricated with parylene and titanium are heated with a peltier stage in the SEM chamber to 50ºC. In Figure 4.1, lower left corner of the membrane is lifted up due to temperature increase but it is difficult to quantify this deflection with the actual magnification. However, these pictures indicate that released pixels deflect with changing temperature.

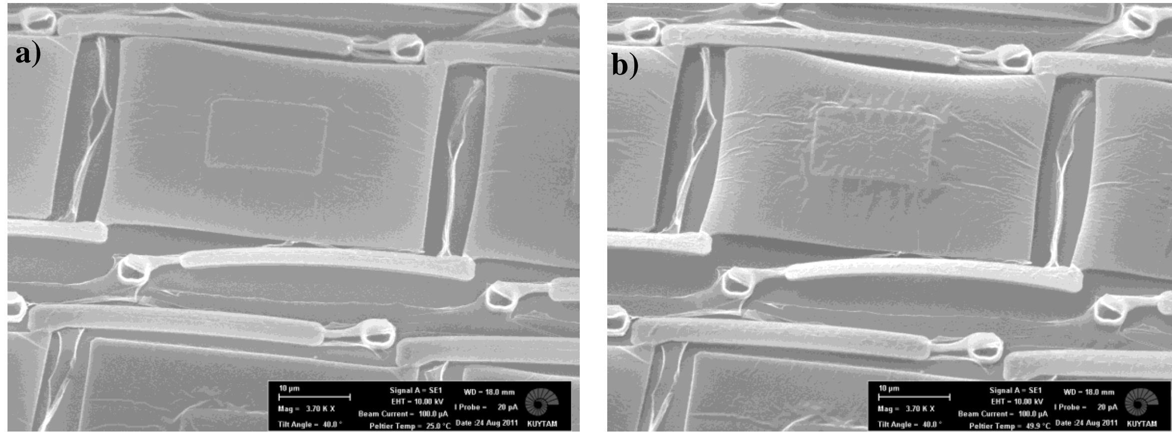

Figure 4.1 Direct heating in SEM chamber. (a) Image at 25 ºC. (b) Image at 50 ºC.

4.1.1 Direct Heating Experiments

Figure 4.2 illustrates the experimental setup that is used for measuring sensor performance using direct heating. The sensor array is located on a thermoelectric cooler (TEC). The optics readout section is composed of a laser source that illuminates the sensor array. The 1st diffracted order light is imaged onto a CCD camera using a beam splitter and a lens.

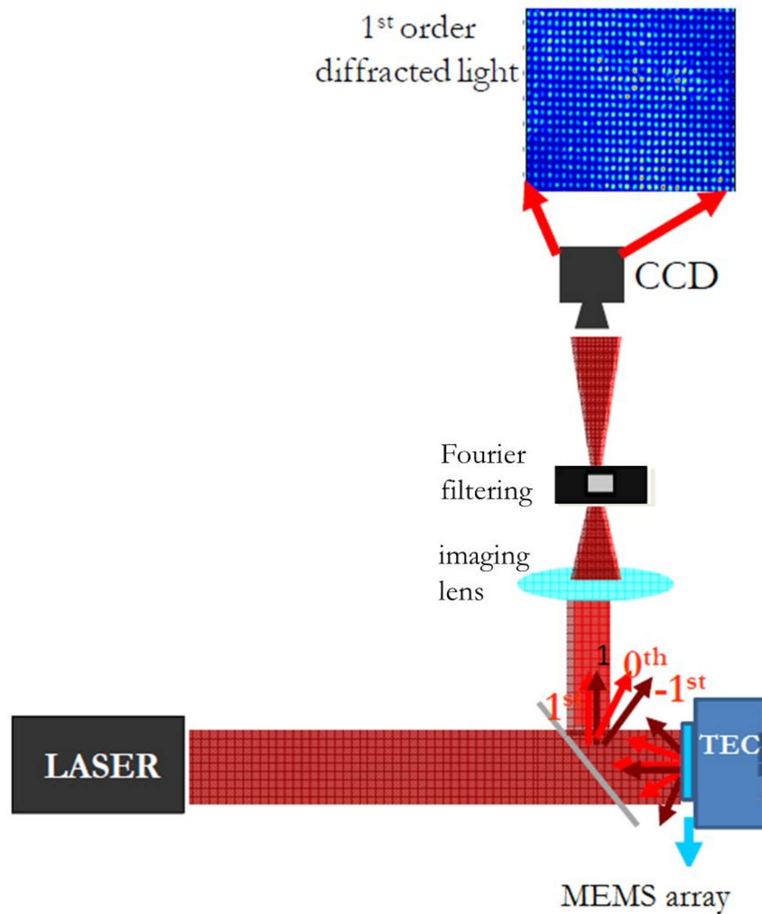

Figure 4.2 Illustration of the experimental setup for direct heating.

Using the experimental setup, a parylene/Ti sensor array was heated using a TEC from 20 ºC to 40 ºC and the change in 1st order intensities was recorded with the CCD camera. The CCD image of the heated array and the arbitrarily chosen sensor are shown in Figure 4.3 (a). Figure 4.3 (b) illustrates the 1st order diffracted intensity of the chosen sensor with respect to video frame. The intensity starts to change once heating starts, and settles down to certain intensity value when the thermal equilibrium is reached. Based on this behavior,

about quarter cycle of the intensity vs. gap curve is covered, which corresponds to a few nanometers of deflection per degree change on the sensor. This value is below the deflections simulated with ANSYS. This difference is caused by the stress problems of the fabrication process and the fact that the temperature increase on the array is less than the temperature reached by the TEC because of sample placement method and the isolation between the array and the TEC surface.

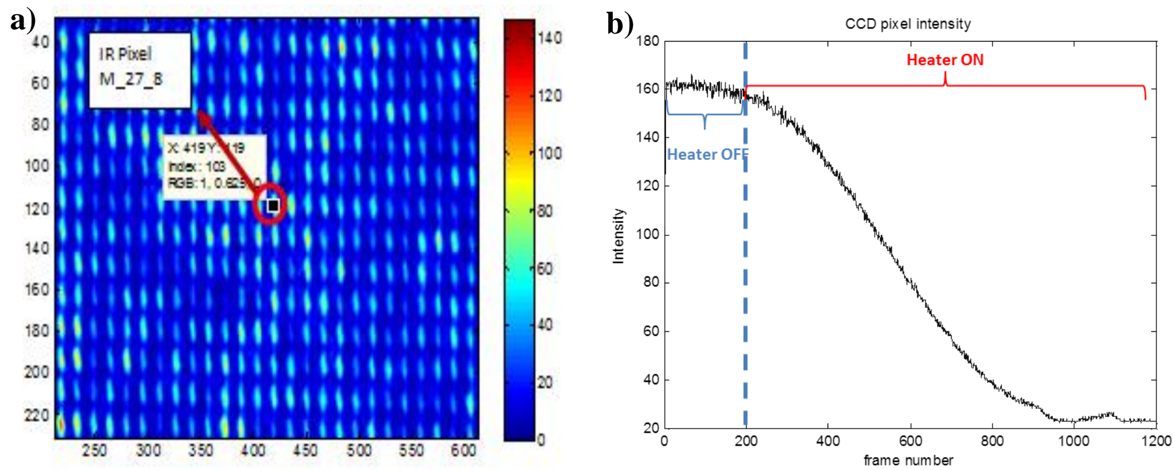

Figure 4.3 Direct heating experiment of parylene/Ti array. (a) CCD image of 1st diffracted orders and randomly chosen pixel. (b) Intensity change of the heated pixel.

Same direct heating experiments were also performed using Si_xN_y/Al sensor arrays. These arrays contain also a sensor design that does not require active thermal stabilization. Direct heating experiments help to prove the working principle of this design. As mentioned before, the design which does not require thermal stabilization does not respond to ambient temperature changes, in other words, sensors of this design should not respond

to direct heating experiments. Figure 4.4 shows a comparison of performance of two designs including the one that does not require thermal stabilization.

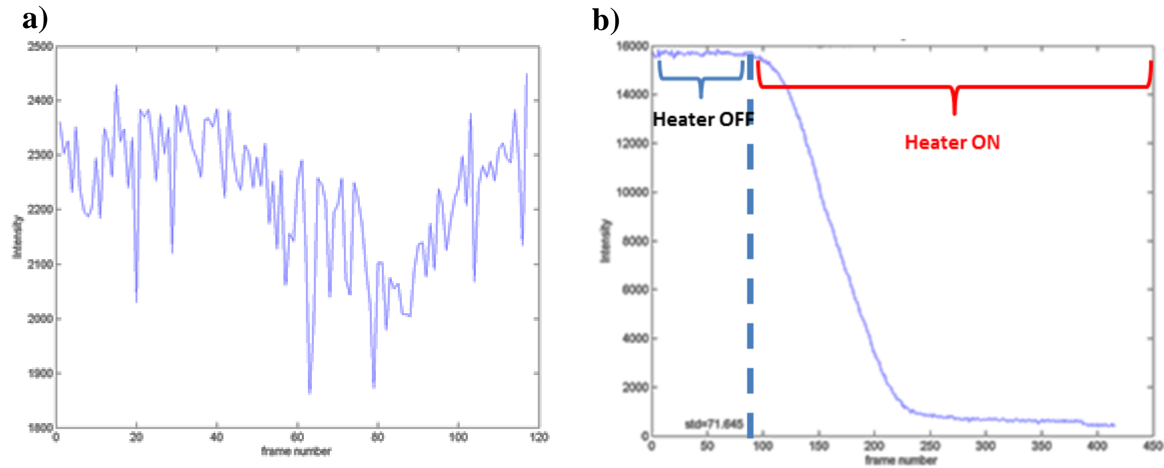

Figure 4.4 Direct heating experiment of Si_xN_y/Al array. (a) Intensity change of the self-levelling pixel. (b) Intensity change of lever design pixel.

Figure 4.4 (a) shows the intensity change of the randomly chosen pixel which has the design that does not require thermal stabilization and (b) shows the direct heating experiment results of the lever design. In (a), according to CCD levels, the intensity variation is composed of noise, therefore in (b), intensity starts to change once heating starts and settles down to certain intensity value once the thermal equilibrium is reached. These two results prove that the design which does not require active thermal stabilization is behaving properly.

4.1.2 IR Imaging Experiments

Figure 4.5 illustrates the experimental setup that is used for IR imaging and measuring NETD.

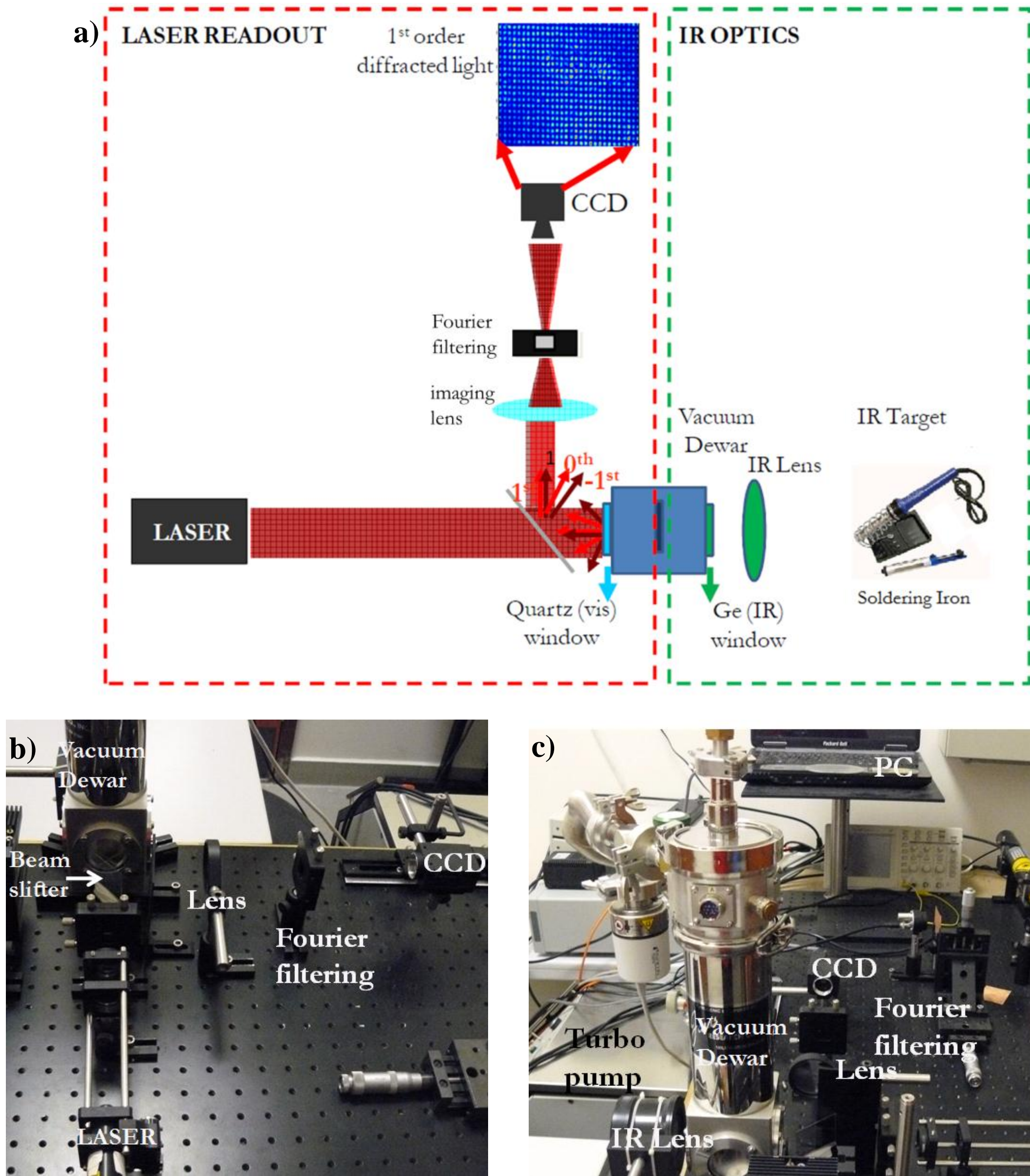

Figure 4.5 (a) Illustration of the experimental setup for infrared imaging experiments. (b,c) Pictures of the setup.

The readout part of the experimental setup is same with the direct heating setup therefore, sensor array is located in a vacuum dewar with a visible window made of quartz and an IR window made of germanium. The dewar is connected to a turbo pump and the experiments are performed at low vacuum values around 1mTorr in order to eliminate heat transfer via conduction and convection. The IR optics part of the setup contains an IR lens in front of germanium window for imaging the IR target onto sensor array.

IR imaging experiments was performed using both Si_xN_y/Al and parylene/Ti based detector arrays. 2 frames of a captured video of a moving soldering iron are shown in Figure 4.6 using a Si_xN_y/Al based sensor array. The sensitivity of the detector array is low since only a very hot object like soldering iron can be imaged, where the temperature contrast is high.

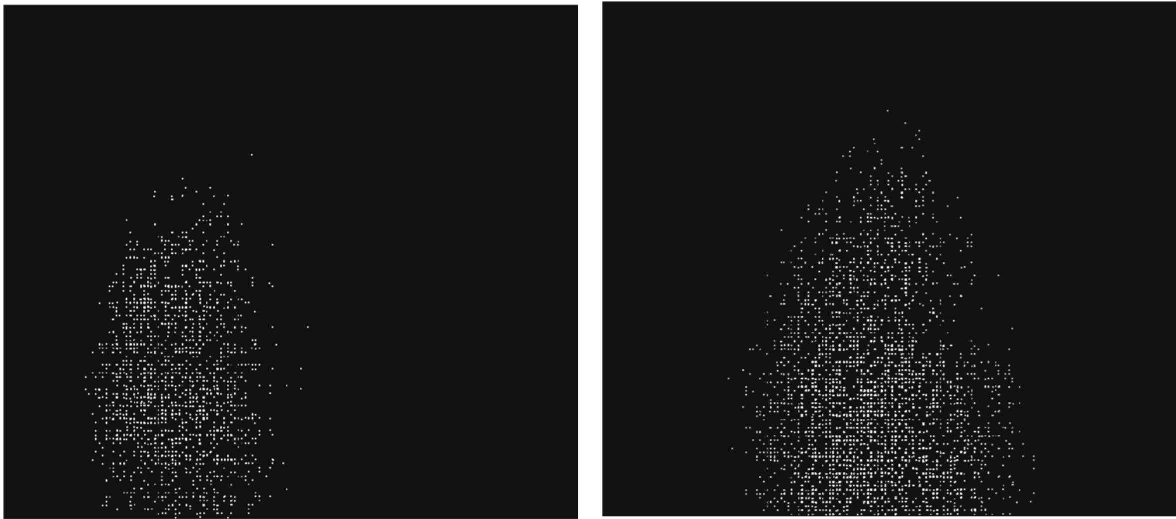

Figure 4.6 2 frames of a captured IR video of a moving soldering iron.

4.2 CMOS ROIC Characterization

For the characterization of the CMOS chips, a PCB is designed and fabricated, and then the chips are wirebonded to them at Lausanne. The designed PCB is shown in Figure 4.7 (a). Some chips are wirebonded without post-process, only the aluminum mask layer was etched for testing the photodiodes (Figure 4.7 (b)). Post-processed chips are also wirebonded to PCB but these PCBs have a hole under the array part of the CMOS chip in order to let the readout beam reach the holes from backside (Figure 4.7 (c,d)).

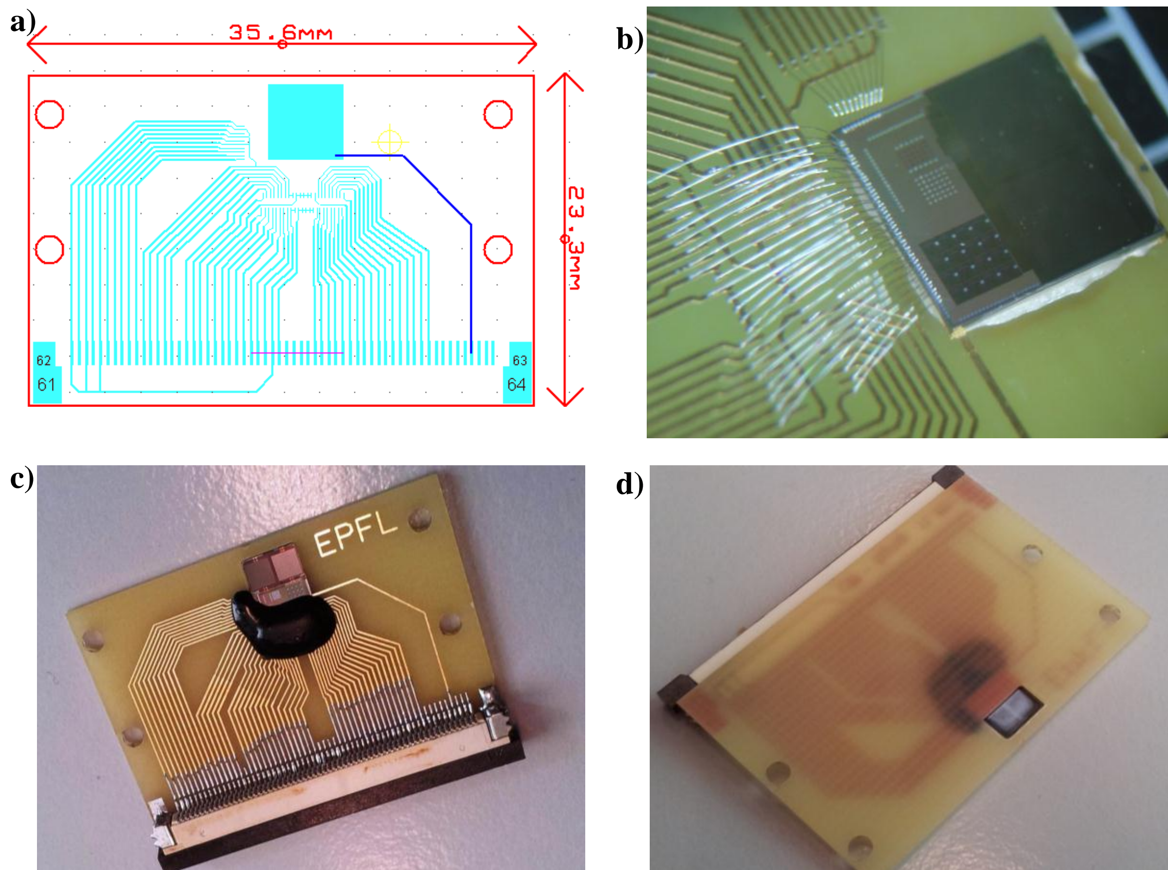

Figure 4.7 (a) Designed PCB for wirebonding. (b) Image of wirebonded test chip. (c,d) Wirebonded post-processed chip to PCB with hole.

For testing the wirebonded chips, a circuit providing the required input voltage and selecting the desired row and column is designed and a corresponding PCB layout is fabricated by Selim Ölçer. Images of circuit layouts and fabricated PCBs are given in Figure 4.8.

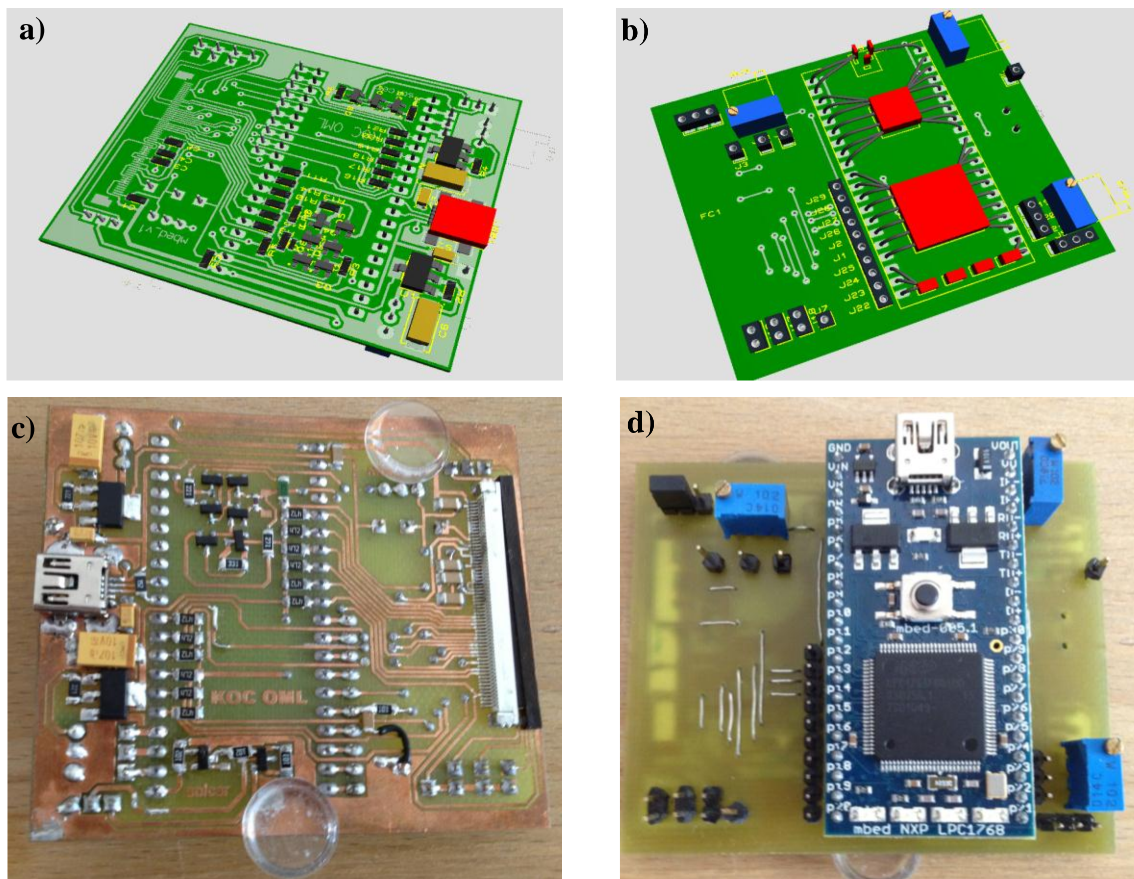

Figure 4.8 (a) Top view of the layout. (b) Bottom view of the layout. (c) Top view of the PCB. (d) Bottom view of the PCB.

A graphical user interface is also designed for the testing of readout circuit by Selim Ölçer. With this interface, the desired photodetector can be selected, duty cycle of the laser can be modulated and the output voltages for different duty cycle ratios can be read and saved to an Excel file. The image of the interface is given in Figure 4.9. In this software, the buttons serve as:

- Port & Connect: Connects chip to computer via USB port.
- Row & Column: Selects the desired photodetector.
- PWM & PWM Sweep: Modulates the duty cycle of the laser and perform a duty cycle sweep with 0.1% increment for the selected photodetector.
- Read all: Scans all the photodetectors and saves the output voltages to an Excel file.
- Average: Selects number of values to measure for averaging.
- Text: Displays alerts if there is an error during the measurements.

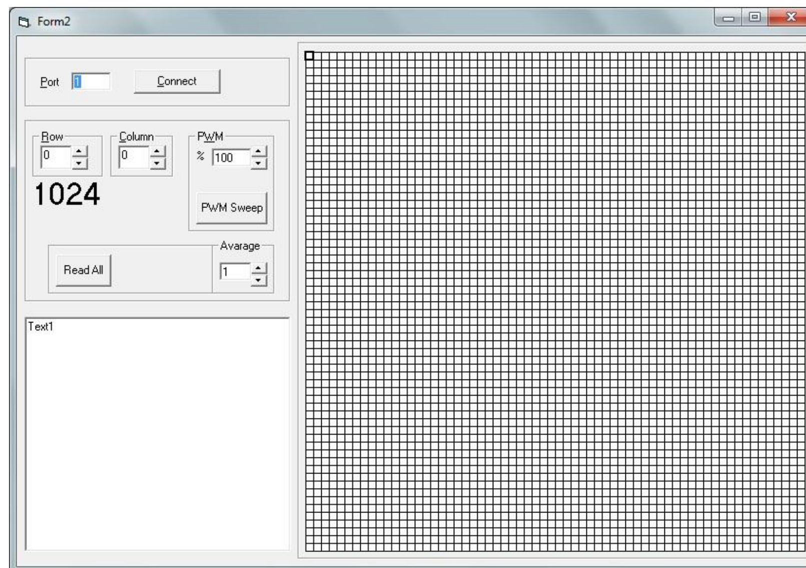

Figure 4.9 Graphical user interface for testing

First tests are performed with a rotating chopper at 2 Hz to monitor PD response. Figure 4.10 shows the first characterization results of test chips. In Figure 4.10 (a), the output of a chip with metal mask on top of the photodetectors is shown. Since the detectors are covered with top metal mask, there is no modulation at the output voltage. But a 220 mV output voltage swing is obtained with the chip without the metal mask when the laser was being modulating at 2 Hz (Figure 4.10 (b)).

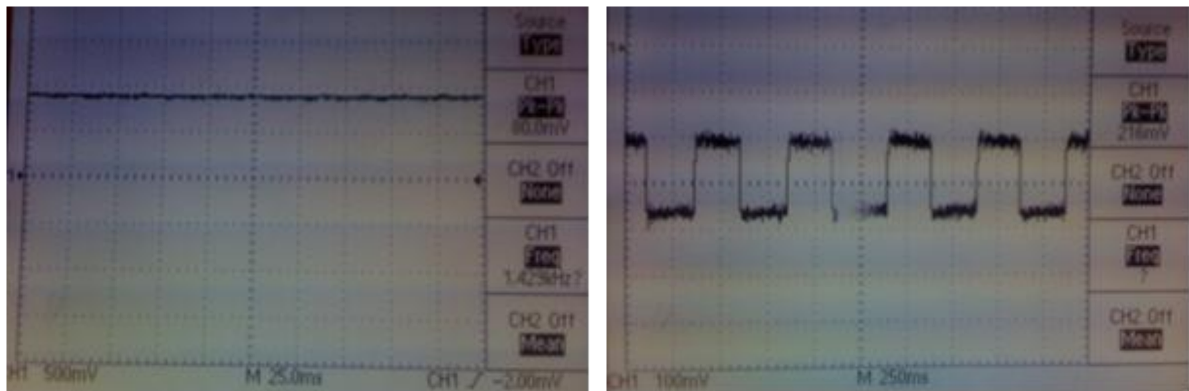

Figure 4.10 Preliminary results of ROIC chip. (a) Output voltage is stable for the chip that is covered with metal mask. (b) Output voltage swing is obtained for the chip with photodetectors not covered with metal mask.

For detailed characterization, a calculation is performed to find how much laser power falls on one photodetector in order to find the sensitivity in terms of A/W. To find out, a CCD is illuminated with a laser and the ratio between the photodetector area and laser spot area is calculated. Laser spot is imaged with a CCD and processed with MATLAB (Figure 4.11).

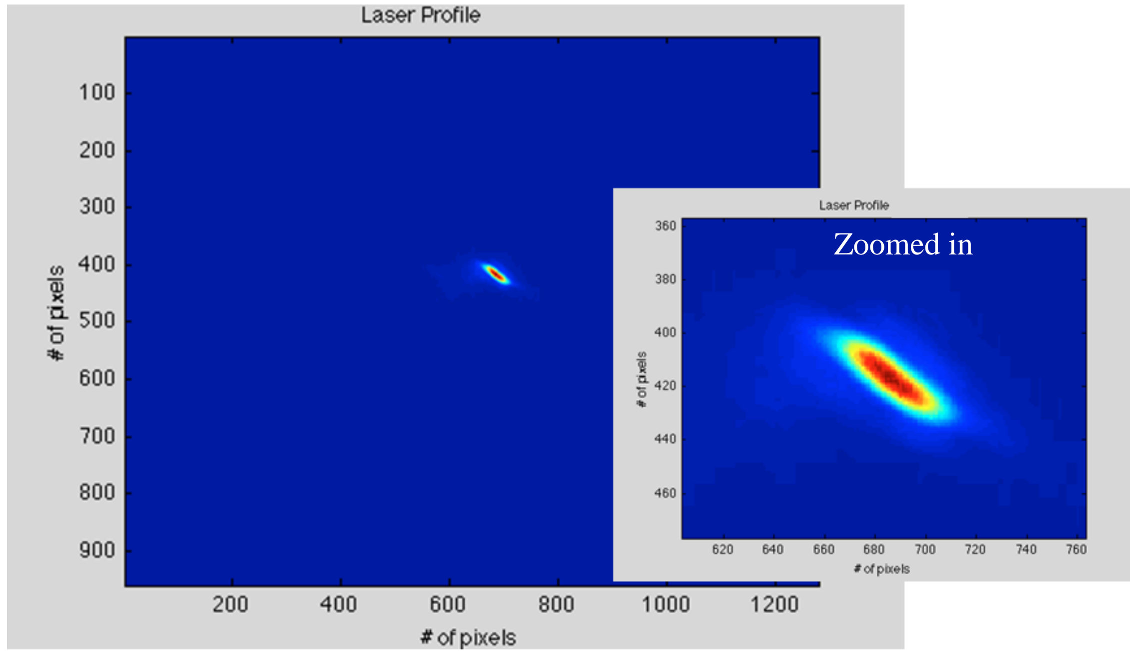

Figure 4.11 Image of the laser spot and zoomed version of it using MATLAB

A cross-section is taken with the highest intensity and a Gaussian function is fit to this section. Therefore, the area with the maximum laser power is calculated. This value is compared with one photodetector area and the laser power ratio for one photodetector is found. The same laser profile is also imaged with the graphical user interface to compare with CCD image (Figure 4.12).

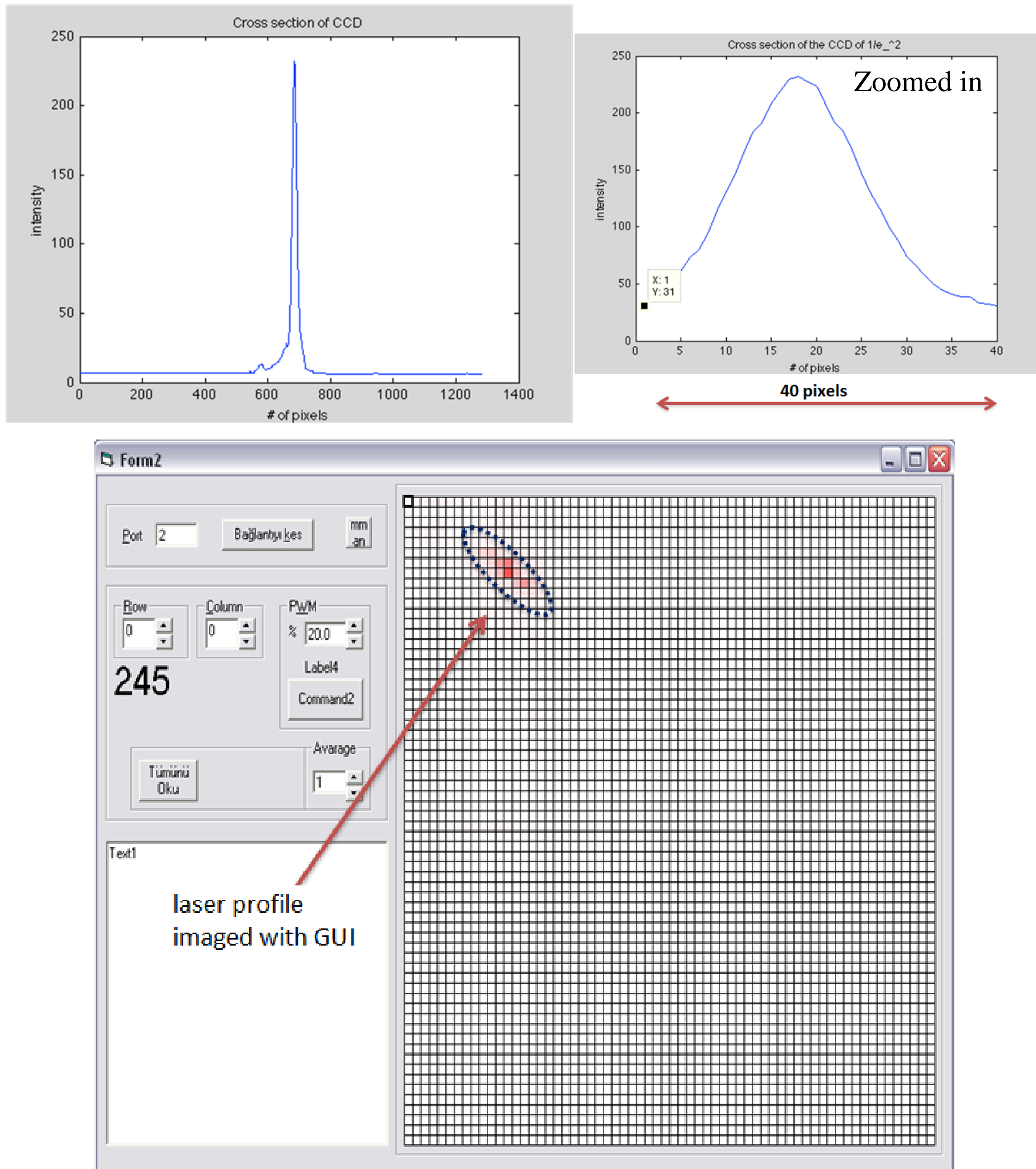

Figure 4.12 (a) Laser profile with highest intensity taken with MATLAB. (b) Laser spot imaged with GUI.

After calculating the laser power on one photodetector, tests for selectivity calculations are performed. The experimental setup is shown in Figure 4.13. In this setup, apart from the laser and CMOS ROIC, there is a Neutral Density (ND) filter to avoid saturation and the fabricated PCB for electronics.

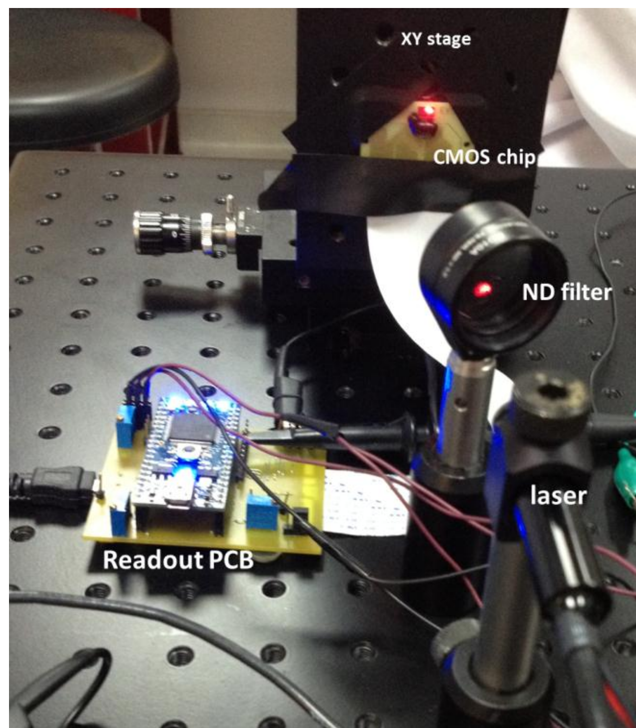

Figure 4.13 Experimental setup for CMOS ROIC characterization

Responsivity for a photodetector fabricated on silicon substrate is given by Eq. (4-1):

$$Responsivity\left[\frac{A}{W}\right]=\frac{V}{2.R}\frac{1}{G}\frac{1}{\alpha.W} \tag{4-1}$$

where V is output voltage, 2 is for sum of two photodiodes, R is amplifier resistance, G is amplifier's gain, α is power ratio and W is the total incident laser power. For the responsivity calculation, CMOS chip is illuminated with a red laser at 1.5 kHz and output voltage is measured while modulating the duty cycle of the laser. The graph in Figure 4.14 shows single photodetector's current with respect to incidence laser power. The duty cycle is changed with 10% increments and single photodetector's current is calculated using Eq. (4-1). The known value of responsivity of silicon photodetectors for red laser in the literature is around 0.3-0.4 A/W. The responsivity value calculated using the measurements in Figure 4.14 is 0.195 A/W.

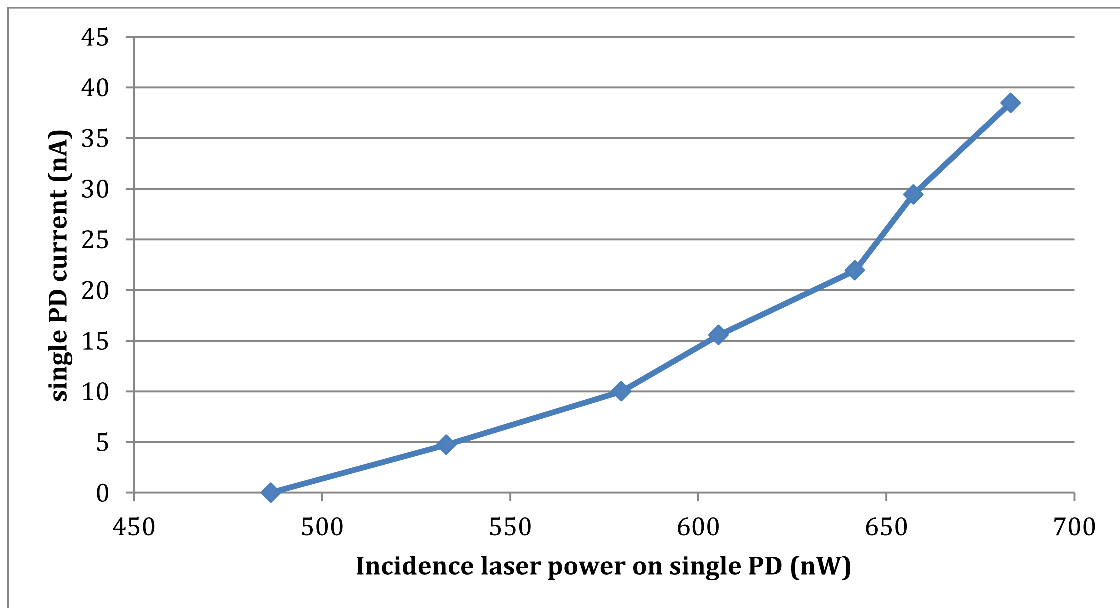

Figure 4.14 The graph of incidence laser power on single PD vs. single PD current.

For the linearity and saturation tests, an experiment is performed with a red laser at 1.5 kHz during which the duty cycle is modulated from 0.1% to 99.9% changed with 0.1% increment. Every measurement in the data set is average of 8 data points and the experiment is repeated for 2 different photodetectors (Figure 4.15).

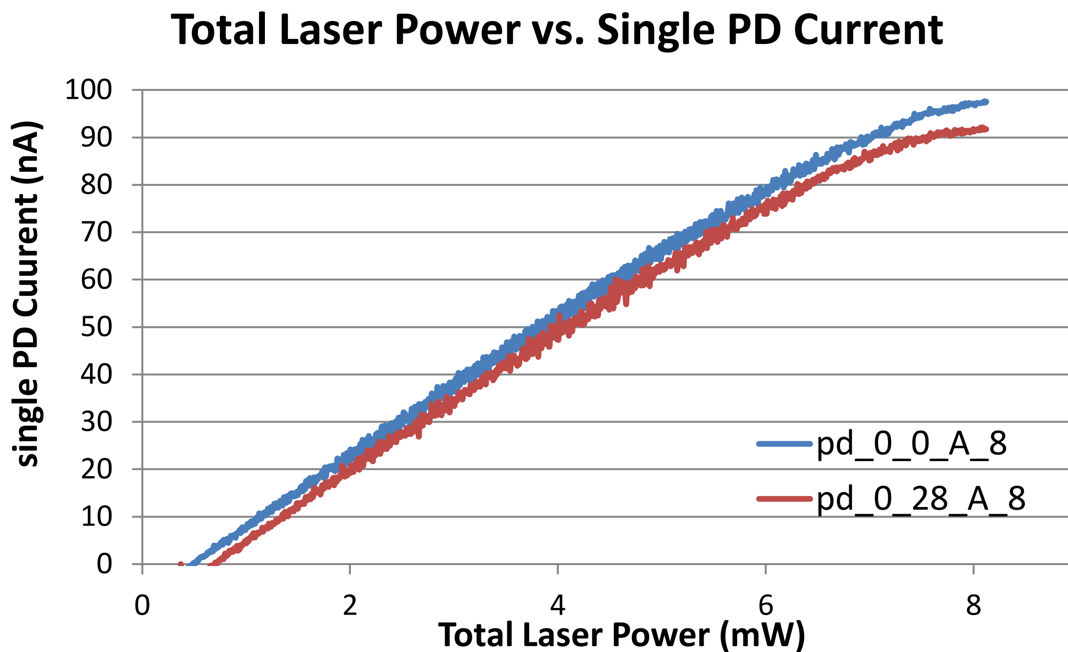

Figure 4.15 Test results of CMOS ROIC for linearity and saturation

According to previous test results, the linearity of the detectors is in the acceptable range and the results of two photodetectors are very similar to each other. Moreover, an optimization for noise is not considered during these characterizations. As a future work, using short cables, replacing power supply with batteries, using capacitors between power sources are planned to reduce noise.

4.3 MEMS & CMOS ROIC Integration

4.3.1 Design and Layout

Another objective of this work is to design a thermo-mechanical IR sensor array that will be integrated with a readout integrated circuit (ROIC) from the back side and perform on-chip readout. The idea of integrating a ROIC chip with MEMS chip and perform on-chip optical readout is also used for accelerometers [56] and optical microphones [57]. The basic structure of an optical microphone is shown in Figure 4.16. In this example, the readout light is coming from a VCSEL and the light reflected from the gratings is captured with photodetectors. However those structures do not have an array of pixels but just one pixel and readout.

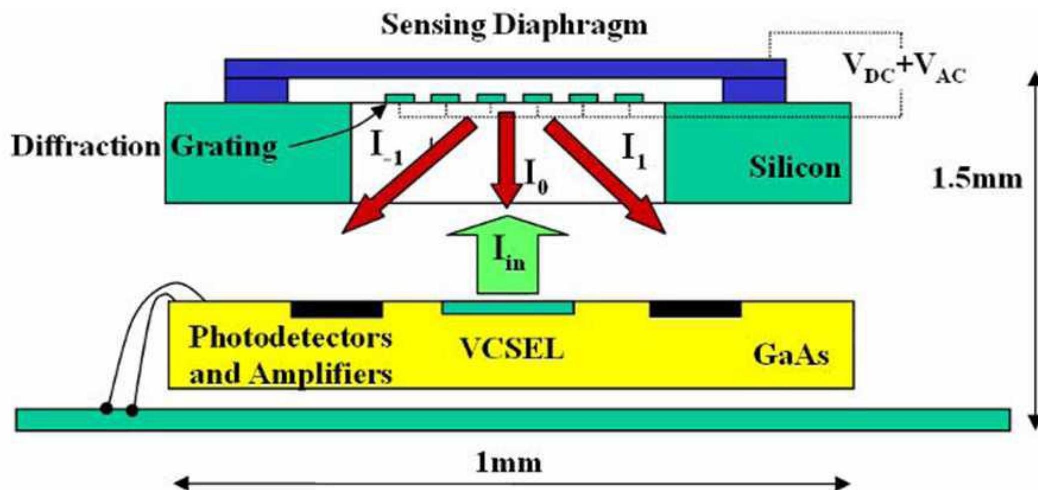

Figure 4.16 IC chip and MEMS integration for optical microphone [57].

A compatible IC chip is designed that will work with both grating readout and optical lever method. In grating readout, the location of the reflected orders do not change, however their intensity changes. Also -1st and +1st diffracted orders are the same, one can sum up these two components to obtain a higher signal value. Thus, it is convenient to use two photodetectors. On the other hand, in the optical lever readout, the readout is reflected from the reflector of the sensor. The detection is performed with a differential readout. The light absorbed by two photodetectors is the same when the IR sensor does not deflect. When the IR sensor bends up or down, one photodetector will absorb more whereas the other one will start to absorb less. Individual trans-impedance amplifiers (TIA) are used for each pixel to amplify and buffer the data. 64 x 64 active pixel arrays are chosen by an analog multiplexer, whose address data is provided by column and row decoders.

The circuit blocks include low power trans-impedance amplifier, noise cancellation circuit, analog multiplexing and decoders. The arrays contain one hole and two photodiodes for each MEMS pixel. For the photodiode type, nwell/psubstrate photodiode is used. The noise cancellation is implemented with a differential readout design. Top level block diagram of the designed circuit is given in Figure 4.17. The specification of the ROIC is given in Table 4-1.

Pixel size	35 µm x 35 µm
Hole diameter	10 µm
Photodiode size	≥ 10 µm x 10 µm
Photodiode number/pixel	2
Array format	64 x 64
Output signal	Voltage
Output signal rate	30 fps

Table 4-1 Specifications of the CMOS ROIC

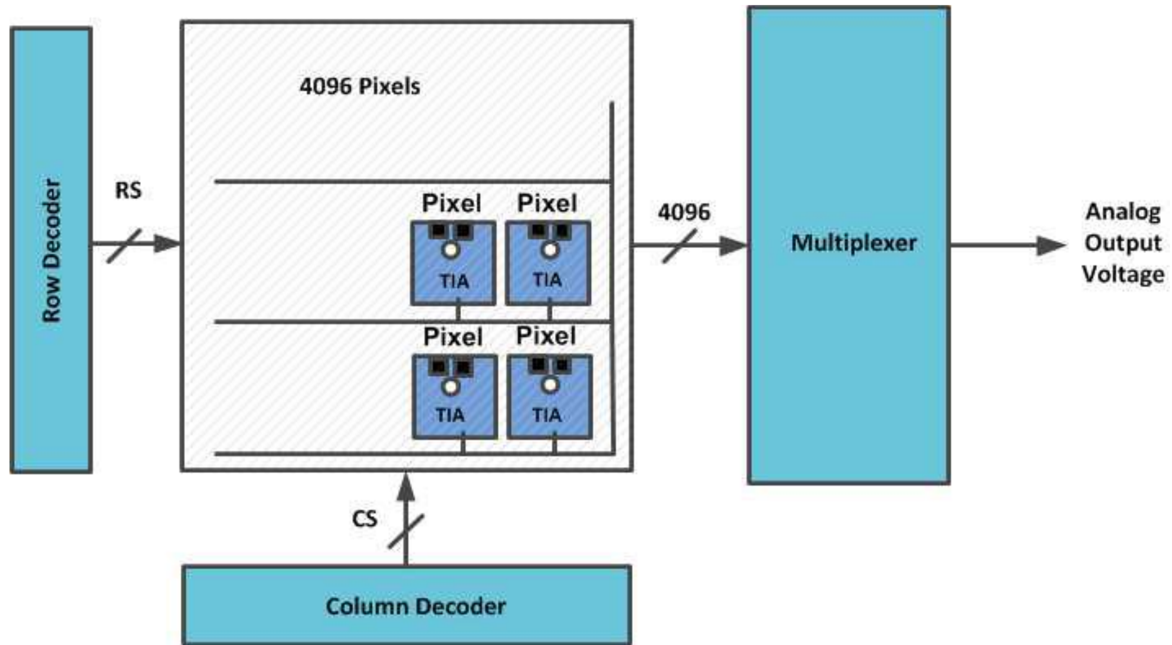

Figure 4.17 Top level structure block diagram.

The layout of the CMOS array and IR sensor array were designed together. For the MEMS part, the layout design depends on the photodiodes and hole locations on the CMOS chip. The photodiode locations are calculated with respect to the reflectors of the IR sensor because the readout laser beam should pass through the holes on the IC chip and afterwards it should reflect from the reflector of the IR sensor. Thus, the reflectors on the IR sensor should be aligned with the holes on the IC chip. Another parameter for the layout is the places of the photodiodes, which determines the placement angle of the gratings and also the area left for the electronics.

The layout of both MEMS part and IC chip is shown in Figure 4.18. In this configuration, MEMS pixels are arranged in a Cartesian grid and reflectors are shifted to

right in one row and to left in the next row, such that photodiodes do not overlap. The two photodiodes are above and below the hole, thus the gratings are placed horizontally.

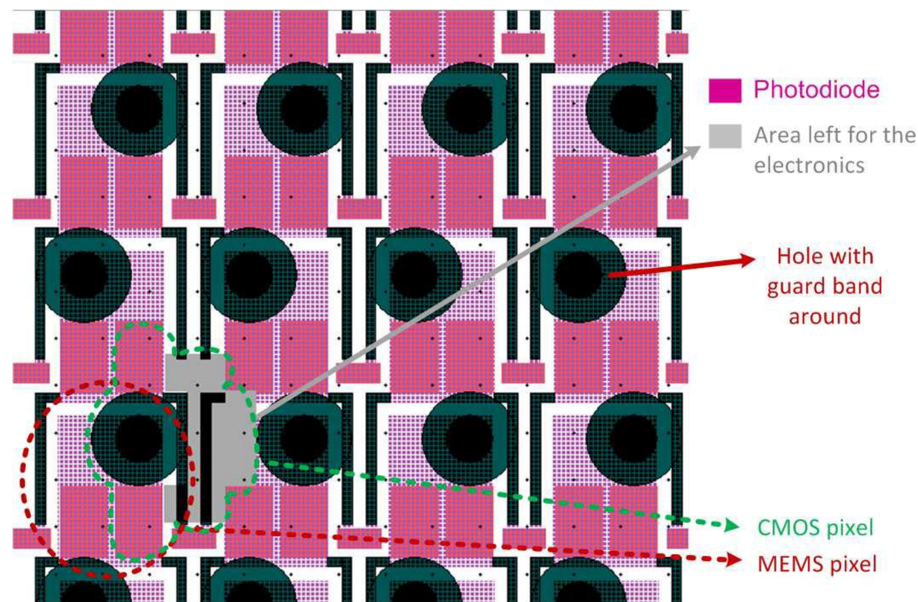

Figure 4.18 MEMS-CMOS array configuration

4.3.2 Alignment and Integration

One important thing during the integration of MEMS and CMOS parts is alignment. Less than 1-2 µm alignment accuracy is required considering the small photodiodes and cross-coupling. Two alignment marks are added on both IR sensor and CMOS chip to facilitate the alignment process. The alignment marks are placed on top and bottom of the arrays to avoid rotation errors.

Several alignment attempts are performed with 2 different configurations using dummy chips. In the first one, a small PCB part is designed as a holder for the MEMS chip. CMOS chip is put on a rotational stage on the optical microscope stage. The PCB is held by a

tweezer using a xyz stage. Alignment is performed using the microscope and when aligned, CMOS and MEMS parts are stacked together using Norland Optical Adhesive 76 UV epoxy. The alignment setup is shown in Figure 4.19.

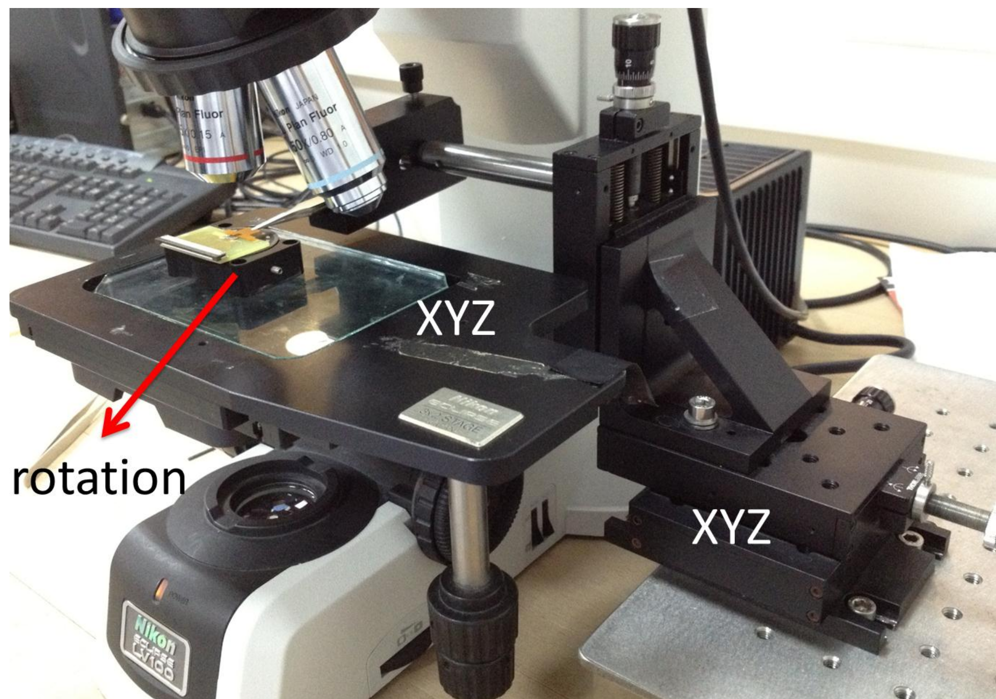

Figure 4.19 First alignment setup

This method has also some disadvantages. Alignment is done using only one alignment mark because CMOS chip is on the microscope stage and it cannot be moved to see the other alignment mark. Thus, rotation errors occurred after UV cure of the epoxy (Figure 4.20 (c,d)). Another problem is the epoxy used while putting MEMS chip to the holder PCB. Since epoxy is a viscous liquid, it floods on the sensor array when pushing PCB to the MEMS chip (Figure 4.20 (a,b)).

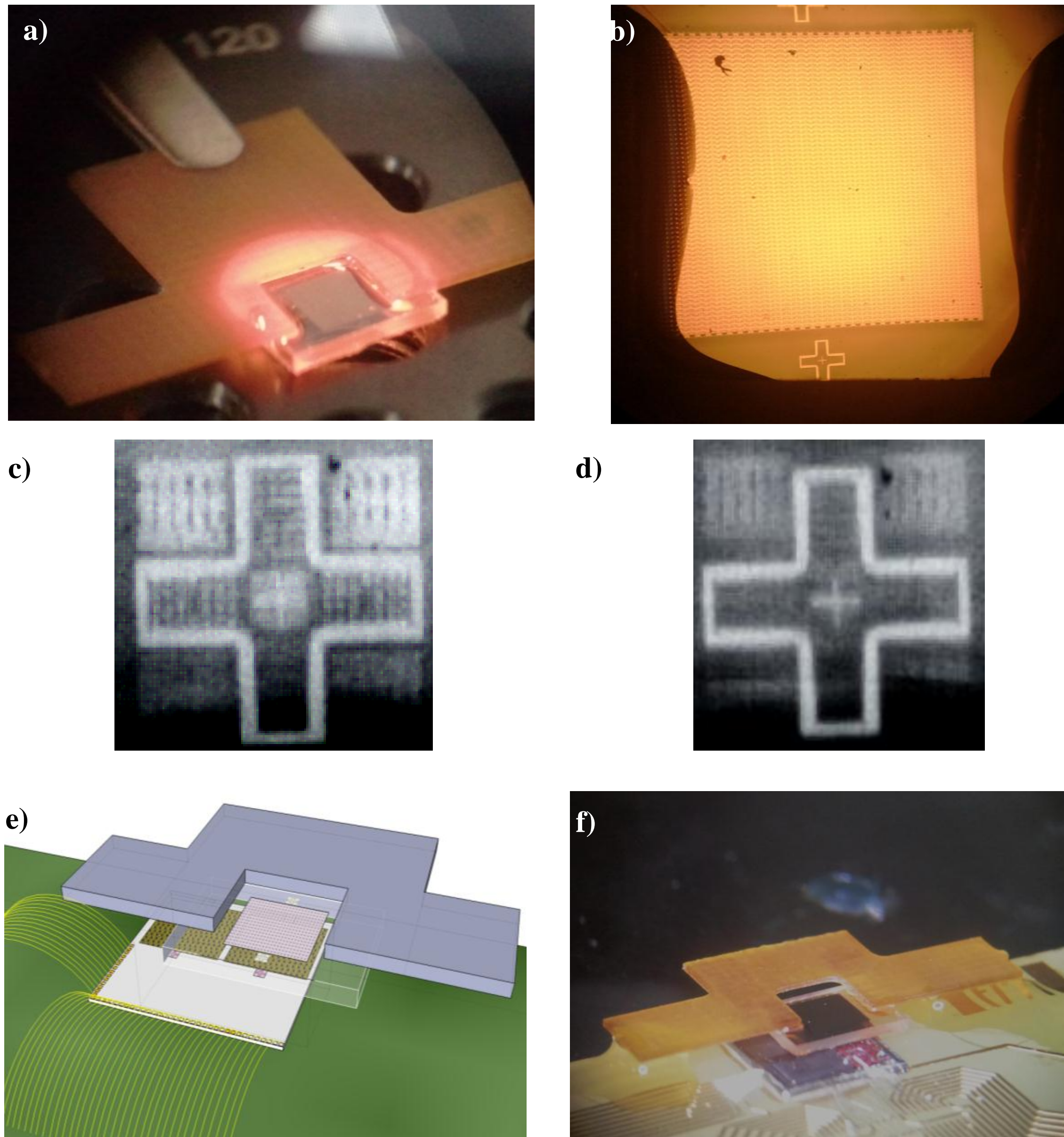

Figure 4.20 (a) MEMS chip with holder PCB. (b) Microscope image of MEMS array with epoxy. (c) Inspected alignment marks after UV cure of epoxy. (d) Alignment mark that is not inspected during alignment. (e) Google SketchUp model of the integration. (f) Image of MEMS chip integrated with CMOS chip.

In the second configuration, a new stage is designed for the microscope that has xyz and rotational stage on it (Figure 4.21 (a)). Thus, microscope stage can be moved to see both alignment marks. Therefore, a more successful alignment was performed. Microscope images of both alignment marks before and after UV curing of epoxy are shown in Figure 4.21 (b,c,d,e)). The alignment and integration of released MEMS devices with post-processed CMOS chips is left as a future work.

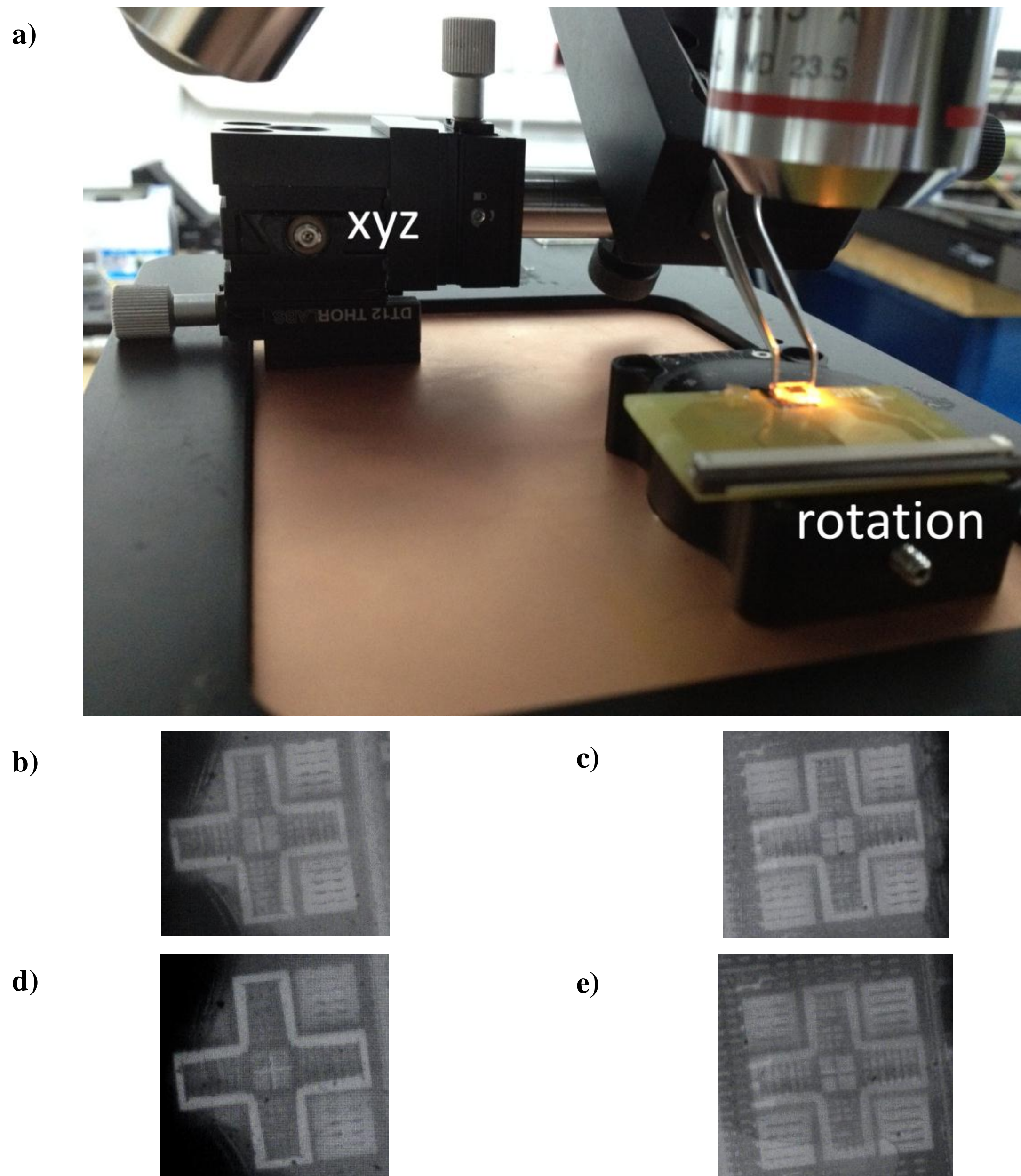

Figure 4.21 (a) Second alignment setup. (b,c) Alignment marks before UV curing (d,e) Alignment marks after UV curing.

4.4 Packaging

For an IR sensor array, it is essential to minimize convective and conductive heat transfer from the substrate to sensor through air in order to prevent thermal crosstalk between adjacent pixels and to reduce the noise. Therefore, optimum operation conditions of the sensor array require vacuum packaging (Figure 4.22 (a)). Furthermore, temperature stabilization for eliminating noise due to ambient temperature fluctuations is another requirement for optimum performance.

The overview of the device after the integration of MEMS chip with CMOS chip is illustrated in Figure 4.22 (b). Integrated device will be inside of a vacuum package with temperature sensor, thermo-electric cooler (TEC) and a heat sink. The fabrication and operation of the sensor arrays within this vacuum package is left as a future work.

a)

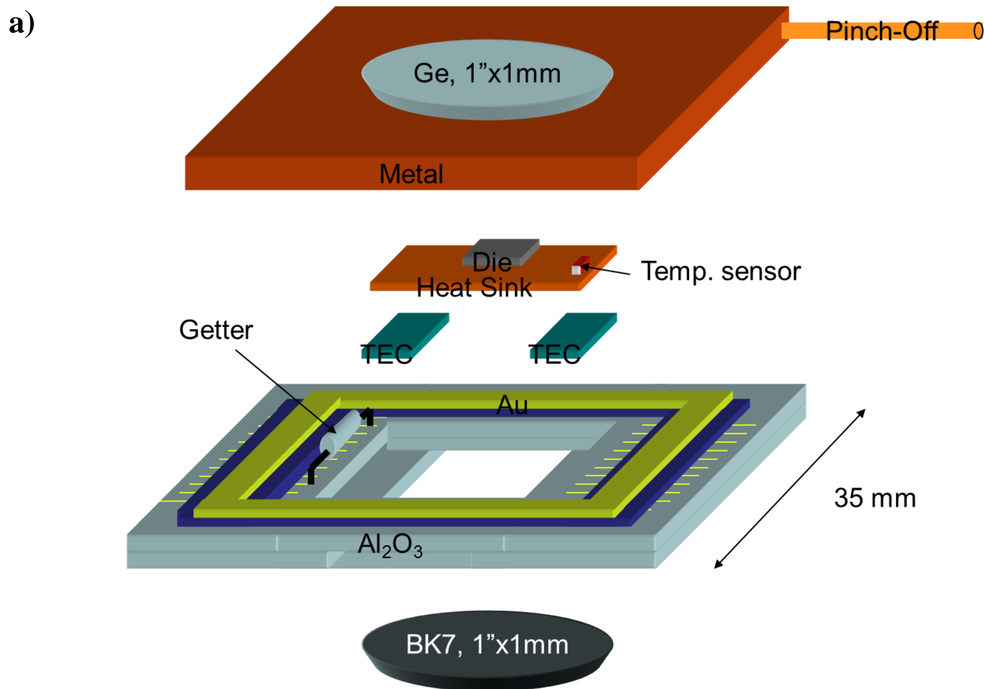

b)

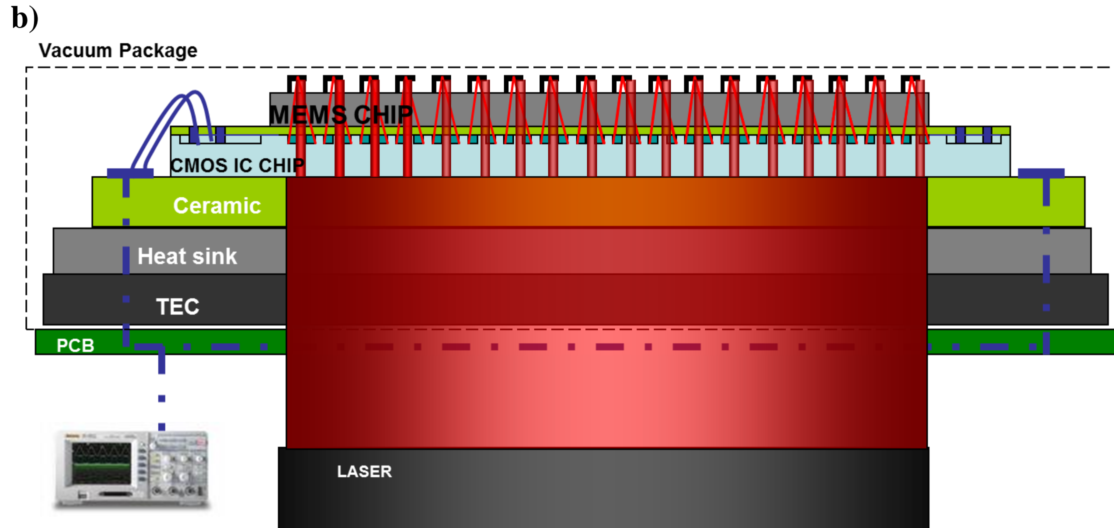

Figure 4.22 (a) Conceptual drawing of the vacuum package. (b) Side view of the CMOS ROIC chip integrated with IR detector in vacuum package.

5 CONCLUSION

In this thesis, design, fabrication and testing of IR thermo-mechanical detector array with integrated optical readout are reported. These detector arrays have several advantages compared to other types of IR sensing devices such as low cost and scalability to high-resolutions. High sensitivity and immunity against vibrations and saturation can be obtained with the embedded diffraction grating readout. Two options are exploited for the optical readout: (i) reimaging of diffracted light onto a CCD camera using Fourier filtering, (ii) integration of MEMS sensor array chip on a CMOS readout chip that contains a photodetector array and a through wafer via hole for each pixel for the illumination beam. This is a novel approach for optical readout and tried for the first time.

35 µm pitch size, 640x480, 320x240 and 64x64 thermo-mechanical detector arrays with diffraction grating and lever based optical readout are designed. The design phase of the research focused on the design and optimization ox pixel structures that form the FPA. The main design effort is a self-leveling detector that does not require thermo-electric cooling. Silicon nitride based detector arrays are fabricated at METU-MEMS center and parylene based detector arrays are fabricated at Center of MicroNano Technology (CMi) at Ecole Polytechnique Fédérale de Lausanne (EPFL). The main work done during this thesis is the fabrication of parylene based sensors. Several process optimizations are developed that results in successful fabrication of the detectors, but there are still some remaining challenges for the fabrication of stress-free devices.

Characterization of fabricated arrays such as minimum detectable temperature measurements, mechanical deflection measurement, time constant measurements, is

performed. Theoretical calculations indicate state of the art performance (<100mK NETD) using 10-12 bit CCD camera for optimal designs after successful fabrication of the arrays.

Since MEMS and readout is decoupled, a compatible CMOS ROIC for readout of the thermo-mechanical IR detector array was designed and fabricated by a research group at EPFL. A post-process is performed and the CMOS chips are thinned to 100 μm and through wafer holes with 10 μm diameter are etched, which allow the readout laser beam to pass through.

Integration of MEMS chip on a CMOS readout chip is achieved during this thesis. The system complexity is significantly simplified through integrating optics with custom CMOS ROIC and the MEMS array. A setup is realized to align 64x64 IR detector array with 64x64 photodiode array. Two chips are aligned and integrated with 1-2 μm accuracy. Future work involves fabrication of a vacuum package and operation of the integrated sensor arrays in this package.

BIBLIOGRAPHY

[1] H. Torun, "Design and Fabrication of Thermo-Mechanical Thermal Detector Arrays with Optical Readout," MSc Thesis, Electrical and Computer Engineering, Koç University, Istanbul, 2005.

[2] M. F. Toy, "Optical Readout for Infrared Thermo-mechanical Detector Array," MSc Thesis, Electrical and Computer Engineering, Koç University, Istanbul, 2008.

[3] O. Ferhanoğlu, "Design, Fabrication and Characterization of a MOEMS based Thermal Imaging System," PhD Thesis, Electrical and Engineering, Koç University, Istanbul, 2010.

[4] L. Hyung-Kew, Y. Jun-Bo, Y. Euisik, J. Sang-Baek, Y. Yoon-Joong, L. Wook, and K. Sang-Gook, "A high fill-factor infrared bolometer using micromachined multilevel electrothermal structures," *IEEE Transactions on Electron Devices,* vol. 46, pp. 1489-1491, 1999.

[5] R. B. Spielman, C. Deeney, D. L. Fehl, D. L. Hanson, N. R. Keltner, J. S. McGurn, and J. L. McKenney, "Fast resistive bolometry," *Review of Scientific Instruments,* vol. 70, pp. 651-655, 1999.

[6] D. Sabuncuoglu Tezcan, S. Eminoglu, O. S. Akar, and T. Akin, "A low cost uncooled infrared microbolometer focal plane array using the CMOS n-well layer," in *Micro Electro Mechanical Systems, 2001. MEMS 2001. The 14th IEEE International Conference on*, 2001, pp. 566-569.

[7] C. Li, G. D. Skidmore, C. Howard, C. J. Han, L. Wood, D. Peysha, E. Williams, C. Trujillo, J. Emmett, G. Robas, D. Jardine, C. F. Wan, and E. Clarke, "Recent development of ultra small pixel uncooled focal plane arrays at DRS," Orlando, FL, USA, 2007, pp. 65421Y-12.

[8] J.-L. Tissot, S. Tinnes, A. Durand, C. Minassian, P. Robert, M. Vilain, and J.-J. Yon, "High-performance uncooled amorphous silicon video graphics array and extended graphics array infrared focal plane arrays with 17- um pixel pitch," *Optical Engineering,* vol. 50, pp. 061006-7, 2011.

[9] F. Niklaus, C. Vieider, and H. Jakobsen, "MEMS-based uncooled infrared bolometer arrays: a review," Beijing, China, 2007, pp. 68360D-15.

[10] E. A. Wachter, T. Thundat, P. I. Oden, R. J. Warmack, P. G. Datskos, and S. L. Sharp, "Remote optical detection using microcantilevers," *Review of Scientific Instruments,* vol. 67, pp. 3434-3439, 1996.

[11] R. Amantea, C. M. Knoedler, F. P. Pantuso, V. Patel, D. J. Sauer, and J. R. Tower, "Uncooled IR imager with 5-mK NETD," Orlando, FL, USA, 1997, pp. 210-222.
[12] P. I. Oden, P. G. Datskos, T. Thundat, and R. J. Warmack, "Uncooled thermal imaging using a piezoresistive microcantilever," *Applied Physics Letters,* vol. 69, pp. 3277-3279, 1996.
[13] P. G. Datskos, P. I. Oden, T. Thundat, E. A. Wachter, R. J. Warmack, and S. R. Hunter, "Remote infrared radiation detection using piezoresistive microcantilevers," *Applied Physics Letters,* vol. 69, pp. 2986-2988, 1996.
[14] P. I. Oden, E. A. Wachter, P. G. Datskos, T. G. Thundat, and R. J. Warmack, "Optical and infrared detection using microcantilevers," Orlando, FL, USA, 1996, pp. 345-354.
[15] P. G. Datskos, S. Rajic, and I. Datskou, "Photoinduced and thermal stress in silicon microcantilevers," *Applied Physics Letters,* vol. 73, pp. 2319-2321, 1998.
[16] P. G. Datskos, S. Rajic, and I. Datskou, "Detection of infrared photons using the electronic stress in metal–semiconductor cantilever interfaces," *Ultramicroscopy,* vol. 82, pp. 49-56, 2000.
[17] L. R. Senesac, J. L. Corbeil, S. Rajic, N. V. Lavrik, and P. G. Datskos, "IR imaging using uncooled microcantilever detectors," *Ultramicroscopy,* vol. 97, pp. 451-458, 2003.
[18] P. G. Datskos, N. V. Lavrik, and S. Rajic, "Performance of uncooled microcantilever thermal detectors," *Review of Scientific Instruments,* vol. 75, pp. 1134-1148, 2004.
[19] P. G. Datskos and N. V. Lavrik, "Uncooled Infrared MEMS Detectors," in *Smart Sensors and MEMS*. vol. 181, S. Y. Yurish and M. T. S. R. Gomes, Eds., ed: Springer Netherlands, 2004, pp. 381-419.
[20] N. Lavrik, R. Archibald, D. Grbovic, S. Rajic, and P. Datskos, "Uncooled MEMS IR imagers with optical readout and image processing," Orlando, FL, USA, 2007, pp. 65421E-8.
[21] R. Amantea, L. A. Goodman, F. P. Pantuso, D. J. Sauer, M. Varghese, T. S. Villani, and L. K. White, "Progress toward an uncooled IR imager with 5-mK NETD," San Diego, CA, USA, 1998, pp. 647-659.
[22] S. R. Hunter, R. A. Amantea, L. A. Goodman, D. B. Kharas, S. Gershtein, J. R. Matey, S. N. Perna, Y. Yu, N. Maley, and L. K. White, "High-sensitivity uncooled microcantilever infrared imaging arrays," Orlando, FL, USA, 2003, pp. 469-480.
[23] S. R. Hunter, G. Maurer, L. Jiang, and G. Simelgor, "High-sensitivity uncooled microcantilever infrared imaging arrays," Orlando (Kissimmee), FL, USA, 2006, pp. 62061J-12.

[24] S. R. Hunter, G. S. Maurer, G. Simelgor, S. Radhakrishnan, J. Gray, K. Bachir, T. Pennell, M. Bauer, and U. Jagadish, "Development and optimization of microcantilever based IR imaging arrays," Orlando, FL, USA, 2008, pp. 694013-12.

[25] T. Perazzo, M. Mao, O. Kwon, A. Majumdar, J. B. Varesi, and P. Norton, "Infrared vision using uncooled micro-optomechanical camera," *Applied Physics Letters,* vol. 74, pp. 3567-3569, 1999.

[26] J. Zhao, "High sensitivity photomechanical MW-LWIR imaging using an uncooled MEMS microcantilever array and optical readout (Invited Paper)," Orlando, FL, USA, 2005, pp. 506-513.

[27] J. R. Barnes, R. J. Stephenson, C. N. Woodburn, S. J. O'Shea, M. E. Welland, T. Rayment, J. K. Gimzewski, and C. Gerber, "A femtojoule calorimeter using micromechanical sensors," *Review of Scientific Instruments,* vol. 65, pp. 3793-3798, 1994.

[28] J. Varesi, J. Lai, T. Perazzo, Z. Shi, and A. Majumdar, "Photothermal measurements at picowatt resolution using uncooled micro-optomechanical sensors," *Applied Physics Letters,* vol. 71, pp. 306-308, 1997.

[29] S. R. Manalis, S. C. Minne, C. F. Quate, G. G. Yaralioglu, and A. Atalar, "Two-dimensional micromechanical bimorph arrays for detection of thermal radiation," *Applied Physics Letters,* vol. 70, pp. 3311-3313, 1997.

[30] A. Rogalski, "Novel uncooled infrared detectors," *Opto-Electronics Review,* vol. 18, pp. 478-492, 2010/12/01 2010.

[31] M. F. Toy, O. Ferhanoglu, T. Hamdi, F. L. Degertekin, and H. Urey, "MOEMS thermal imaging camera," in *Research in Microelectronics and Electronics, 2008. PRIME 2008. Ph.D.*, 2008, pp. 101-104.

[32] O. Ferhanoglu, M. F. Toy, and H. Urey, "Parylene-based uncooled thermomechanical array," Orlando, FL, USA, 2009, pp. 72980H-8.

[33] O. Ferhanoglu and H. Urey, "Sensitivity enhancement of bimaterial MOEMS thermal imaging sensor array using 2-lambda wavelength readout," Brussels, Belgium, 2010, pp. 77180O-6.

[34] O. Ferhanoglu and H. Urey, "Sensitivity enhancement of grating interferometer based two-dimensional sensor arrays using two-wavelength readout," *Appl. Opt.,* vol. 50, pp. 3289-3295, 2011.

[35] O. Ferhanoglu, M. F. Toy, G. Unal, and H. Kalyoncu, "Thermal-mechanical Detector Array with Integrated Diffraction Grating," in *Lasers and Electro-Optics Society, 2007. LEOS 2007. The 20th Annual Meeting of the IEEE*, 2007, pp. 836-837.

[36] H. Torun, O. Ferhanoglu, and H. Urey, "Thermo-Mechanical Detector Array with Optical Readout," in *Optical MEMS and Their Applications Conference, 2006. IEEE/LEOS International Conference on*, 2006, pp. 112-113.

[37] M. F. Toy, O. Ferhanoglu, H. Torun, and H. Urey, "Uncooled infrared thermo-mechanical detector array: Design, fabrication and testing," *Sensors and Actuators A: Physical,* vol. 156, pp. 88-94, 2009.

[38] H. Torun and H. Urey, "Uncooled thermo-mechanical detector array with optical readout," *Opto-Electronics Review,* vol. 14, pp. 54-58, 2006.

[39] W. Lang, K. Kühl, and H. Sandmaier, "Absorbing layers for thermal infrared detectors," *Sensors and Actuators A: Physical,* vol. 34, pp. 243-248, 1992.

[40] J. W. L. Zhou, C. Ho-Yin, T. K. H. To, K. W. C. Lai, and W. J. Li, "Polymer MEMS actuators for underwater micromanipulation," *Mechatronics, IEEE/ASME Transactions on,* vol. 9, pp. 334-342, 2004.

[41] L. Zhihua, W. Yangjie, C. Ho-Yin, L. Wen Jung, D. Zaili, and W. Yuechao, "Structural and Thermal Analysis of a Thermally Actuated Polymer Micro Robotic Gripper," in *Robotics and Biomimetics, 2004. ROBIO 2004. IEEE International Conference on*, 2004, pp. 470-473.

[42] Y. Tze-Jung, K. Walsh, and T. Yu-Chong, "Dielectric charging effects on Parylene electrostatic actuators," in *Micro Electro Mechanical Systems, 2002. The Fifteenth IEEE International Conference on*, 2002, pp. 614-617.

[43] H. Torun, K. K. Sarangapani, P. Joseph, F. L. Degertekin, and C. Zhu, "A micromachined membrane-based active probe for biomolecular mechanicsmeasurement," *Nanotechnology,* vol. 18, 2007.

[44] R. Luharuka, H. M. Noh, S. K. Kim, H. Mao, L. Wong, and P. J. Hesketh, "Improved manufacturability and characterization of a corrugated Parylene diaphragm pressure transducer," *Journal of Micromechanics and Microengineering,* vol. 16, 2006.

[45] M. Liger, S. Konishi, and T. Yu-Chong, "Uncooled all-parylene bolometer," in *Micro Electro Mechanical Systems, 2004. 17th IEEE International Conference on. (MEMS)*, 2004, pp. 593-596.

[46] T. N. Pornsin-Sirirak, Y. C. Tai, H. Nassef, and C. M. Ho, "Flexible parylene actuator for micro adaptive flow control," in *Micro Electro Mechanical Systems, 2001. MEMS 2001. The 14th IEEE International Conference on*, 2001, pp. 511-514.

[47] K. Walsh, J. Norville, and T. Yu-Chong, "Photoresist as a sacrificial layer by dissolution in acetone," in *Micro Electro Mechanical Systems, 2001. MEMS 2001. The 14th IEEE International Conference on*, 2001, pp. 114-117.

[48] T.-J. Yao, X. Yang, and Y.-C. Tai, "BrF3 dry release technology for large freestanding parylene microstructures and electrostatic actuators," *Sensors and Actuators A: Physical,* vol. 97–98, pp. 771-775, 2002.

[49] H. Qing, E. Meng, T. Yu-Chong, C. M. Rutherglen, J. Erickson, and J. Pine, "Parylene neuro-cages for live neural networks study," in *TRANSDUCERS, Solid-State Sensors, Actuators and Microsystems, 12th International Conference on, 2003*, 2003, pp. 995-998 vol.2.

[50] F. Zhifang, J. M. Engel, J. Chen, and L. Chang, "Parylene surface-micromachined membranes for sensor applications," *Microelectromechanical Systems, Journal of,* vol. 13, pp. 484-490, 2004.

[51] C. A. Gutierrez and E. Meng, "Parylene-Based Electrochemical-MEMS Transducers," *Microelectromechanical Systems, Journal of,* vol. 19, pp. 1352-1361, 2010.

[52] S. Satyanarayana, D. T. McCormick, and A. Majumdar, "Parylene micro membrane capacitive sensor array for chemical and biological sensing," *Sensors and Actuators B: Chemical,* vol. 115, pp. 494-502, 2006.

[53] H. Torun, K. K. Sarangapani, and F. L. Degertekin, "Fabrication and Characterization of Micromachined Active Probes With Polymer Membranes for Biomolecular Force Spectroscopy," *Microelectromechanical Systems, Journal of,* vol. 19, pp. 1021-1028, 2010.

[54] J. L. Corbeil, N. V. Lavrik, S. Rajic, and P. G. Datskos, "``Self-leveling" uncooled microcantilever thermal detector," *Applied Physics Letters,* vol. 81, pp. 1306-1308, 2002.

[55] S. Z. Temel, "Smart Pixel Array and Readout IC with Built-In Noiise Cancellation," MSc Thesis, Electrical and Electronics Engineering, Ecole Polytechnique Fédérale de Lausanne, Lausanne, 2010.

[56] N. A. Hall, M. Okandan, R. Littrell, D. K. Serkland, G. A. Keeler, K. Peterson, B. Bicen, C. T. Garcia, and F. L. Degertekin, "Micromachined Accelerometers With Optical Interferometric Read-Out and Integrated Electrostatic Actuation," *Journal of Microelectromechanical Systems,* vol. 17, pp. 37-44, 2008.

[57] M. Okandan, N. Hall, B. Bicen, C. Garcia, and F. L. Degertekin, "Optical Microphone Structures Fabricated for Broad Bandwidth and Low Noise," in *Sensors, 2007 IEEE*, 2007, pp. 1472-1475.